KEK Proceedings 2005-10
November 2005
R

Proceedings of the Twelfth EGS Users' Meeting in Japan

August 9 - 11, 2005.

KEK, Tsukuba, Japan

Edited by

Y. Namito, H. Hirayama and S. Ban

High Energy Accelerator Research Organization

FOREWARD

The Twelfth EGS Users' Meeting in Japan was held at High Energy Accelerator Research Organization (KEK) from August 9 to 11. The meeting has been hosted by the Radiation Science Center. Nearly 100 participants attended the meeting.

The meeting was divided into two parts. Short course on EGS was held at the first half of the workshop using test version of EGS5 code. In the later half, 18 talks related EGS were presented. The talk covered the wide fields, like the medical application and the calculation of various detector responses *etc.* These talks were very useful to exchange the information between the researchers in the different fields.

Finally, we would like to express our great appreciation to all authors who have prepared manuscript quickly for the publication of this proceedings.

Hideo Hirayama
Yoshihito Namito
Syuichi Ban
Radiation Science Center
KEK, High Energy Accelerator Research Organization

CONTENTS

MOLIÈRE ANGULAR AND LATERAL DISTRIBUTIONS WITH IONIZATION

T. Nakatsuka and K. Okei[†]

Okayama Shoka University, Okayama 700-8601, Japan

[†]*Dept. of Physics, Okayama University, Okayama 700-8530, Japan*

Abstract

The Molière distribution for arbitrary linear combination between the deflection angle and the lateral displacement is improved to take into account ionization loss. The analytical results for lateral distribution derived through numerical integrations for dilogarithm function are compared with our detailed Monte Carlo results. Goudsmit-Saunderson angular distribution derived with Molière parameters, is also confirmed to agree with our detailed Monte Carlo results.

1 Introduction

Molière derived the distribution for the arbitrary combination between the deflection angle and the lateral displacement under the fixed-energy condition [1]. We proposed the formulation to give the distribution under the ionization process based on the Kamata-Nishimura theory [2, 3] and got the distribution in some special conditions [4]. This time we have obtained the distribution for the arbitrary combination between them, carrying out the integration using the dilogarithm function. The theoretical results are compared with our Monte Carlo results [5].

It is well known the Molière-Bethe theory [6, 7, 8] is less accurate than the Goudsmit-Saunderson theory [9, 10] due to the small angle approximation [11] applied in the former theory. We found even the Goudsmit-Saunderson angular distribution with ionization can be expressed with the Molière characteristic parameters, B and $\theta_{\rm M}$, based on the Lewis theory [12]. We confirm our prediction by comparing the analytical results with our detailed Monte Carlo result without the small angle approximation.

2 Molière distributions with ionization for arbitrary linear combination of the deflection angle and the lateral displacement

Let the simultaneous distribution between the deflection angle $\vec{\theta}$ and the lateral displacement $\vec{r}$ be $f(\vec{\theta},\vec{r},t)d\vec{\theta}d\vec{r}$, the diffusion equation is described as

$$\frac{\partial \tilde{f}}{\partial t'} = \vec{\eta}\frac{\partial \tilde{f}}{\partial \vec{\zeta}'} - \frac{K^2\zeta'^2}{4E'^2}\tilde{f}\{1-\frac{1}{\Omega}\ln\frac{K^2\zeta'^2}{4E'^2}\} \tag{1}$$

under the Kamata-Nishimura formulation, where $\tilde{f}(\vec{\zeta},\vec{\eta},t)$ denotes the Fourier transforms of the simultaneous distribution

$$f(\vec{\theta},\vec{r},t) = \frac{1}{4\pi^2}\iiint e^{-i\vec{\theta}\vec{\zeta}-i\vec{r}\vec{\eta}}\tilde{f}(\vec{\zeta},\vec{\eta},t)d\vec{\zeta}d\vec{\eta}, \tag{2}$$

and $\vec{\zeta}$ and $\vec{\eta}$ denote the Fourier variables corresponding to $\vec{\theta}$ and $\vec{r}$, respectively. The variables $\vec{\zeta}'$ and E' in Eq. (1) are primed to note that they change together with the differential variable t' under the ionization process of

$$E = E_0 - \varepsilon t, \tag{3}$$

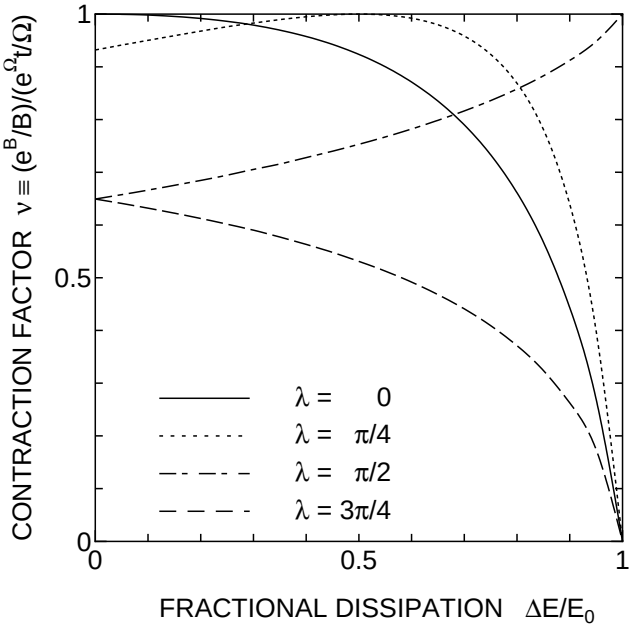

Figure 1: The ratios of e^B/B to $e^\Omega t/\Omega$ under the ionization process, i.e. the contraction factors ν for distributions of the linear combination $\vec{\rho} \equiv \vec{\theta}\cos\lambda + (\vec{r}/t)\sin\lambda$, defined for the extreme-relativistic charged particles. Abscissa denotes the fraction of dissipated energy $(E_0 - E)/E_0$.

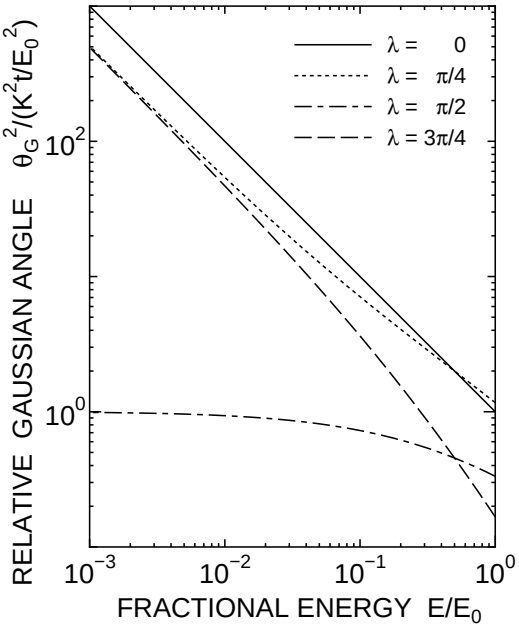

Figure 2: The ratios of $\theta_{\rm G}^2$, i.e. the gaussian mean square angle for distributions of the linear combination angle $\vec{\rho} \equiv \vec{\theta}\cos\lambda + (\vec{r}/t)\sin\lambda$ under the ionization process defined for extreme-relativistic charged particles, to $\Omega^{-1}K^2t/E_0^2$. Abscissa denotes the fraction of residual energy E/E_0.

where E_0 and E denote energies at the incidence and the destination. The first term of the right-hand side of Eq. (1) vanishes when we replace the variable $\vec{\zeta}'$ as

$$\vec{\zeta}' = \vec{\zeta} + (t - t')\vec{\eta}, \tag{4}$$

where t and $\vec{\zeta}$ denote those at the destination. Thus we have

$$\ln 4\pi^2 \tilde{f} = -\int_0^t \frac{K^2\zeta'^2}{4E'^2}\{1 - \frac{1}{\Omega}\ln\frac{K^2\zeta'^2}{4E'^2}\}dt' = \int_0^1 \frac{K^2t(\vec{\zeta} + \vec{\eta}tu)^2}{4\Omega(E + \varepsilon tu)^2}\ln\frac{K^2(\vec{\zeta} + \vec{\eta}tu)^2}{4e^\Omega(E + \varepsilon tu)^2}du. \tag{5}$$

Let $\vec{\rho}$ be the linear combination of the deflection angle $\vec{\theta}$ and the lateral displacement $\vec{r}$, or the chord angle $\vec{r}/t$ [1, 11], with respective weights of a and b,

$$\vec{\rho} = a\vec{\theta} + b\vec{r}/t, \tag{6}$$

and be its probability density, then we have

$$g(\vec{\rho}, t)d\vec{\rho} = \frac{td\vec{\rho}}{b}\iint f(\vec{\theta}, \frac{t}{b}(\vec{\rho} - a\vec{\theta}), t)d\vec{\theta}. \tag{7}$$

Let $\tilde{g}(\vec{\xi}, t)$ be the Fourier transforms of $g(\vec{\rho}, t)$,

$$\tilde{g}(\vec{\xi}) = \frac{1}{2\pi}\iint e^{-i\vec{\xi}\vec{\rho}}g(\vec{\rho}, t)d\vec{\rho} = 2\pi\tilde{f}(a\vec{\xi}, b\vec{\xi}/t, t), \tag{8}$$

Table 1: The contraction factor ν for the linear combination $\vec{\rho}$, taking $a = \cos\lambda$ and $b = \sin\lambda$.

$\Delta E/E_0$	$\lambda = 0$	$\lambda = \pi/4$	$\lambda = \pi/2$	$\lambda = 3\pi/4$
.00	1.000E+00	9.320E-01	6.492E-01	6.492E-01
.05	9.996E-01	9.412E-01	6.575E-01	6.409E-01
.10	9.982E-01	9.502E-01	6.662E-01	6.320E-01
.15	9.956E-01	9.590E-01	6.752E-01	6.225E-01
.20	9.917E-01	9.677E-01	6.846E-01	6.124E-01
.25	9.863E-01	9.760E-01	6.945E-01	6.016E-01
.30	9.791E-01	9.829E-01	7.054E-01	5.902E-01
.35	9.696E-01	9.895E-01	7.157E-01	5.772E-01
.40	9.576E-01	9.949E-01	7.278E-01	5.632E-01
.45	9.425E-01	9.986E-01	7.400E-01	5.481E-01
.50	9.236E-01	1.000E+00	7.531E-01	5.310E-01
.55	9.002E-01	9.982E-01	7.670E-01	5.126E-01
.60	8.711E-01	9.921E-01	7.821E-01	4.917E-01
.65	8.349E-01	9.797E-01	7.986E-01	4.680E-01
.70	7.898E-01	9.583E-01	8.164E-01	4.409E-01
.75	7.331E-01	9.236E-01	8.360E-01	4.091E-01
.80	6.609E-01	8.686E-01	8.580E-01	3.711E-01
.85	5.674E-01	7.811E-01	8.829E-01	3.240E-01
.90	4.430E-01	6.390E-01	9.122E-01	2.625E-01
.95	2.695E-01	3.986E-01	9.482E-01	1.740E-01
1.00	.000E+00	.000E+00	1.000E+00	.000E+00

then we have

$$\begin{aligned}
\ln 2\pi\tilde{g} &= \int_0^1 \frac{K^2 t\xi^2 (a+bu)^2}{4\Omega(E+\varepsilon tu)^2} \ln \frac{K^2\xi^2(a+bu)^2}{4e^{\Omega}(E+\varepsilon tu)^2} du \\
&= \int_E^{E_0} \frac{b^2K^2t\xi^2}{4\Omega\varepsilon^3t^3}(1-\frac{Q}{E'})^2 \ln[\frac{b^2K^2\xi^2}{4e^{\Omega}\varepsilon^2t^2}(1-\frac{Q}{E'})^2] dE' \\
&= \int_{Q/E_0}^{Q/E} \frac{b^2QK^2t\xi^2}{4\Omega\varepsilon^3t^3}(1-\frac{1}{s})^2 \ln \frac{b^2K^2\xi^2(1-s)^2}{4e^{\Omega}\varepsilon^2t^2} ds \\
&= -\frac{b^2QK^2t\xi^2}{4\Omega(E_0-E)^3}\{2[s+\ln|s|-(s-\frac{1}{s})\ln|1-s|-2\mathcal{L}_2(s)]_{Q/E_0}^{Q/E} \\
&\qquad -[s-\frac{1}{s}-2\ln|s|]_{Q/E_0}^{Q/E} \ln\frac{b^2K^2\xi^2}{4e^{\Omega}(E_0-E)^2}\}, \qquad (9)
\end{aligned}$$

where we introduced an energy parameter Q and the dilogarithm function $\mathcal{L}_2(z)$ [13, 14]:

$$Q \equiv E - (a/b)\varepsilon t, \qquad (10)$$

$$\mathcal{L}_2(z) = \int_z^0 \frac{\ln|1-t|}{t} dt. \qquad (11)$$

Thus we can get the spatial distribution for $\vec{\rho}$ by using our translation formula [15]:

$$g(\vec{\rho},t)d\vec{\rho} = f(\vartheta)d\vec{\vartheta} \qquad \text{with} \qquad \vec{\vartheta} = \vec{\rho}/\theta_{\rm M}, \qquad (12)$$

where

$$2\pi f(\vartheta) = f^{(0)}(\vartheta) + B^{-1}f^{(1)}(\vartheta) + B^{-2}f^{(2)}(\vartheta) + \ldots. \qquad (13)$$

The characteristic parameters B and $\theta_{\rm M}$ are determined as

$$B - \ln B = \Omega - \ln\Omega + \ln\nu t \qquad (14)$$

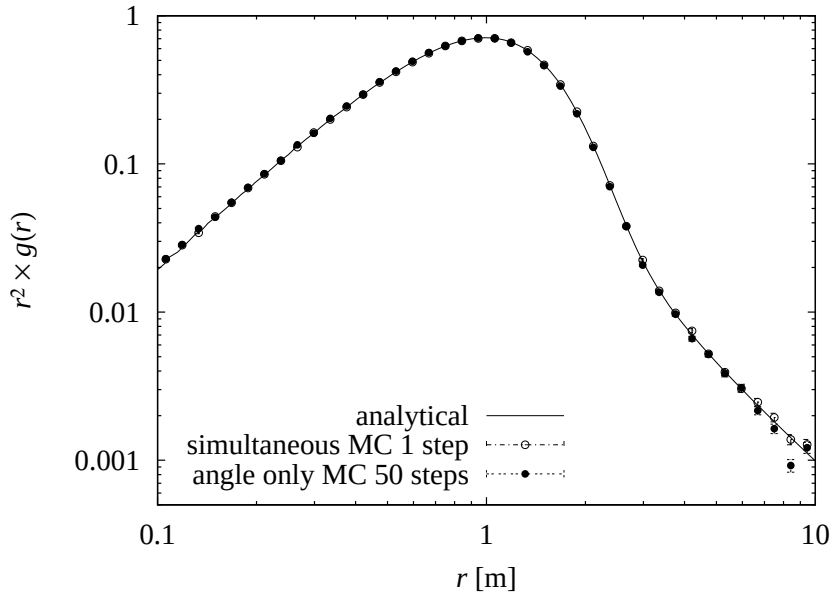

Figure 3: Analytical prediction of lateral distribution of muon after dissipating half of its energy agrees with the Monte Carlo result.

with

$$\ln \nu = \frac{2[s + \ln|s| - (s - s^{-1})\ln|1 - s| - 2\mathcal{L}_2(s)]_{Q/E_0}^{Q/E}}{[s - s^{-1} - 2\ln|s|]_{Q/E_0}^{Q/E}} + \ln \frac{Q[s - s^{-1} - 2\ln|s|]_{Q/E_0}^{Q/E}}{E_0 - E}, \tag{15}$$

and

$$\theta_{\rm M}^2 = \frac{B}{\Omega}\theta_{\rm G}^2 \qquad \text{with} \qquad \theta_{\rm G}^2 \equiv \frac{b^2 Q K^2 t}{(E_0 - E)^3}[s - \frac{1}{s} - 2\ln|s|]_{Q/E_0}^{Q/E}. \tag{16}$$

ν and $\theta_{\rm G}^2$ denote the contraction factor and the gaussian mean square angle respectively for the combination angle $\vec{\rho}$ of Eq. (6). The projected distribution for $\vec{\rho}$ can also be derived likewise. The limits of Eqs. (14) and (16) at $\varepsilon \to 0$ give the Molière's results for the combination angle under the fixed-energy condition [1].

3 Evaluation of ν and $\theta_{\rm G}^2$ and the Molière distributions

We indicate the contraction factor ν of Eq. (15) in Table 1 and Fig. 1 and the factor of gaussian mean square angle $\theta_{\rm G}^2$ of Eq. (16) to $K^2 t/E_0^2$ in Fig. 2, for the linear combination $\vec{\rho}$ taking

$$a = \cos\lambda \qquad \text{and} \qquad b = \sin\lambda \tag{17}$$

as Molière did [1]. The both factors are functions of the fraction of residual energy E/E_0, or functions of the fraction of dissipated energy $\varepsilon t/E_0$. Our factors at $\Delta E/E_0 = 0$ in Fig. 1 and ours at $E/E_0 = 1$ in Fig. 2 agree with Molière's results without ionization in his Table 1 [1]. We find only the lateral distribution or the chord-angle distribution ($\lambda = \pi/2$) has the factors of non-zero finite value, so that has the definite distribution, at the limit of $E \to 0$.

Molière lateral distribution with ionization is derived as the combination of $a = 0$ and $b = 1$, or $\lambda = \pi/2$. The result for 100 GeV muon, having dissipated half of its energy after penetrating water of 250 m, is compared with the simulation result by our high-accurate and high efficient Monte Carlo code [5] in Fig. 3.

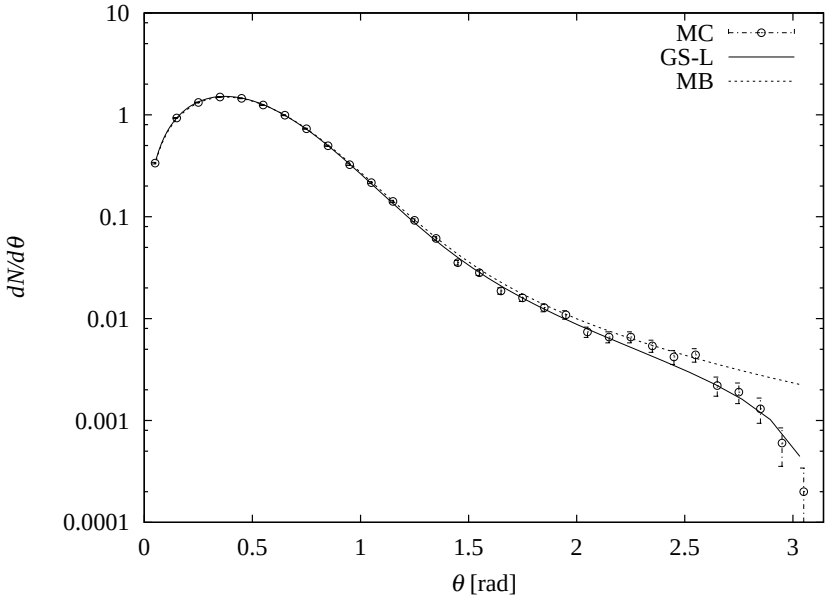

Figure 4: The probability densities of deflection angle, analytically expected by Molière-Bethe theory (dot line) and by Goudsmit-Saunderson theory (solid line), are compared with that evaluated by the Monte Carlo simulation (open circle) for 10 MeV electron, after dissipating half of its energy by ionization loss of 2.5 MeV in unit path-length of g/cm^2, neglecting the rest energy. The Monte Carlo results agree with Goudsmit-Saunderson results at the angular range where the small-angle approximations are no more satisfied.

4 Goudsmit-Saunderson angular distribution with ionization expressed by the Molière parameters B and $\theta_{\rm M}$

We found the Goudsmit-Saunderson angular distribution with ionization is expressed as

$$2\pi f_{\rm GS}(\theta,t) \;=\; \sum_{l=0}^{\infty}(l+\frac{1}{2})P_l(\cos\theta)\exp\{-\frac{\theta_{\rm M}^2}{4}l(l+1)(1-\frac{1}{B}[\ln\frac{\theta_{\rm M}^2}{4}+2\psi(l+1)])\}, \qquad (18)$$

corresponding to the Molière angular distribution $f_{\rm M}(\theta,t)2\pi\theta d\theta$ with ionization of

$$2\pi f_{\rm M}(\theta,t)=\int_0^{\infty}\zeta d\zeta J_0(\theta\zeta)\exp\{-\frac{\theta_{\rm M}^2\zeta^2}{4}(1-\frac{1}{B}\ln\frac{\theta_{\rm M}^2\zeta^2}{4})\}, \qquad (19)$$

using the same characteristic parameters B and $\theta_{\rm M}$ [4], according to the Lewis theory [12].

We have compared our Goudsmit-Saunderson distribution with ionization with the Monte Carlo result based on Rutherford cross-section without the small angle approximation [4] for 10 MeV electrons dissipating half of their energies by ionization loss of 2.5 MeV in each actual path-length in cm, neglecting the rest energy. The both results agree well as indicated in Fig. 4.

5 Conclusions

Molière distribution with ionization for arbitrary linear combination between the deflection angle $\vec{\theta}$ and the lateral displacement $\vec{r}$ is solved analytically, based on Kamata-Nishimura formulation of the theory. Derived lateral distribution agrees very well with our Monte Carlo result. Goudsmit-Saunderson angular distribution with ionization expressed by the Molière parameters B and $\theta_{\rm M}$

is confirmed to agree very well with our Monte Carlo result without the small angle approximation. These investigations will be helpful for our designing and analyses of experiments concerning charged particles and be useful for improving the accuracy and the efficiency in tracing charged particles by Monte Carlo simulations.

6 Acknowledgements

We are very much indebted to Prof. Jun Nishimura for useful discussions and many advices.

References

[1] G. Molière, Z. Naturforsch. **10a**, 177(1955).

[2] K. Kamata and J. Nishimura, Prog. Theor. Phys. Suppl. **6**, 93(1958).

[3] J. Nishimura, in *Handbuch der Physik, Band 46*, edited by S. Flügge (Springer, Berlin, 1967), Teil **2**, p. 1.

[4] T. Nakatsuka and K. Okei, *"Proceedings of the Third International Workshop on EGS,"* KEK Proceedings 2005-3, 47(2005).

[5] K. Okei and T. Nakatsuka, *"Proceedings of the Third International Workshop on EGS,"* KEK Proceedings 2005-3, 57(2005).

[6] G. Molière, Z. Naturforsch. **2a**, 133(1947).

[7] G. Molière, Z. Naturforsch. **3a**, 78(1948).

[8] H.A. Bethe, Phys. Rev. **89**, 1256(1953).

[9] S.A. Goudsmit and J.L. Saunderson, Phys. Rev. **57**, 24(1940).

[10] S.A. Goudsmit and J.L. Saunderson, Phys. Rev. **58**, 36(1940).

[11] W.T. Scott, Rev. Mod. Phys. **35**, 231(1963).

[12] H.W. Lewis, Phys. Rev. **78**, 526(1950).

[13] *Handbook of Mathematical Functions with Formulas, Graphs, and Mathematical Tables*, edited by M. Abramowitz and I.A. Stegun (Dover, New York, 1965), Chap. 6.

[14] W. Gröbner and N. Hofreiter, *Integraltafeln* (Springer, Wien, 1950), **I**.

[15] T. Nakatsuka, *"Proceedings of the Second International Workshop on EGS,"* KEK Proceedings 2000-20, 330(2000).

INCORPORATING COMBINATORIAL GEOMETRY TO THE EGS5 CODE AND ITS SPEED-UP

T. Sugita[1], T. Torii[2], A. Takamura[1]

[1]Science and System Laboratory Ltd., Tomobe, Ibaraki 309-1716, Japan
[2] Tsuruga Head Office, Japan Atomic Energy Agency, Tsuruga, Fukui 919-1279, Japan

Abstract

In order to calculate particle transport easily even in the case with various complex geometrical configurations, we have developed a CG (Combinatorial Geometry) user-routine in the EGS5 code. Furthermore, we have improved this routine for speed-up of the calculation. As the result, the calculation speed is several times faster than the original ones speed, and comparable with the speed with the non-CG routine.

1. Introduction

A user of the EGS code must make a user-routine for structuring geometry of calculation. Several years ago, we had developed a user code of EGS4/PRESTA [1, 2], named PRESTA-CG [3] to calculate the response of radiation detectors with complex geometry. Since the EGS4 updated to the EGS5 recently, we have developed a user-routine to apply a combinatorial geometrical method to the EGS5. In addition, we have improved the user-routine for speed-up of the calculation, and we have made a checking routine of that. In this paper, we describe the CG user-routine, and a routine for checking the region descriptions.

2. CG user-routine in EGS5

2.1 Geometry Description in the CG user-routine

The CG user-routine provides the solution of electron-photon transport calculation for users through three-dimensional multi-material geometry described by the CG method. In the combinatorial scheme, the problem input zones (regions) are built up out of simple bodies (fundamental shapes). In the present version of the CG user-routine, the bodies that can be used are as follows;

- RPP - Rectangular Parallelepiped,
- SPH - Sphere,
- RCC - Right Circular Cylinder,
- TRC - Truncated Right Angle Cone,
- TOR - Torus.

The definitions of the above bodies are illustrated in Appendix A. Each input zone is described as a combination that may consist of complex intersections, unions and differences of these bodies. We show examples in figure 1 and figure 2.

2.2 Management of Particle Stepping in EGS5

Subroutine HOWFAR in EGS5 calculates the distances between the particle position and surface of geometries and obtains a next region number. This subroutine is very important to use combinatorial geometry. We have made an extensible subroutine HOWFAR. We show the list of subroutine HOWFAR in appendix B and those arrangements in appendix C.

2.3 Searching Region Table to Speed up Calculation.

Furthermore, the calculation is sped up by using the region search table we made. In combinatorial geometry, boundaries connecting other regions with the original region are limited. However, it is difficult for users to describe the interrelation of the regions. If it is possible to obtain the region search table, the calculation will speed up. For the purpose of obtaining the region search table, we have made a subroutine RSTNXT. The subroutine RSTNXT calculates the correlation of every regions that related to a particle, and obtains the weighting factor for all regions with the possibility of flying the particle. At the time when some particles (ex. 10^4 histories) have calculated, the region search table created by this subroutine will be updated for newest one. In addition, it can be use to search a source region. These are carried out independently for electrons, positrons, and photons, respectively.

We show the parameters of subroutine RSTNXT.

```
subroutine rstnxt ( iq_np,    ir_np,        irnew)
```

charge of particle, present region number, next region number

2.4 Checking Region Routine

We have made subroutine GEOMCHK for checking region description. It is very useful for using the combinatorial geometry. This routine verifies whether there is a double-booking region, undefined region, the end region of particle-tracking, and the generation of particle with undefined region.

If a particle flights straightly, the subroutine GEOMCHK calculate the distance between the next boundary surface and the former surface / the present position. Next, GEOMCHK checks the region number at the mid points of those.

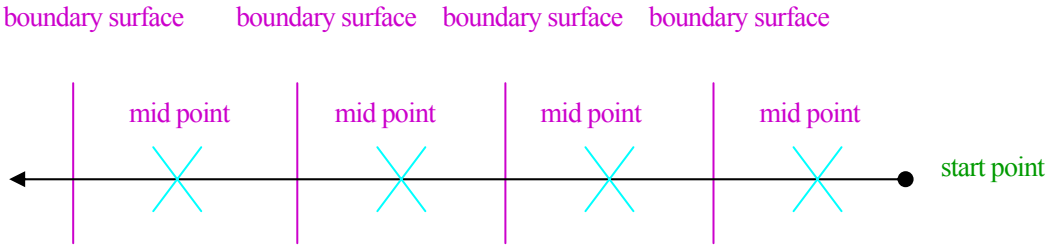

We describe the parameters of subroutine GEOMCHK. And we show the error messages in table 1.

```
subroutine geomchk (xin,yin,zin,  uin,vin,win,  ierrcnt,        ifto)
```

start point, direction, error counter, message output unit

3. Application of CG user-routine.

3.1 Model of Calculations

In order to verify the CG user-routine, we calculated two samples.

First, we calculated the dose rate in a water phantom (used ucphantomcgv file).

Used regions : 24.
Used geometries : 25 RPP.
Tracking area : 15 cm×15 cm×30 cm.
World area : 20 cm×20 cm×40 cm.
Used materials : 3 kinds.

Next, we calculated the response function of a NaI detector (used ucnaicgv file).

Used regions : 5.
Used geometries : 5 RCC.
Tracking area : φ 8.81 cm×h 8.72 cm.
World area : φ 10 cm×h 10 cm.
Used materials : 2 kinds.

We show result in table 2.

4. Conclusions

We have developed a CG user-routine, which incorporates the CG method in EGS5, and compared the time of calculations. We have verified that the calculation using this routine is very fast compared with the former routine. Furthermore, we have made a checking routine of CG description. The calculation of EGS5 that used the CG method became very convenient by this improvement, and it can be applicable to various fields of the transport calculation.

Acknowledgments

We are grateful to Prof. H. Hirayama and Dr. Y. Namito of KEK for their encouragement of this work.

References

1) W.R. Nelson, H. Hirayama, and D.W.O. Rogers, SLAC-265 (1985).
2) D.W.O. Rogers, Nucl. Instr. And Meth., 199, 531 (1982).
3) T. Torii, T. Sugita, Development of PRESTA-CG Incorporating Combinatorial Geometry in EGS4/PRESTA, JNC TN1410 2002-001 (2002).

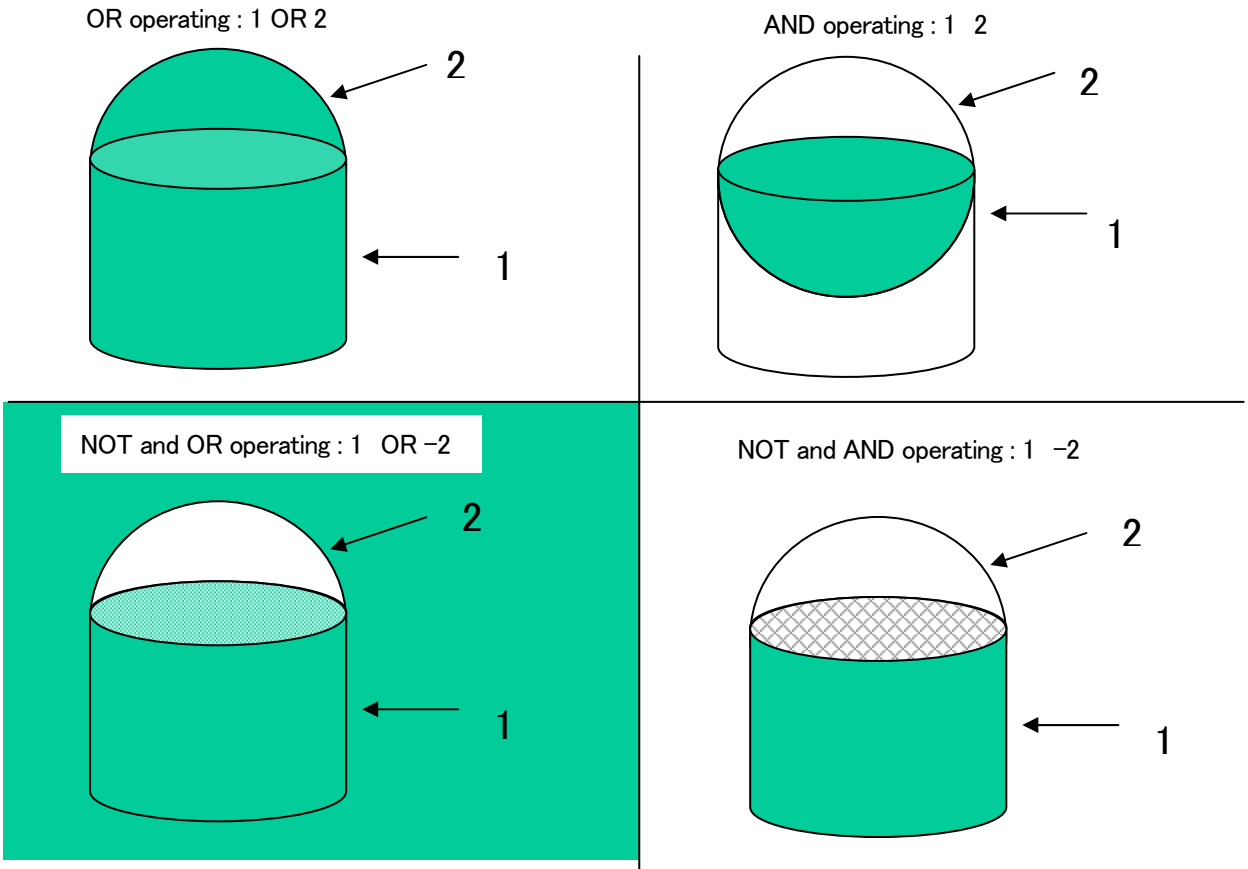

Figure 1. An example of description for using combinatorial geometry method (1).

```
RCC   1     -5   -5    0    10    10    0      30          inclined cylinder 1
RCC   2      0   -5   -5     0    10    10     30          inclined cylinder 2
RCC   3     -5    0   -5    10     0    10     30          inclined cylinder 3
END
Z01          1    2    3                                  AND operating : 1  2  3
END
```

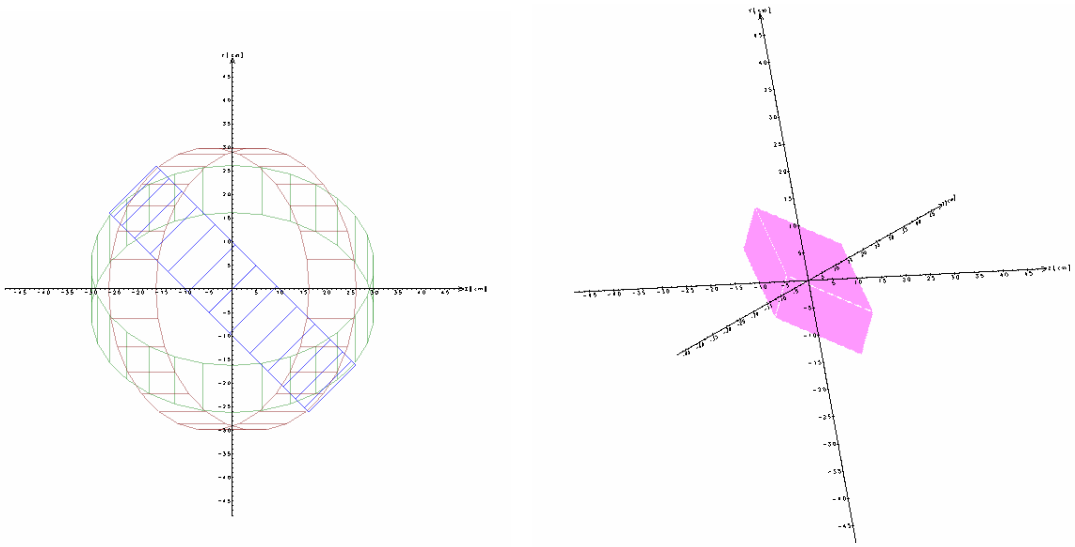

Figure 2. An example of description for using combinatorial geometry method (2).

Table 1. The error messages of geometry checking

① A Example of error message (1)

```
 geometry check start
 Geometry error : Non stopping zone x,y,z,u,v,w=  4.7050E+00  0.0000E+00  2.5494E-01  9.9854E-01  0.0000E+00  5.4105E-02
 Geometry error : Non stopping zone x,y,z,u,v,w=  4.7050E+00  0.0000E+00  2.9139E+00  8.5016E-01  0.0000E+00  5.2652E-01
 Geometry error : Non stopping zone x,y,z,u,v,w=  4.7050E+00  0.0000E+00  2.2833E-01  9.9882E-01  0.0000E+00  4.8472E-02
 Geometry error : Non stopping zone x,y,z,u,v,w=  4.7050E+00  0.0000E+00  3.2664E+00  8.2145E-01  0.0000E+00  5.7028E-01
 Geometry error : Double zone       x,y,z,u,v,w=  3.7928E+00  0.0000E+00  8.2575E+00  4.1739E-01  0.0000E+00  9.0873E-01
 Geometry error : izone_tbl=    3    4
 Geometry error : Non stopping zone x,y,z,u,v,w=  4.0695E+00  0.0000E+00  8.8600E+00  4.1739E-01  0.0000E+00  9.0873E-01
 Geometry error : Non stopping zone x,y,z,u,v,w=  4.7050E+00  0.0000E+00  4.4844E+00  7.2387E-01  0.0000E+00  6.8993E-01
 Geometry error : Non stopping zone x,y,z,u,v,w=  4.7050E+00  0.0000E+00  4.5632E-01  9.9533E-01  0.0000E+00  9.6534E-02
 Geometry error : Non stopping zone x,y,z,u,v,w=  4.7050E+00  0.0000E+00  1.5475E+00  9.4994E-01  0.0000E+00  3.1245E-01
 Geometry error : Non stopping zone x,y,z,u,v,w=  4.7050E+00  0.0000E+00  1.0762E+00  9.7482E-01  0.0000E+00  2.2298E-01
                                                   x point     y point    z point     x direction  y direction  z direction
 Geometry error count=         10
```

This is a message that a geometry checking has done.

The stopping region has non-zero material number.

The point has two regions.

The point has the region numbers.

This is the count of errors.
If it has over 10 then the calculation has be exited.

② A Example of error message (2)

```
 geometry check start
 Geometry error : Non next zone     x,y,z,u,v,w=  3.7928E+00  0.0000E+00  8.2575E+00  4.1739E-01  0.0000E+00  9.0873E-01
 Geometry error : Non next zone     x,y,z,u,v,w=  3.9076E+00  0.0000E+00  8.5075E+00  4.1739E-01  0.0000E+00  9.0873E-01
 Geometry error : Non next zone     x,y,z,u,v,w=  1.4016E+00  0.0000E+00  8.4700E+00  1.6326E-01  0.0000E+00  9.8658E-01
 Geometry error : Non next zone     x,y,z,u,v,w=  3.0349E+00  0.0000E+00  8.4700E+00  3.3731E-01  0.0000E+00  9.4139E-01
 Geometry error : Non next zone     x,y,z,u,v,w=  3.5269E+00  0.0000E+00  8.4700E+00  3.8440E-01  0.0000E+00  9.2317E-01
 Geometry error : Non next zone     x,y,z,u,v,w=  3.4625E+00  0.0000E+00  8.4700E+00  3.7840E-01  0.0000E+00  9.2564E-01
 Geometry error : Non next zone     x,y,z,u,v,w=  1.3199E+00  0.0000E+00  8.4700E+00  1.5397E-01  0.0000E+00  9.8808E-01
 Geometry error : Non next zone     x,y,z,u,v,w=  3.6421E+00  0.0000E+00  8.4700E+00  3.9503E-01  0.0000E+00  9.1867E-01
 Geometry error : Non next zone     x,y,z,u,v,w=  3.3035E+00  0.0000E+00  8.4700E+00  3.6337E-01  0.0000E+00  9.3165E-01
 Geometry error : Non next zone     x,y,z,u,v,w=  2.0676E+00  0.0000E+00  8.4700E+00  2.3715E-01  0.0000E+00  9.7147E-01

 Geometry error count=         10
```

The point is not included in any regions.

③ A Example of no error message

```
 geometry check start

 Geometry error count=         0
```

This shows no error.

Table 2. The calculation times of the EGS codes.

unit of time:sec

User code name	Number of particles	First CG model (same EGS4)	Second CG model (2004)	New CG model (2005)	Non CG model	Comments
ucphantomcgv	0	7.562	7.468	7.515	7.483	First try
		7.515	7.530	7.468	7.452	second try
		7.515	7.499	7.436	7.499	third try
		22.592	22.497	22.419	22.434	sum
		7.531	7.499	7.473	7.478	average
		1.000	0.996	0.992	0.993	factor by first CG model
		1.004	1.000	0.997	0.997	factor by second CG model
		1.007	1.003	0.999	1.000	factor by non CG model
	100,000	70.921	23.061	15.249	14.937	First try
		71.202	23.577	15.421	14.968	second try
		70.140	23.186	15.734	15.140	third try
		212.263	69.824	46.404	45.045	sum
		70.754	23.275	15.468	15.015	average
		1.000	0.329	0.219	0.212	factor by first CG model
		3.040	1.000	0.665	0.645	factor by second CG model
		4.712	1.550	1.030	1.000	factor by non CG model
	at shower call	63.224	15.776	7.995	7.537	average
		1.000	0.250	0.126	0.119	factor by first CG model
		4.008	1.000	0.507	0.478	factor by second CG model
		8.388	2.093	1.061	1.000	factor by non CG model
ucnaicgv	0	9.452	9.531	9.421	9.530	First try
		9.452	9.436	9.499	9.608	second try
		9.452	9.499	9.468	9.609	third try
		28.356	28.466	28.388	28.747	sum
		9.452	9.489	9.463	9.582	average
		1.000	1.004	1.001	1.014	factor by first CG model
		0.996	1.000	0.997	1.010	factor by second CG model
		0.986	0.990	0.988	1.000	factor by non CG model
	100,000	151.968	89.968	71.546	43.671	First try
		149.608	93.499	71.749	43.515	second try
		151.812	96.327	68.858	43.890	third try
		453.388	279.794	212.153	131.076	sum
		151.129	93.265	70.718	43.692	average
		1.000	0.617	0.468	0.289	factor by first CG model
		1.620	1.000	0.758	0.468	factor by second CG model
		3.459	2.135	1.619	1.000	factor by non CG model
	at shower call	141.677	83.776	61.255	34.110	average
		1.000	0.591	0.432	0.241	factor by first CG model
		1.691	1.000	0.731	0.407	factor by second CG model
		4.154	2.456	1.796	1.000	factor by non CG model

Appendix A　　Body Definition

A) Rectangular Parallelepiped (RPP)

Specify the minimum and maximum values of x-, y-, and z-coordinates that bound a rectangular parallelepiped whose six sides are perpendicular to the coordinate axes.

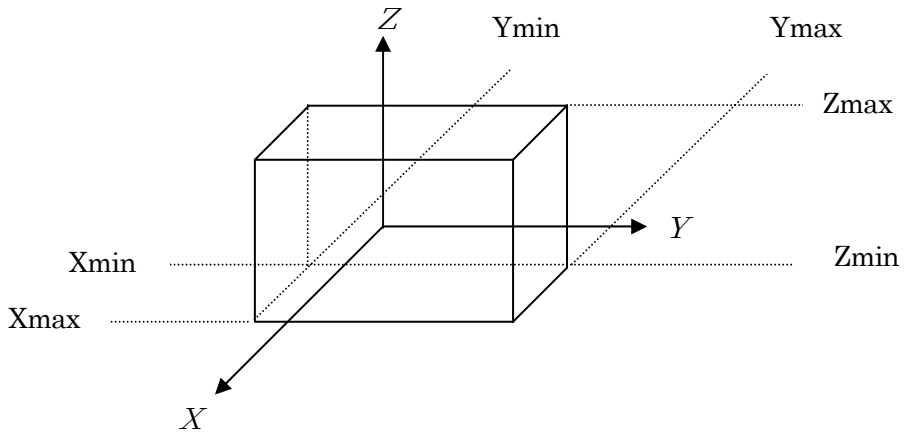

B) Sphere (SPH)

Specify the components of the radius vector **V** to the center of the sphere and the radius R of the sphere.

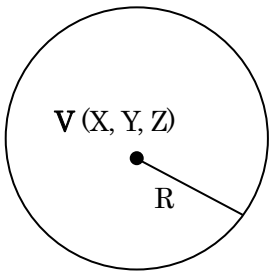

C) Right Circular Cylinder (RCC)

Specify the components of a radius vector **V** to the center of one base, the components of a vector **H** from the center of that base to the center of the other base, and the radius of the cylinder.

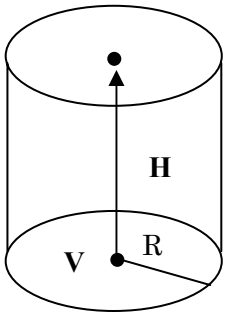

D) Truncated Right Angle Cone (TRC)

Specify the components of a radius vector **V** to the center of one base, the components of a vector **H** from the center of that base to the center of the other base, and the radii R1 and R2 of the lower and upper bases, respectively.

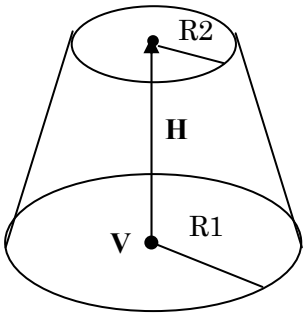

E) Torus (TOR)

Specify the components of a radius vector **V** to the center of the torus, and the torus is configured parallel to one of the axes. R1 is the length between the center of torus and the center of tube, and R2 is the radius of the tube. Also, input the direction number of torus (n: x/y/z-axis = 1/2/3). Furthermore, input starting angle θ1 and ending angle θ2 of the sector for the calculation of a part of torus. For the calculation of "complete" torus, set θ1=0, and θ2=360, respectively.

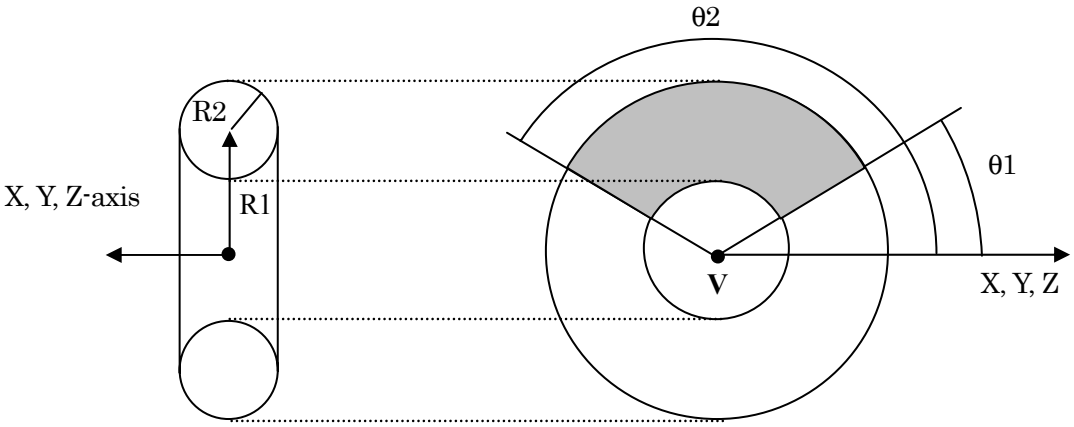

Table A1 Data required to described each body type

Body Type	Inp. #	Real Data Defining Particular Body					
RPP	#	Xmin	Xmax	Ymin	Ymax	Zmin	Zmax
SPH	#	Vx	Vy	Vz	R		
RCC	#	Vx	Vy	Vz	Hx	Hy	Hz
	R						
TRC	#	Vx	Vy	Vz	Hx	Hy	Hz
	R1	R2					
TOR	#	Vx	Vy	Vz	R1	R2	
		θ1	θ2	n			

Appendix B　List of Subroutine HOWFAR

```
      implicit none
c
      include 'include/egs5_h.f'        ! Main EGS "header" file
      include 'include/egs5_epcont.f'   ! COMMONs required by EGS5 code
      include 'include/egs5_stack.f'
      include 'auxcommons/cg/geom_common.f' ! geom-common file
c
c
      integer i,j,jjj,ir_np,nozone,jty,kno
      integer irnear,irnext,irlold,irlfg,itvlfg,ihitcg
      double precision xidd,yidd,zidd,x_np,y_np,z_np,u_np,v_np,w_np
      double precision tval,tval0,tval00,tval10,tvalmn,delhow
      double precision atvaltmp
      integer iq_np
c
      ir_np = ir(np)                    !region number
      iq_np = iq(np) + 2                !kind of particle
c
      if(ir_np.le.0) then
        write(6,*) 'Stopped in howfar with ir(np) <=0'
        stop
      end if
c
      if(ir_np.gt.izonin) then
        write(6,*) 'Stopped in howfar with ir(np) > izonin'
        stop
      end if
c
      if(ir_np.EQ.izonin) then
        idisc=1                         !tracking stop
        return
      end if
      tval=1.d+30
      itvalm=0
c     body check
      u_np=u(np)
      v_np=v(np)
      w_np=w(np)
      x_np=x(np)
      y_np=y(np)
      z_np=z(np)
      do i=1,nbbody(ir_np)          !number of geometries structuring now region
        nozone=ABS(nbzone(i,ir_np))     ! geometry number
        jty=itblty(nozone)
        kno=itblno(nozone)
c     rpp check
        if(jty.eq.ityknd(1)) then
          if(kno.le.0.or.kno.gt.irppin) go to 190
```

Direction of a particle

Position of a particle

Calculate the distances between the particle position and surface of geometries

```
          call rppcg1(kno,x_np,y_np,z_np,u_np,v_np,w_np)
c     sph check
        elseif(jty.eq.ityknd(2)) then
          if(kno.le.0.or.kno.gt.isphin) go to 190
          call sphcg1(kno,x_np,y_np,z_np,u_np,v_np,w_np)
c     rcc check
        elseif(jty.eq.ityknd(3)) then
          if(kno.le.0.or.kno.gt.irccin) go to 190
          call rcccg1(kno,x_np,y_np,z_np,u_np,v_np,w_np)
c     trc check
        elseif(jty.eq.ityknd(4)) then
          if(kno.le.0.or.kno.gt.itrcin) go to 190
          call trccg1(kno,x_np,y_np,z_np,u_np,v_np,w_np)
c     tor check
        elseif(jty.eq.ityknd(5)) then
          if(kno.le.0.or.kno.gt.itorin) go to 190
          call torcg1(kno,x_np,y_np,z_np,u_np,v_np,w_np)
c**** add new geometry in here
       end if
  190  continue
      end do
      irnear=ir_np
      if(itvalm.eq.0) then
        tval0=cgeps1
        xidd=x_np+tval0*u_np
        yidd=y_np+tval0*v_np
        zidd=z_np+tval0*w_np
  310   continue
          if(x_np.ne.xidd.or.y_np.ne.yidd.or.z_np.ne.zidd) goto 320
          tval0=tval0*10.d0
          xidd=x_np+tval0*u_np
          yidd=y_np+tval0*v_np
          zidd=z_np+tval0*w_np
          go to 310
  320   continue
        call srzone(xidd,yidd,zidd,iq_np,ir_np,irnext)
        if(irnext.ne.ir_np) then
          tval=0.0d0
          irnear=irnext
        else
          tval00=0.0d0
          tval10=10.0d0*tval0
          irlold=ir_np
          irlfg=0
  330     continue
          if(irlfg.eq.1) go to 340
            tval00=tval00+tval10
            if(tval00.gt.1.0d+06) then
              write(6,9000) iq(np),ir(np),x(np),y(np),z(np),
     &                      u(np),v(np),w(np),tval00
```

```
 9000 format(' TVAL00 ERROR : iq,ir,x,y,z,u,v,w,tval=',
     &       2I3,1P7E12.5)
              stop
            end if
            xidd=x_np+tval00*u_np
            yidd=y_np+tval00*v_np
            zidd=z_np+tval00*w_np
            call srzold(xidd,yidd,zidd,irlold,irlfg)
            go to 330
  340     continue
          tval=tval00
          do j=1,10
            xidd=x_np+tval00*u_np
            yidd=y_np+tval00*v_np
            zidd=z_np+tval00*w_np
            call srzone(xidd,yidd,zidd,iq_np,irlold,irnext)
            if(irnext.ne.irlold) then
              tval=tval00
              irnear=irnext
            end if
            tval00=tval00-tval0
          end do
          if(ir_np.eq.irnear) then
            write(0,*) 'ir(np),tval=',ir_np,tval
          end if
        end if
      else
        do j=1,itvalm-1
          do i=j+1,itvalm
            if(atval(i).lt.atval(j)) then
              atvaltmp=atval(i)
              atval(i)=atval(j)
              atval(j)=atvaltmp
            endif
          enddo
        enddo
        itvlfg=0
        tvalmn=tval
        do jjj=1,itvalm                  ! number of crossing points at boundary surface
          if(tvalmn.gt.atval(jjj)) then
            tvalmn=atval(jjj)
          end if
          delhow=cgeps2
          tval0=atval(jjj)+delhow
          xidd=x_np+tval0*u_np
          yidd=y_np+tval0*v_np
          zidd=z_np+tval0*w_np
  410     continue
          if(x_np.ne.xidd.or.y_np.ne.yidd.or.z_np.ne.zidd) go to 420
            delhow=delhow*10.d0
```

```
          tval0=atval(jjj)+delhow
          xidd=x_np+tval0*u_np
          yidd=y_np+tval0*v_np
          zidd=z_np+tval0*w_np
        go to 410
420     continue
        call srzone(xidd,yidd,zidd,iq_np,ir_np,irnext)  ! get a region number
        if((irnext.ne.ir_np.or.atval(jjj).ge.1.).and.
     &       tval.gt.atval(jjj)) THEN
          tval=atval(jjj)                          ! length
          irnear=irnext                            ! region number
          itvlfg=1
          goto 425
        end if
      end do
425   continue
      if(itvlfg.eq.0) then
        tval0=cgmnst
        xidd=x_np+tval0*u_np
        yidd=y_np+tval0*v_np
        zidd=z_np+tval0*w_np
430     continue
        if(x_np.ne.xidd.or.y_np.ne.yidd.or.z_np.ne.zidd) go to 440
          tval0=tval0*10.d0
          xidd=x_np+tval0*u_np
          yidd=y_np+tval0*v_np
          zidd=z_np+tval0*w_np
          go to 430
440     continue
        if(tvalmn.gt.tval0) then
          tval=tvalmn
        else
          tval=tval0
        end if
      end if
    end if
    ihitcg=0
    if(tval.le.ustep) then
      ustep=tval            !length of next region
   ihitcg=1
    end if
    if(ihitcg.eq.1) THEN
      if(irnear.eq.0) THEN
        write(6,9200) iq(np),ir(np),x(np),y(np),z(np),
     &                u(np),v(np),w(np),tval
9200 format(' TVAL ERROR : iq,ir,x,y,z,u,v,w,tval=',2I3,1P7E12.5)
        idisc=1
        itverr=itverr+1
        if(itverr.ge.100) then
          stop
```

```
    end if
    return
  end if
  irnew=irnear                    ! next region number
  if(irnew.ne.ir_np) then
    call rstnxt(iq_np,ir_np,irnew)  ! update a region search table
  endif
end if
return
end
```

Appendix C List of Include File GEOM_COMMON.F

```
      integer  MAX_BODY,MAX_ZONE,MAX_TVAL,MAX_GEOM,MAX_GTYPE,
     &         MAX_RPP,MAX_SPH,MAX_RCC,MAX_TRC,MAX_TOR
      parameter (MAX_BODY=72,MAX_ZONE=200,MAX_TVAL=800,
     &           MAX_GEOM=500,MAX_GTYPE=10,
     &           MAX_RPP=100,MAX_SPH=100,MAX_RCC=100,
     &           MAX_TRC=100,MAX_TOR=100)
      integer MAX_IZN
      parameter (MAX_IZN=200)
c
      double precision atval
      integer itvalm,itverr
      common/TVALCG/atval(MAX_TVAL),itvalm,itverr
      integer nbzone,nbbody,izonin
      common/ZONDTA/ nbzone(MAX_BODY,MAX_ZONE),nbbody(MAX_ZONE),izonin,
     &               zoneid(MAX_ZONE),zoneor(MAX_BODY,MAX_ZONE)
      character zoneid*3,zoneor*2
      double precision rpppnt
      integer nbrpp,irppin,irppuse
      common/RPPDTA/rpppnt(6,MAX_RPP),nbrpp(MAX_RPP),irppin,
     &              irppuse(MAX_RPP)
      double precision sphpnt
      integer nbsph,isphin,isphuse
      common/SPHDTACG/sphpnt(4,MAX_SPH),nbsph(MAX_SPH),isphin,
     &              isphuse(MAX_SPH)
      double precision rccpnt
      integer nbrcc,irccin,irccuse
      common/RCCDTA/rccpnt(7,MAX_RCC),nbrcc(MAX_RCC),irccin,
     &              irccuse(MAX_RCC)
      double precision trcpnt
      integer nbtrc,itrcin,itrcuse
      common/TRCDAT/trcpnt(8,MAX_TRC),nbtrc(MAX_TRC),itrcin,
     &              itrcuse(MAX_TRC)
      double precision torpnt
      integer nbtor,itorin,itoruse
      common/TORDTA/torpnt(8,MAX_TOR),nbtor(MAX_TOR),itorin,
     &              itoruse(MAX_TOR)
      integer itblty,itblno,ityknd,igmmax,itbody
      common/GEOMID/itblty(MAX_GEOM),itblno(MAX_GEOM),
     &              ityknd(MAX_GTYPE),igmmax,itbody
      integer iznnxc,iznnxt,iznnxp,iznnxs
      common/ZONNXT/iznnxc(3,MAX_ZONE,0:MAX_ZONE),
     &              iznnxt(3,MAX_ZONE,0:MAX_ZONE),
     &              iznnxp(3,MAX_ZONE,0:MAX_ZONE),iznnxs(3,2)
      double precision cgmnst,cgeps1,cgeps2
      data cgmnst/1.0d-4/
      data cgeps1/1.0d-4/
      data cgeps2/1.0d-4/
      double precision rcceps,trceps
```

Maximum number of the arrangements

The arrangements for pushing the distances

The arrangements of the regions

The arrangements of RPP

The arrangements of SPH

The arrangements of RCC

The arrangements of TRC

The arrangements of TOR

The arrangements of geometry

The arrangements for searching next region

```
data rcceps/1.0d-4/
data trceps/1.0d-4/
integer irynow,ilpnow
common /CMLOOP/irynow,ilpnow
```

APPLICATIONS OF EGS4 MONTE CARLO SIMULATION FOR X-RAY SOURCE CHARACTERIZATION AND POTABLE X-RAY FLUORESCENCE SPECTROSCOPY

I. Sakai[1], T. Utaka[1], S. Maeo[1], K. Kuzushita[1], I. Sugimoto[2], D. Nomoto[1], and K. Taniguchi[1]

[1]Division of Electronics and Applied Physics,
Osaka Electro-Communication University, Osaka 572-8530, Japan
[2]Technical Research Institute, HITACHI ZOSEN CORPORATION, Osaka 606-8507, Japan
e-mail: i-sakai@isc.osakac.ac.jp

Abstract

We applied EGS4 Monte Carlo (MC) simulation to the spectral evaluation of the primary x-ray beam from low-power x-ray tube and the prediction of the energy-dispersive x-ray fluorescence (ED-XRF) analysis of metals. The end-window type of small x-ray tube with Mo anode was adopted to observe the backscattered component of the primary x-ray beam under the condition of low power (<50 kV, <1 μA). For estimation of the filtration effect on the primary x-ray beam, the set of Si and Mo sheet optimized for harmful heavy elements analysis were used. On the other hand, the ED-XRF spectra of metals were recorded using a portable spectrometer with LiF bend monochromator which enables simple measurement situation. In all measurement situations MC calculations were done using low energy extension of EGS4 code, and the experimental data can be compared directly with the simulated spectrum. Results showed that the EGS4 MC calculations are useful method for spectral evaluation of x-ray tube and analysis of ED-XRF measurement.

1. Introduction

A number of studies for x-ray generation by electron beam bombardment of target materials were made in various measurement situations including the conventional x-ray tube source, for examples in Ref. 1- 4. However, there remains the question whether energy and spatial distribution of emitted x-ray by expected by theory hold in small low energy x-ray tube source situations. On the other hand, unique design of mono-energetic x-ray tube has been proposed, in which angle distribution of the x-ray beam is effectively used [5]. The detailed simulation of these x-ray source and systematic set of measurement are important issue for the development of the x-ray tube.

The nondestructive quantitative characterization technique is demanded for variety of environmental and industrial applications. X-ray fluorescent studies are among the most powerful tools for quantification procedure. Portable energy-dispersive x-ray fluorescence (ED-XRF) spectrometer for handled use is suitable for harmful heavy elements and the other materials (Cd, As, Br, Pb , Se, Hg) in environmental applications, for example seen in Ref 6. We have performed the ED-XRF measurement of metals using a portable spectrometer. The obtained data were directly compared with the results of EGS4 Monte Carlo (MC) simulations corrected for the detector response. The MC calculation well reproduced experimental spectrum. The resulting measurements are described in the following sections.

2. Experimental procedure

2.1 Measurement of primary x-ray beam from end-window type x-ray tube

Structure of the end-window type x-ray tube allows the quasi 90˚ incident direction of electron beam against a surface of target material and the observation angle of 90˚. Figure 1 shows a schematic drawing of measurement set-up of primary x-ray beam spectrum from x-ray tube. The x-ray tube is an end-window type with Mo anode (Varian VF-50J). The emitted x-ray beam was generated by bombardment of 30 kV electron beam of Mo target material. The primary x-ray beam was taken out through the extraction beryllium window of 25 micron thickness and introduced into the CdTe detector (AmpTek XR100CR). The energy spectrum was measured when the x-ray tube voltage and tube current are 30 kV and 0.3 μA respectively.

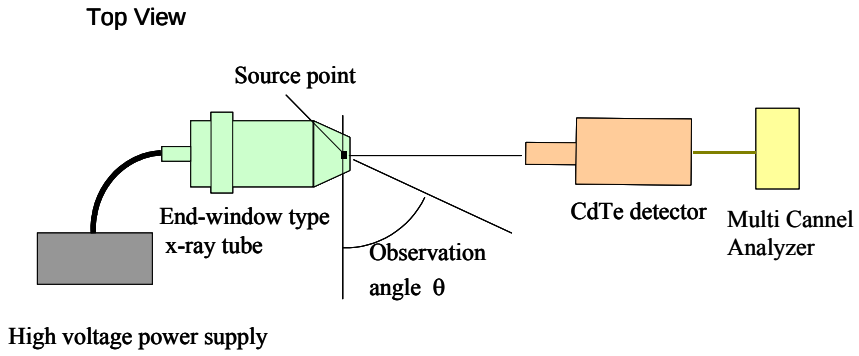

Figure 1. Schematic drawing of measurement set-up of primary x-ray beam spectra from end-window type x-ray tube

2.2 Measurement of filtered primary x-ray beam from end-window type x-ray tube

Figure 2 shows the schematic representation of experimental configuration for filtered primary x-ray beam spectrum in ED-XRF spectroscopy system. The X-ray source is the end-window type with W anode (Varian VF-50J, 50 kV max). The x-ray tube current was controlled below 1 μA for decrease count rate of detector. Si sheet with thickness of 1.5 mm and Mo sheet with thickness of 0.3 mm are set to extract the optimal energy distribution for ED-XRF of heavy metals and the other materials.

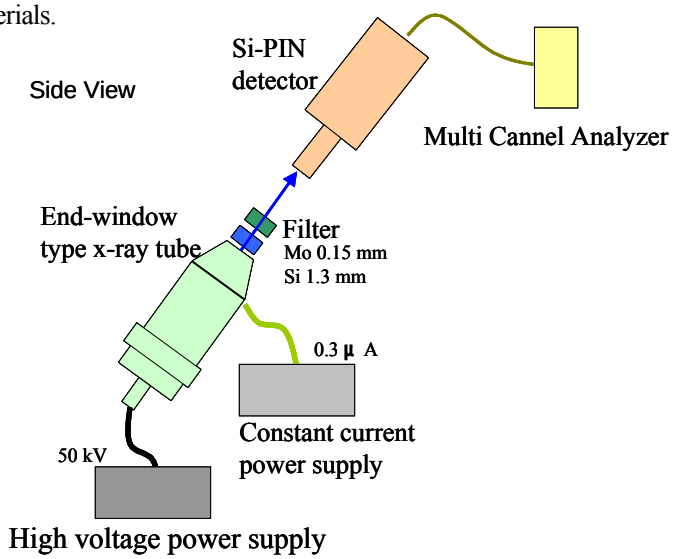

Figure 2. Schematic representation of experimental configuration for filtered x-ray beam spectra. from end-window type x-ray tube.

2.3 Portable energy dispersive x-ray fluoresence spectrometer

EGS4 MC calculation can be applied to quantitative analysis of XRF spectra. Figure 3 shows a photograph of the portable ED-XRF spectrometer (RIGAKU PORTARIX). The instrument consists of Mo x-ray tube, curved LiF crystal monochrometor and Si-PIN detector. The availabl x-ray energy is 17.4 keV and is focused on the sample position. We measured the x-ray fluorescence spectra of stainless steel SUS304 and bearing steel SUJ2.

Figure 3. A photograph of a portable ED-XRF spectrometer (RIGAKU PORTARIX).

3. Results

3.1 Primary x-ray beam spectrum of Mo x-ray tube

Figure 4 shows the measured spectrum of primary x-ray beam from Mo x-ray tube. The MC calculation was done in the range of photon energy above 5 keV and observation angle between 85˚to 90˚. To compare the obtained data with MC calculation, the correction of the detector resolution function were made for the MC calculation. The intensity of fluorescence lines of Mo-K α〈 (17.4 keV) and K β_1 (19.7 keV) fit well to MC calculation. It is seen that the deviations between the simulated and experimental distribution is considerable in low energy side, suggesting that the effect of thickness of target material appeared.

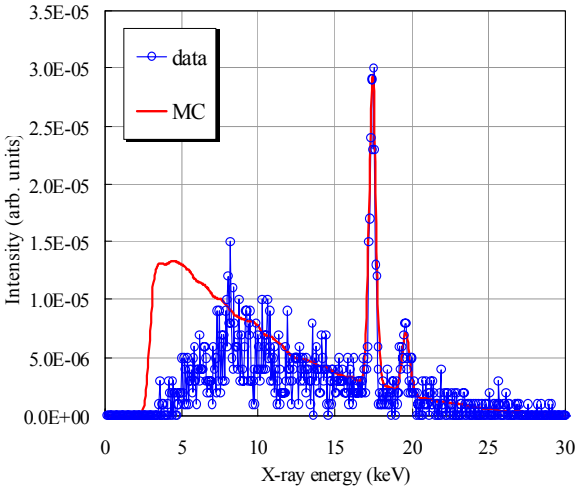

Figure 4. Measured and calculated energy spectrum of primary x-ray beam from Mo x-ray tube.

3.2 Filtered x-ray beam spectrum of W x-ray tube

The filtered x-ray beam of W x-ray tube formed by two set of filters is shown in Fig. 5. The corrections of the MC calculation were made for the detection efficiency and energy resolution of Si-PIN detector. The peak on the left side at 20.0 keV shows Mo absorption edge. The calculated peak position shifts by a few hundred electron volts from the measured value. The shift comes from the uncertainties of the response function of the detector. Taking into account of the fact, the data points fit well to a MC calculation.

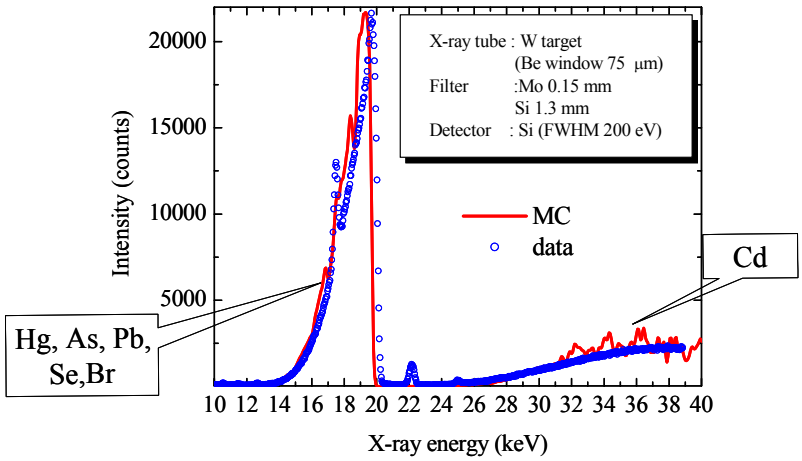

Figure 5. Measured and calculated energy spectrum of filtered primary x-ray beam from W x-ray tube.

3.3 Energy dispersive x-ray fluoresence spectra of metals

EGS4 MC calculation was applied to ED-XRF analysis of metals. The results of ED-XRF measurement of stainless steel SUS304 and bearing steel SUJ2 are compared with the MC calculations as shown in Fig. 6 and 7 respectively. The correction of the detector response was made for the MC calculations. The data fit well MC calculation, indicating that EGS 4 MC calculation is useful for quantitative ED-XRF analysis. The calculated profile of Cr-K β is somewhat small, suggesting that the absorption effect in a sample sickness.

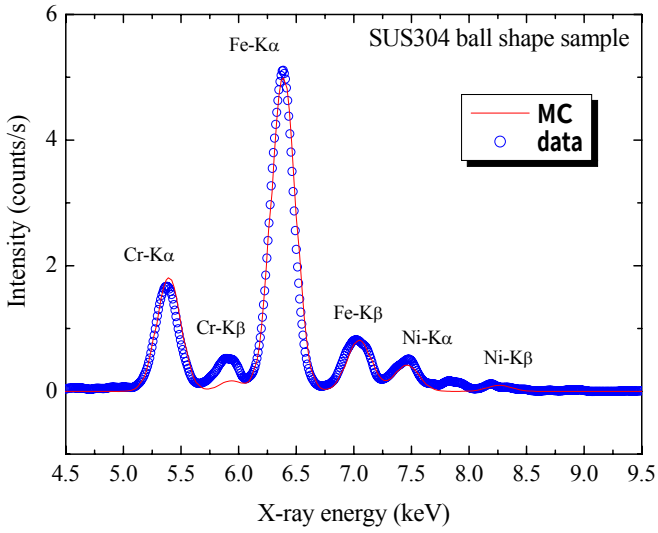

Figure 6. ED-XRF analysis of stainless steel SUS304.

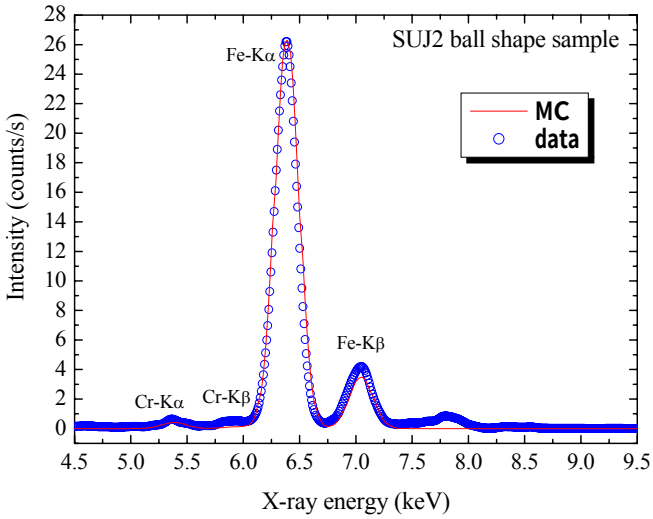

Figure 7. ED-XRF analysis of bearing steel of SUJ2.

4. Discussion

Our results show that the MC calculation using the low extension of EGS4 code is applicable method for the evaluation of the x-ray beam spectrum from x-ray tube and the quantitative analysis of ED-XRF measurement.

For the validation of the primary x-ray beam spectrum in low energy region, it is necessary to take into account the effect of material thickness and the other possible sources of error in measurement. We have begun to construct x-ray tube having an appropriate structure for the investigation of the energy and spatial distribution of the primary x-ray beam. It will supply the simple and useful measurement situations in the comparison with MC calculations.

Our primary aim was to perform the preliminary study of the applications of EGS4 MC simulation to the ED-XRF measurements. The reasonable responses of ED-XRF were obtained. The MC simulation combined with the portable ED-XRF analysis will be useful to judgment of the kind of materials as well as quantitative analysis. Next step is to search for applications to the standard materials in various measurement situations.

Acknowledgments

This work was partially supported by Japan Science and Technology agency Grants.

References

1) S. FLÜGGE, HANDBUCH DER PHYSIK, RÖNTGENSTRAHLEN, BERLIN·GÖTTINGEN·HEIDELBERG, SPRINGER-VERLAG, 1957.
2) R. C. PLACIOUS, "Dependence of 50- and 100-keV Bremsstrahlung on Target Thicknes, Atomic Nimber, and Geometric Factors" J. of Appl. Phys. **38**, 2030-2038 (1967).
3) J. H. McCrary, L. V. Singman, L. H. Ziegler, L. D. Looney, C. M. Edmonds, and Carolyn E. Harris, "K-Fluoresent-X-Ray Relative-Intensity MeasuementsMonte," Phys. Rev A. **4**, 1745-1750 (1971).
4) E. Acosta, X. Llovet, E. Coleoni, J. A. Riveros, F. Salvat, "Monte Carlo simulation of x-ray emission by kilovolt electron bombardment," J. of Appl. Phys. **11**, 6038-6049 (1998).
5) E. Sato, E. Tanaka, H. Mori, T. Kawai, S. Sato and K. Takayaam "Clean monochromatic x-ray irradiation from weakly ionized linear copper plasma" Opt. Eng., **44**, 049002-1-6, (2005).
6) T. Sanada, A. Hokura, I. Nakai, S. Maeo, S. Nomura, K. Taniguchi, T. Utaka and S. Yoshimura, "On site Analysis of Archaeological Samples at the Abusir South Hill Remains in Egypt by Newly Developed Portable X-ray Floresence Spectrometer" Adv. X-Ray. Chem. Anal., Japan **34**, 289-306, (2002).

FLUCTUATIONS OF ELECTRON AND PHOTON FLUX BY A THUNDERCLOUD ELECTRIC FIELD AND THE RUNAWAY AIR BREAKDOWN.

T. Torii and T. Sugita[†]

Tsuruga Head Office, Japan Atomic Energy Agency, Tsuruga 919-1279, Japan

[†]*Science System Laboratory Inc., Tomobe 309-1716, Japan*

Abstract

In recent years, fluctuations in the radiation intensity within or above thunderclouds have occasionally been observed by aircraft, balloons and artificial satellites equipped with radiation detectors within and above the upper atmosphere. The fluctuations on the ground which seemed to be caused by thunderstorm activity have also been detected on the coastal area facing the Sea of Japan during winter thunderstorm activities. Then, assuming the injection of primary cosmic-rays at the upper atmosphere, the generation of secondary cosmic-rays are calculated by the GEANT4 code. Furthermore, in order to simulate the transport of energetic electrons produced by secondary cosmic-rays in a winter thundercloud electric field, we have made a user code of the EGS5 code incorporating the effect of external electric fields. We have also carried out the transport analysis of energetic electrons within and below the thundercloud. As the result, it is confirmed that the electron and photon flux increased rapidly in the region with high electric field. In particular, since the density of electron flux increases greatly in the high field region, it is suggested that the runaway air breakdown can be occurred by the generation of the electromagnetic shower as the result of the injection of energetic radiation.

1 Introduction

Increases in gamma-ray dose-rate associated with winter thunderstorm activity have been observed by environmental radiation monitors and other radiation detectors around nuclear facilities facing the Sea of Japan [1]. The energy of enhanced gamma-rays is up to several MeV, and the duration is several tens of seconds. Furthermore, the areas affected by these dose-rate increases are quite local, typically several hundred meters across. It would appear that the phenomena observed during winter thunderstorms are caused by the acceleration and generation of energetic electrons in a strong electric field formed before lightning discharges as a static process, and are independent of individual lightning flashes. By using the electron and photon transport Monte Carlo calculation code EGS4 [2], we simulated the behaviors of electrons and photons originating from cosmic rays and radon progeny products within the electric field of a typical winter thunderstorm [3, 4]. According to the results of our simulation, the production of secondary electrons and photons increases with electric field intensity, and when the electric field strength exceeds $E_c \approx 280\, P(z)$ kV/m, where $P(z)$ is the atmospheric pressure in units of atm at altitude z, then continuous production occurs and causes an electromagnetic shower. Furthermore, in the transport calculation of the electromagnetic component of cosmic-rays emitted downward from the top of the winter thundercloud, we have clarified that the electron and photon fluxes increased greatly in the high electric field region and the photon energy spectrum showed a large increase in the energy region up to several MeV [3]. However, the behavior of cosmic-ray muons as a source of energetic electrons was not considered in that calculation.

Muons are the most common form of charged cosmic radiation in the lower atmosphere [e.g., see [5]], and many of the energetic electrons in this region are knock-on electrons originated by collision with the muons and air molecules. In addition, as muons finally decay into an electron

and two neutrinos, they can serve as a source of energetic electrons in high electric field regions of thunderclouds. Focusing on muons as a major component of cosmic rays, we investigated the fluctuations experienced by particle fluxes within a thundercloud electric field by simulating the behaviors of cosmic-rays by the Monte Carlo transport calculation.

2 Calculation and Results

2.1 Transport of cosmic-rays in the atmosphere

As various charged energetic particles that exists popularly in the atmosphere, we analyzed the behaviors of cosmic-rays, which form the largest part of energetic particles in the upper atmoshere, using the GEANT4 code [6]. Here, we assumed the cylindrical triple-pole structure given in Fig. 1 when we simulated the distribution of electric charges in a typical winter thundercloud, and determined the distribution of electric field intensities over different altitudes using the finite element method.

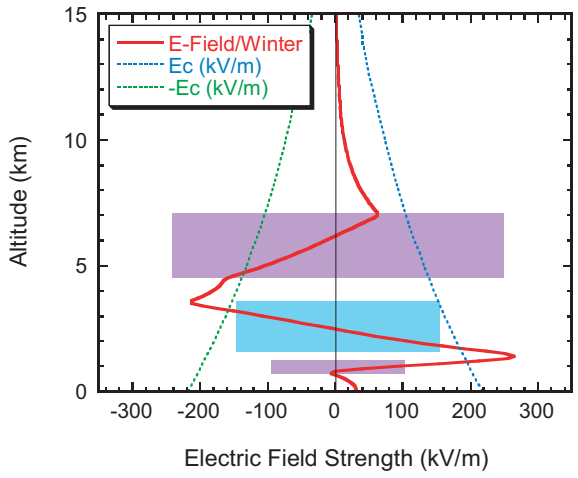

Figure 1: Tri-pole structure model of electric charges in a winter thundercloud and the altitudinal distribution of electric field strength. $|E_c|$ means the threshold field strength generating an electromagnetic shower.

At this time, we segmented altitude into units of 500 m for distances of up to 10 km above ground, and into units of 1 km for distances of 10 to 200 km above ground, so as to assign different atmospheric densities according to the US Standard Atmosphere. The energy spectra of primary cosmic-rays (protons) were determined using the evaluated values based on the LISA simulation [7]. In order to determine the position, the direction, and the energy of electrons produced by various reaction in the atmosphere, we emitted protons downward from an altitude of 100 km. Produced electrons in the atmosphere at the altitude from 0 (on the ground) to 15 km are converted into a input file to the EGS5 code [8, 9] incorporated the effect of external electric fields.

2.2 Incorporating the effect of external electric field to EGS5

In a high electric field, energetic electrons are accelerated to generate copious secondary electrons through collisions with air molecules. Consequently, these phenomena produce a shower of electrons and photons. In order to analyze the transport of energetic electrons by such electric fields and estimate the condition for the generation of the runaway electrons, we modified the sub-routine ELECTR of the EGS5 code, based on the Bielajew's manner [10, 11] for evaluating the influence

that the external electric field has on electrons, and calculated the fluctuation of the total flux and energy spectrum of the bremsstrahlung photons generated in winter thunderstorm electric fields. We have tested the transport of electron and positron in a vacuum in a constant electric field. Trajectories with a electric fields strength of 511 kV/cm are shown in Fig. 2.

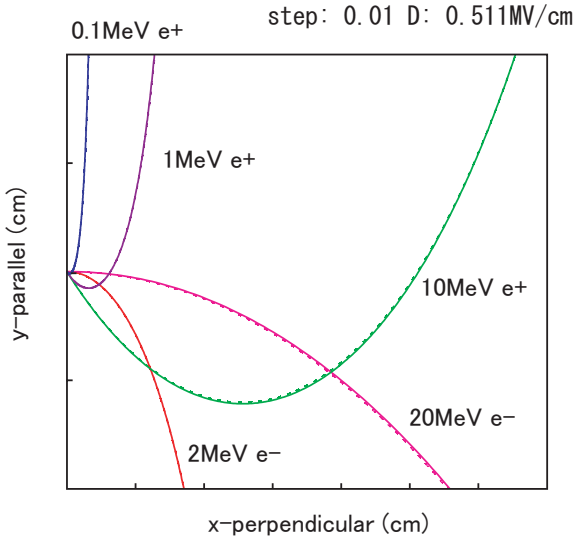

Figure 2: Electron/positron trajectories (solid lines) influenced by a constant electric field in vacuum calculated using the EGS5 code compared with an exact analytical solution (dotted lines).

2.3 Electron and photon fluxes in the thundercloud electric field

We calculated the electron and photon fluxes at various altitudes assuming that the primary cosmic rays (proton) are emitted downward at the altitude 100 km. Since it is considered that the thunderclouds form a tripole charge structure even in winter, we modeled the vertical electric fields inside and below the tripole winter thundercloud by using Finite Element Method, and adopted the models (depicted in Figure 1) in the Monte Carlo calculation.

As illustrated in Fig. 3, the electron and photon fluxes in the tripole winter thundercloud model increases sharply around the altitude 1km, the lower part of the cloud, and remains several times greater than the other two results even below the cloud base. It is presumably due to the strong electric field of the tripole model exceeding E_c around this altitude. Such an electric field can lead to the avalanche-type increase of energetic runaway electrons and thus the generation of a significant amount of bremsstrahlung photons, some of which may reach the ground consequently causing the dose-rate increases we observed in conjunction with the winter thunderstorm activities.

From the simulation results described above, we can draw the following conclusions. In the tripole winter thundercloud, it is possible that runaway electrons and intensive radiation are generated in the lower part of the cloud where a strong electric field exceeding E_c exists (see Fig. 1), and then trigger the dose-rate increases such as those we observed on the ground. However, in the case of the summer thunderclouds, the altitude of the strong electric field region is thought to be considerably greater than the attenuation length of bremsstrahlung photons. So it seems that such thunderclouds rarely affect the dose-rate on the ground except in the mountain areas, because the radiation produced inside the strong electric field region is expected to attenuate in the atmosphere, as described in the previous paper [3], so that near the ground it is hardly discernible above background levels.

2.4 Enhanced electron and photon fluxes and lightning initiation

This section discusses the fluctuations experienced by electron fluxes in the presence of a thundercloud electric field.

When the cosmic-rays are discharged in the atmosphere, the presence of a strong electric field causes a dramatic growth of electron flux, which is more significant than the increase of photon fluxes. While the electric field strength necessary for producing breakdown of air has been determined to be about 3 MV/m in laboratory experiments (using parallel plate electrodes), an electric field with such strength has never been observed in a thundercloud; the typical electric field strength in a thundercloud is an order of magnitude less than the threshold field strength of conventional air breakdown. This means that the mechanism behind the initiation of lightning discharge remains unclear. Gurevich et al. [12] have characterized the difference from the conventional breakdown by the presence of runaway electrons; such runaway electrons are produced by the acceleration of cosmic-ray electrons in the atmosphere and can produce a particular type of breakdown called runaway air breakdown. Our analysis has confirmed the possible occurrence of an electromagnetic shower at electric field strengths almost an order of magnitude lower than the conventional breakdown requirement, which could increase the electron flux by more than two orders of magnitude, and increase the number of electrons with energy of several MeV in particular.

These results suggest as follows:

- In the region with a strong electric field in thunderclouds, cosmic rays can trigger the production of a large number of energetic electrons.
- Since the W-value of air is about 34 eV per electron-ion pair, energetic electrons can produce a large number of electron-ion pairs as they are absorbed in the air.
- The production of a large number of electron-ion pairs should increase the electric conductivity in the region with a strong electric field, which may boost the initiation of a lightning discharge.

3 Concluding Remarks

In order to clarify the reason for the gamma-ray dose increases observed on the ground during winter thunderstorms, we have calculated the electron and photon fluxes by using the Monte Carlo calculation codes with the function of evaluating the effect of an external electric field. As a result, it is possible that runaway electrons and bremsstrahlung photons are generated in the lower part of the cloud where a strong electric field exceeding E_c exists, and then trigger the dose-rate increases such as those we have observed on the ground during winter thunderstorms. Furthermore, we have obtained an enormous increase flux of electrons within a thundercloud electric field. This suggests the possibility of lightning initiation through the runaway air breakdown by an injection of energetic radiation. In particular, since high energy muons form a large part of the secondary cosmic-rays, and directly reach the region of strong electric fields owing to their high penetrability in the atmosphere, they can serve as the source of a considerable amount of runaway electrons, through their ionization of air molecules producing a number of knock-on electrons and the production of muon decay electrons. If it is possible that the injection of the high energy muons to the thundercloud electric field causes the lightning discharge, the following idea comes out: a muon triggered lightning. When a beam of high energy muons, which have been made by a particle accelerator, is irradiated toward a thundercloud, the muons can easily reach a region with high electric field, and hence the muons directly promote ionization of the air in the thundercloud through the production of knock-on electrons and the subsequent generation of the electromagnetic shower [13].

References

[1] T. Torii, M. Takeishi, T. Hosono, J. Geophys. Res. **107 (D17)**, 4324 (2002).

[2] W. R. Nelson, H. Hirayama, D. W. O. Rogers, *"EGS4 Code System"* SLAC-265 (1985).

[3] T. Torii, T. Nishijima, Z-I. Kawasaki, T. Sugita, Geophys. Res. Lett. **31**, L05113 (2004).

[4] T. Torii, T. Nozaki, T. Sugita et al., International Congress Series. 1276, Elsevier, doi:10.1016/j.ics.2004.11.110 (2005).

[5] NCRP, NCRP Report No. 94, National Council on Radiation Protection and Measurement, Bethesda, MD, USA ((1987).

[6] S. Agostinelli, J. Allison, K. Amako, et al., Nucl. Instrum. Meth. A, **506 (3)**, 250 (2003).

[7] Simulation of Test-Mass Charging in the LISA Mission: WP500 Software User's Manual, WP500-SUM-ICL-002, Inperial College London (2004).

[8] S. J. Wilderman and A. F. Bielajew, *"Proceedings of the 3rd International Workshop on EGS,"* KEK Proceedings 2005-3, 1 – 18 (2005).

[9] Y. Namito and H. Hirayama, *"Proceedings of the 3rd International Workshop on EGS,"* KEK Proceedings 2005-3, 19 – 26 (2005).

[10] A. F. Bielajew, in *Monte Carlo Transport of Electrons and Photons*, pp. 421 – 434, Prenum, NY, USA (1987)

[11] T. Torii, M. Takeishi, T. Hosono, T. Sugita, *"Proceedings of the 2nd International Workshop on EGS,"* KEK Proceedings 2000-20, 324 – 329 (2000).

[12] A. V. Gurevich G. M. Milikh, R. Roussel-Dupré, Phys. Lett. A, **165**, 463 (1992).

[13] T. Torii, T. Sugita, et al., Monte Carlo 2005 Topical Meeting, Chattanooga, TN, USA (2005) [see $http://rsicc.ornl.gov/rsiccnew/MC2005_Presentations/Program1.htm$].

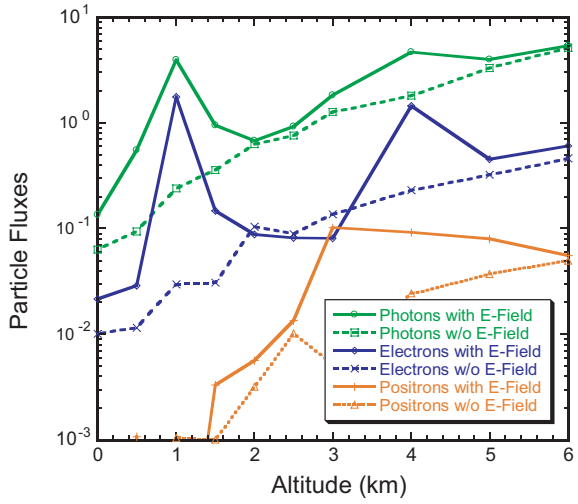

Figure 3: Particle fluxes with the tripole winter thundercloud electric field and without any electric fields calculated by the GEANT4/EGS5 code.

SPECIFIC ABSORBED FRACTIONS FOR PHOTON AND ELECTRON TO A SIMPLE STOMACH MODEL CONSIDERING STEM CELLS

S. Kinase, R. Watanabe and K. Saito

Research Group for Radiation Effect Analysis,
Nuclear Energy Basic Engineering Research Sector,
Japan Atomic Energy Agency, Tokai-mura, Naka-gun, Ibaraki 319-1195, Japan
e-mail: kinase.sakae@jaea.go.jp

Abstract

The aim of the present work is the development of logical dosimetry for human alimentary tract. In this work, specific absorbed fractions for both photon and electron to a stomach model with stem cells have been evaluated in the energy range 10 keV-4MeV using Monte Calro simulation. Furthermore, S values to the stomach model have been evaluated for several positron sources: ^{11}C, ^{13}N, ^{15}O and ^{18}F. Consequently, it was found that photon SAFs to stem cells in the stomach are greater than those to the whole stomach wall. Electron SAFs to stem cells in the stomach were also found to be less than those used in the radiological protection. The stomach wall S values are less than those used in the radiological protection. It is concluded that the determination of target tissue in the stomach is very important for the SAF and S value evaluations.

1. Introduction

Specific absorbed fraction (SAF) –the fraction of energy emitted as a specified radiation type in a source tissue which is absorbed in 1 kg of a target tissue– is very important from the standpoint of developing logical dosimetry for human alimentary tract [1-4]. In evaluating SAFs for the alimentary tract, target tissues should be considered to be the radiosensitive epithelial stem cells in the regions such as the stomach. Both the Medical Internal Radiation Dose (MIRD) committee [1] and the International Commission on Radiological Protection (ICRP) [2,3] have provided the estimates of SAFs for photon and electron sources uniformly distributed in the stomach contents of a MIRD 5 type phantom. The photon SAFs to the stomach wall were estimated using the mean absorbed dose to the whole stomach wall, whereas the electron SAF to the stomach wall was taken to be a constant as a measure of the SAF to the stem cells in the stomach wall. The electron SAF was estimated by use of the simple assumption that the absorbed dose to the cells was calculated as 50% of the average absorbed dose to the stomach contents. Consequently, the target tissue in the stomach wall was not considered to be the stem cells in the radiation dosimetry for human alimentary tract. Since the absorbed dose evaluation method for the stomach wall is not logical, the dose to the stomach wall might not reflect the radiation risks.

Two groups [5-8], using the stomach model that is divided into multi-layers, have evaluated SAFs for photon and electron to stem cells in the stomach. However, there are few data on photon and electron SAFs to stem cell layer whose thick is of the order of 10 μm in their reported results. To develop the logical dosimetry for human alimentary tract, SAFs to the stem cells are required. The present study evaluates photon and electron SAFs to stem cells in the stomach wall that is a region of human alimentary tract. In addition, this study describes S values –mean absorbed dose to a target tissue per unit cumulated activity in the source tissue– to the stem cells for four positron emitters: ^{11}C, ^{13}N, ^{15}O and ^{18}F.

2. Materials and Methods

2.1 Stomach model

The stomach was modeled as ellipsoids in **Fig.1** shows. The stomach wall was divided into multi-layers which range in thickness from 10-μm layers within the inner 300 μm to 130-μm layers within the outer 5830 μm of the wall. The stem cells were taken to be a continuous layer at a depth of 60 μm to 100 μm from the inner surface of the stomach in a similar manner of ICRP [4]. The stomach model was assumed to have the component of ICRP stomach [9] (**Table 1**) and to be located in semi-infinite soft tissue. The masses of the stomach wall and the stomach contents were 0.15 kg and 0.247 kg, respectively.

2.2 SAF evaluation

Stomach SAFs were evaluated for both monoenergetic photons and electrons with energies ranging from 10 keV to 4 MeV using the Monte Carlo code, EGS4 [10]. The SAFs were evaluated as the fraction absorbed in the target tissue of the energy released in the stomach contents –AF– divided by the mass of the target tissue. The sources of the photons and electrons were assumed to be uniformly distributed in the stomach contents. The target were three tissues: 0-10 μm layer from the inner surface of the stomach –0-10 μm layer, 60-100 μm layer from the inner surface of the stomach –stem cell layer– and the whole stomach wall The number of histories of the simulations were basically determined to reduce statistical uncertainties below 5 %. No variance reduction technique was used. The cross–section for photons were taken from PHOTX [11] and the data for electrons were taken from ICRU report 37 [12]. The photon SAFs were evaluated considering energy deposition due to secondary electrons.

2.3 S value evaluation

S values to three target tissues in the stomach wall from uniformly distributed positron emitters within the stomach contents were evaluated, using the results of the SAFs for both photons (two annihilations) and electrons. The SAFs were converted into the S values, through consideration of the masses of the target tissues in the stomach and the decay modes of the radionuclides. The nuclides were ^{11}C, ^{13}N, ^{15}O and ^{18}F. **Table 2** shows the maximum and mean energies of the positron emitters. The decay mode for each emitter was assumed to consist of a main branching since a few percentages branching for the decay mode would be insignificant for the S values evaluations. The spectra for the positron emitters were taken from DECDC2 [13].

3. Results and Discussion

Figure 2 shows photon SAFs to 0-10 μm layer, stem cell layer and whole stomach wall. As a whole, the SAFs, shown in the figure, decrease with an increase in the photon energy. The photon SAFs to both 0-10 μm layer and stem cell layer are larger than those used in the radiological protection –whole stomach wall SAFs– in the energy range 10 keV-4MeV. From a comparison of the photon SAFs to the whole stomach wall in ICRP publication [2], a good agreement were found between the evaluated results and those listed by ICRP except for the SAF at the energy 4 MeV. The discrepancy in the SAF at photon energy of 4 MeV is considered to be due to the differences in the photon cross–section and the photon transport.

Electron SAFs to 0-10 μm layer, stem cell layer and whole stomach wall are shown in **Fig.3**. The SAFs increase as energy increases in the range 10 keV-4MeV. These results demonstrate that electron SAF to the stomach wall is not a constant used in the radiological protection. The electron SAFs to stem cells in the stomach are less than those used in the radiological protection. The electron SAF to stem cell layer shows a sharp rise at 100 keV since the SAFs at energies greater than 60 keV are directly contributed from the primary electrons –the csda range at the energy of 60 keV in the stomach is approximately 59 μm.

In **Fig. 4**, S values for ^{11}C, ^{13}N, ^{15}O and ^{18}F, respectively, are shown for the target tissues in the stomach; the contributions from positrons and the two annihilation photons are presented separately. The S values increase with an increase in mean energy of beta ray. For nuclides with the large positron energies, positron interactions are large contributor to the S values. The stomach wall S values are less than those used in the radiological protection.

4. Conclusions

We have evaluated SAFs for both photon and electron to a simple stomach with stem cells using EGS4 code. Furthermore, stomach S values for positron emitters were evaluated using the results of the SAFs . Both the SAFs and S values to the stem cells in the stomach were found to disagree with those used in the radiological protection. Consequently, the preliminary conclusion was reached that the determination of target tissue, in particular of stem cells in the stomach is very important for the evaluation of SAFs and S values. We plan in the near future to develop a precision stem cell model of the human alimentary tract for logical dosimetry.

References

1) W. S. Snyder, H. L. Fisher, Jr., M. R. Ford and G. G. Warner; Estimates of absorbed fractions for monoenergetic photon sources uniformly distributed in various organs of a heterogeneous phantom, MIRD Pamphlet No.5, J. Nuclear Med. 10 Suppl. 3, 5-52 (1969).
2) ICRP: Report of the task group on reference man, ICRP Publication 23, Pergamon Press, Oxford, UK (1975).
3) ICRP: Limits for intakes of radionuclides by workers, ICRP Publication 30, Pergamon Press, Oxford, UK (1979).
4) ICRP: Human alimentary tract model for radiological protection, a draft document (2004).
5) J. W. Poston, Jr., K. A. Kodimer, W. E. Bolch and J. W. Poston, Sr.; Calculation of absorbed energy in the gastrointestinal tract, Health Phys. 71, 300-306 (1996).
6) J. W. Poston, Jr., K. A. Kodimer, W. E. Bolch and J. W. Poston, Sr.; A revised model for the calculation of absorbed energy in the gastrointestinal tract, Health Phys. 71, 307-314 (1996).
7) N. U. Bhuiyan and J. W. Poston, Sr.; A revised model for electron dosimetry in the human small intestine, Health Phys. 88, 23-36 (2005).
8) J. B. Stubbs, J. F. Evans and M. G. Stabin; Radiation absorbed doses to the walls of hollow organs, J. Nucl. Med. 39, 1989-1995 (1998).
9) ICRP: Basic anatomical and physiological data for use in radiological protection: reference values, ICRP Publication 89, Pergamon Press, Oxford, UK (2002).
10) W. R. Nelson, H. Hirayama and D. W. O. Rogers: The EGS4 Code System, SLAC-265 (1985).
11) RSIC: DLC-136/PHOTX Photon interaction cross section library (contributed by National Institute of Standards and Technology) (1989).
12) ICRU: Stopping powers for electrons and positrons, ICRU Report 37, Bethesda, Md. (1984).
13) A. Endo, Y. Yamaguchi and K. Eckerman: Nuclear Decay Data for Dosimetry Calculation Revised data of ICRP Publication 38, JAERI 1347 (2005).

Table1 Elemental composition of stomach model[9)]

Organ	Elemental composition (% by mass)								
	H	C	N	O	Na	P	S	Cl	K
Stomach	10.6	11.5	2.2	75.1	0.1	0.1	0.1	0.2	0.1

Table2 Mean and maximum energies of positron emitters[13)]

Nuclides	Mean energy (MeV)	Maximum energy (MeV)
^{11}C	0.386	0.960
^{13}N	0.492	1.199
^{15}O	0.735	1.732
^{18}F	0.250	0.634

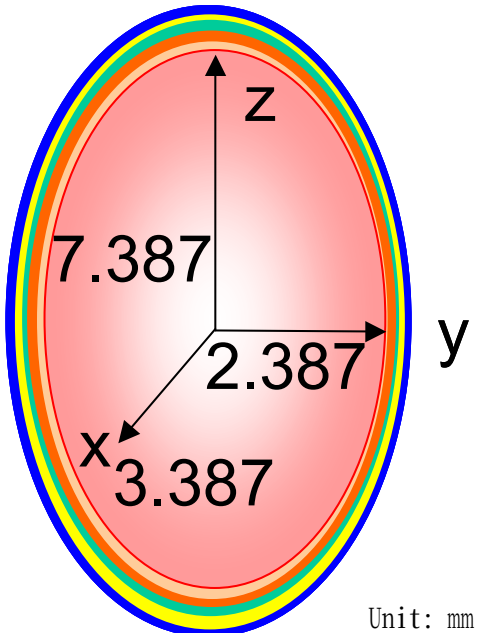

Figure 1. Simple stomach model with stem cells.

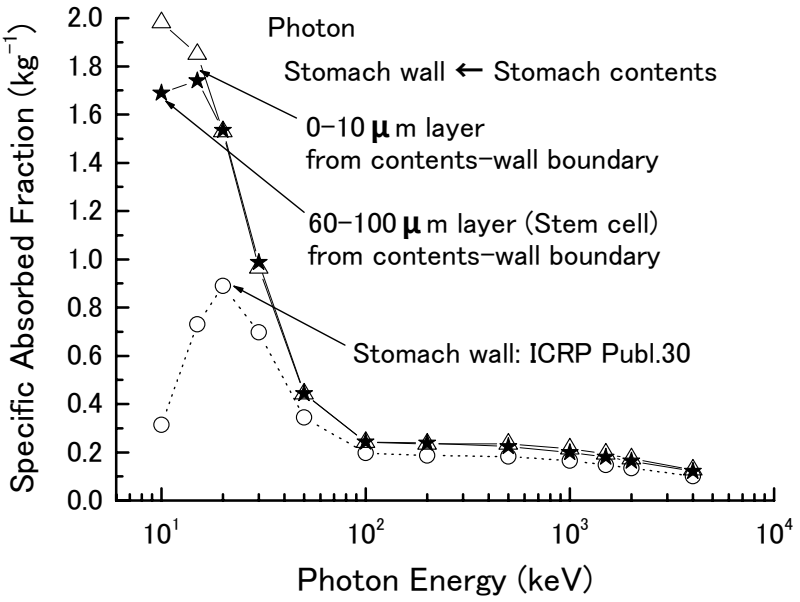

Figure 2. Specific absorbed fractions of energy for monoenergetic photon sources with stomach contents as the source organ and the stomach wall as the target organ.

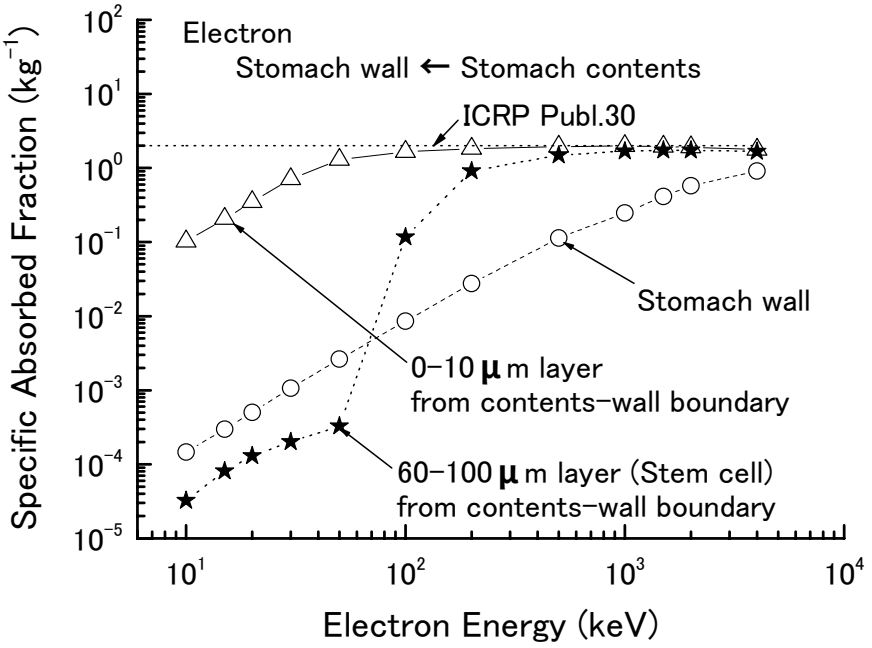

Figure 3. Specific absorbed fractions of energy for monoenergetic electron sources with stomach contents as the source organ and the stomach wall as the target organ.

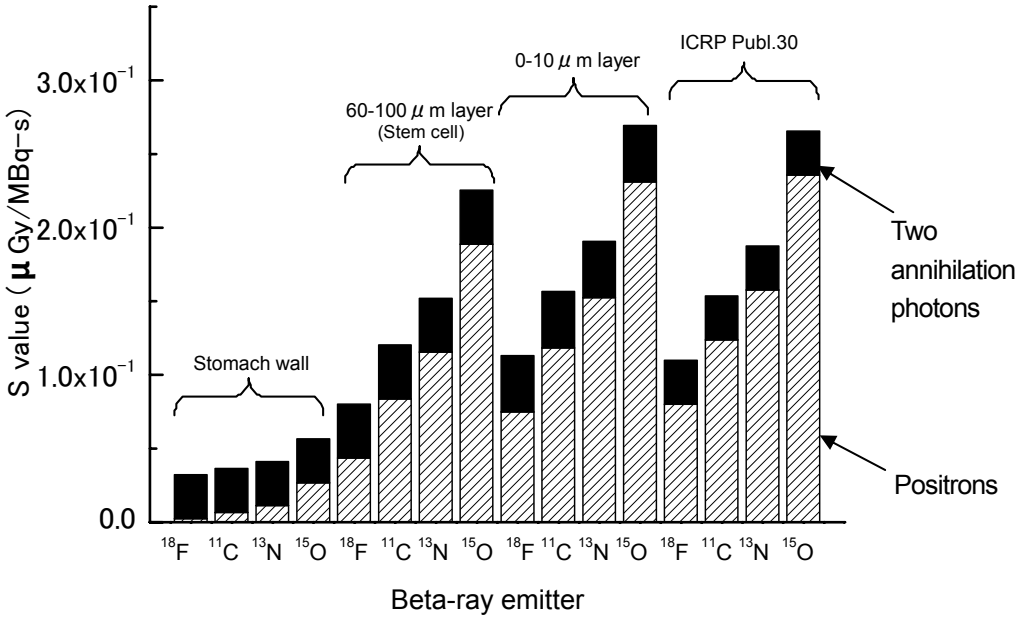

Figure 4. S values for positron emitters distributed in the stomach contents.
Contributions from positrons and from two annihilation photons are illustrated for each S value.

Evaluation of external radiation dose of humans involved in veterinary nuclear medicine by using EGS4

M. Fujii[1], N. Yamada[1], N. Komatsubara[1], N. Ito[1], M. Natsuhori[1], T. Sano[1], H. Hirayama[2], Y. Namito[2]

[1]School of Veterinary Medicine, Kitasato University, Higashi,23-35-1,Towada, Aomori,034-8628,Japan
[2]High Energy Accelerator Research Organization, Tsukuba, Ibaraki,305-0801,Japan

Abstract

This study was undertaken to show the radiation safety data as the reference source of guidelines for the veterinary nuclear medicine in Japan. An EGS4 code was applied in this simulation in order to avoid unnecessary animal experiments. In this study, ^{99m}Tc and ^{18}F were applied since these two nuclides are the most expected radionuclides worth not only for human medicine but also for veterinary medicine. Mathematical phantoms of the canine trunk structures containing the major organs including the heart, the liver, the kidney, and the urinary bladder were prepared and evaluated based on the basis of the mass balance distribution of the radionuclide. Radiation exposure of the personnel involved in veterinary nuclear medicine (a veterinarian, an animal owner, and general public) from the animal and their realistic but maximal condition concerning the time and the distance from the animal for the exposure were also taken into account. The exposure of the veterinarian who uses ^{99m}Tc was estimated at most 0.07mSv per study, which was about 1/300 of the average dose limit per year (20mSv). On the other hand, in case of ^{18}F, the exposure was at most 0.12mSv per study, i.e., about 1/160 of the average dose limit per year. As to the public exposure, less than 1/100 of the counseled level ICRP (1mSv) was achieved by 5 hours after injection of ^{99m}Tc and by 19 hours after injection of ^{18}F to the animal phantom. As to animal owner, less than the dose constraint IAEA (5mSv) was achieved by 12 hours after injection of ^{99m}Tc and 2 hours after injection of ^{18}F, less than the dose constraint of IAEA for children (1mSv) was achieved by about a day after injection of ^{99m}Tc and 6 hours after infection of ^{18}F. In this study, nevertheless the condition for the exposure evaluation is still tough enough for overestimation. Therefore in more realistic or practical condition for the practice of veterinary nuclear medicine, there would be no or insignificant effect for the radiation exposure to the public.

1. Introduction

It is under the legal process of performing nuclear medicine examination in a field of Japanese veterinary medicine. Moreover, it is required to publish radiation safety guidelines about performing veterinary nuclear medicine including the condition that animal is released from the controlled area. Therefore the authors estimated the external radiation exposure of a man from the animal that is administered radiopharmaceuticals. It may be simpler and the better to do animal experiments. However, it makes rather difficult since the Japanese law, at this moment, requires sacrificing the animal after all without coming back from the controlled area. Although there is an exception in the case of positron nuclides with some special cases, in its reality, it is still difficult to perform animal experiments in Japan.

Therefore, we made mathematical phantom of the canine trunk structures and estimated external radiation dose of the people who are related to veterinary nuclear medicine (veterinarian, animal owner, and general public). In this study, ^{99m}Tc and ^{18}F were taken into account to estimate the external radiation exposure.

2. Materials and Methods

2.1 Evaluation of external radiation dose of personnel from animal

By using CGView (Fig.1), two different size (B.W. : 1kg, 30kg) of mathematical phantom models of the canine trunk structures were prepared. Position and weight of each internal organ were decided after the documents of canine anatomy [1-3] and canine x-ray images. Elemental composition and density of each internal organ were based on the documents about human [4]. The dosage of the radiopharmaceutical to the dog phantom was followed by the value used at Tennessee University, college of veterinary medicine [5] as listed in Table 1. It was assumed that the radiopharmaceutical will distribute proportional to the weight of each major organ (heart, liver, kidney, and bladder). Since it was pre-estimated that the ventral side of the liver has the highest dose rate, the detectors were set at the mid- ventral portion of the liver at 0, 10, and 100 cm from the surface of the body (Fig.2). The effective dose was calculated by the following 2 hypothesis. 1) The detector was composed by air, and the energy and the fluence of γ-ray will pass through that area. The effective dose of the detector was calculated by a conversion coefficient. 2) The detector was composed by water, and absorbed dose of γ-ray at this point was calculated and its effective dose was calculated by another conversion coefficient.

The external exposure of the veterinarian was calculated according to the following distances from the animal, i.e., distances at 10 cm from the surface in the first 10 minutes in order to prepare radiopharmaceutical formulation and administration, at 100 cm in the next 40 minutes post dosage for scintigraphy, and 10 cm in the last 10 minutes for the post imaging care. External radiation doses of the animal owner and the general public from the time the dog is released were calculated based on the assumption that an owner will hold the animal (0 cm) and general public at 100 cm.

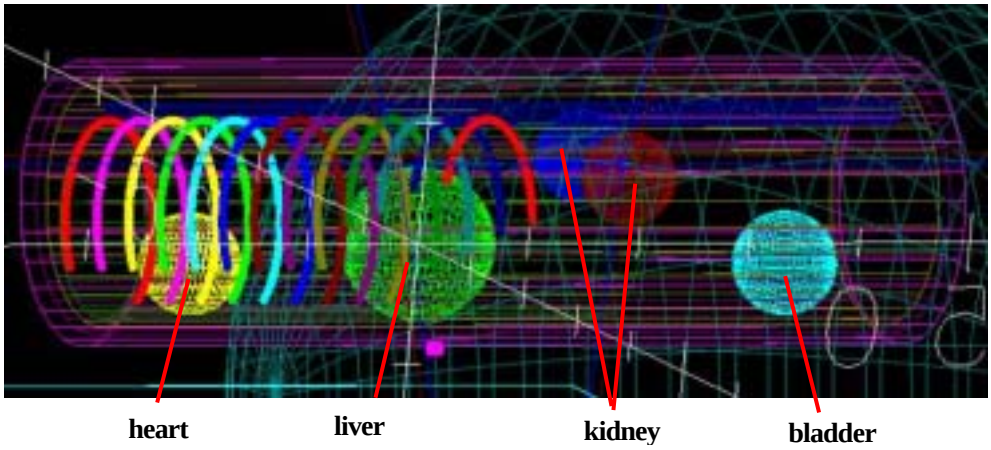

Fig 1. Canine trunk mathematical phantom with some particular organs
(Small size : 1kg , Large size : 30kg)

Table 1. Amount of activity of radiopharmaceutical used.

Radionuclide	Weight	Used activity
F-18	B.W. 1kg B.W. 30kg	37MBq 185MBq
Tc-99m	B.W. 1kg B.W. 30kg	185MBq 740MBq

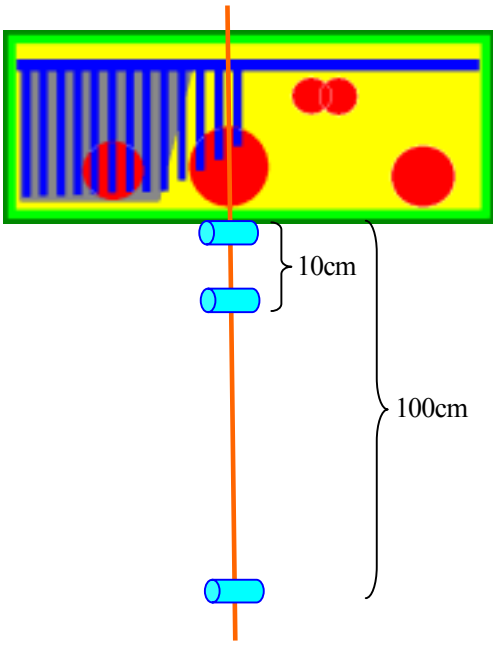

Fig 2. Locations of the detectors from the phantom surface
Each detector (blue) was set at the mid-ventral portion of the liver of 0, 10, and 100 cm from the surface of the phantom.

2.2 Evaluation of the effect by wearing the protecting lead apron

In order to evaluate the effect of protecting lead apron, the external radiation dose to the veterinarian was calculated under condition that Pb sheet (60×60cm, width : 0.25 or 0.50 mmPb) was set at between 0-10cm from the body surface of canine (Fig.3).

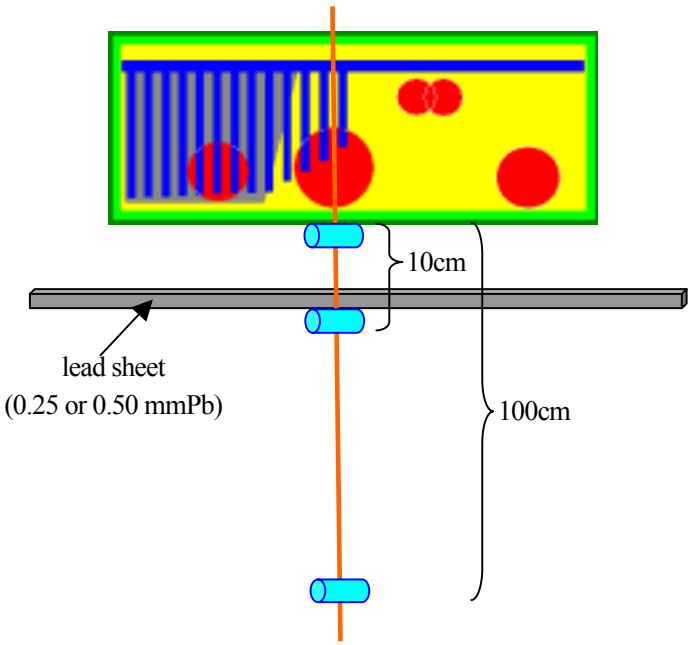

Fig 3. Location of a lead sheet and detectors
A lead sheet is set between 0-10cm and the detectors are assigned as indicated

3. Results and Discussion

3.1 Evaluation of external radiation dose of humans involved in veterinary nuclear medicine

3.1.1 External radiation dose to a veterinarian

The external radiation doses to a veterinarian were at most 65.5 μSv by ^{99m}Tc and 124 μSv by ^{18}F (Fig.4, 5). These are 1/300 and 1/160 of the average dose limit per year (20mSv), respectively.

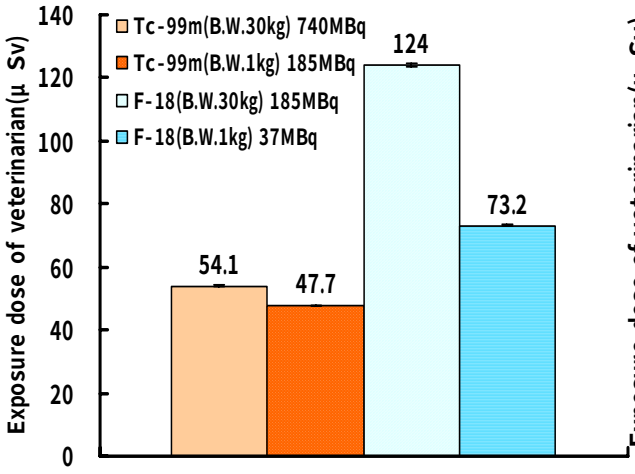

Fig 4. External exposure of a veterinarian, assuming a detector is composed by water

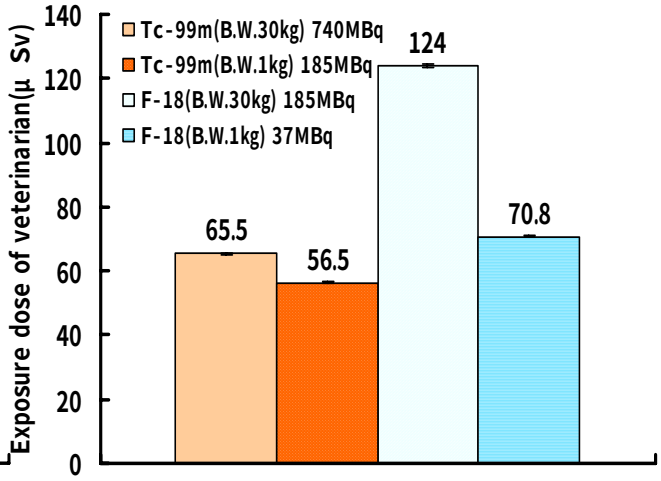

Fig 5. External exposure of a veterinarian, assuming a detector is composed by air

3.1.2 External radiation dose to the general public

The radiation exposure to general public was less than 1/100 of 1mSv (dose limit by ICRP) from a dog, where animal was released 19 hours after ^{99m}Tc administration, and 5 hours after ^{18}F administration (Fig.6).

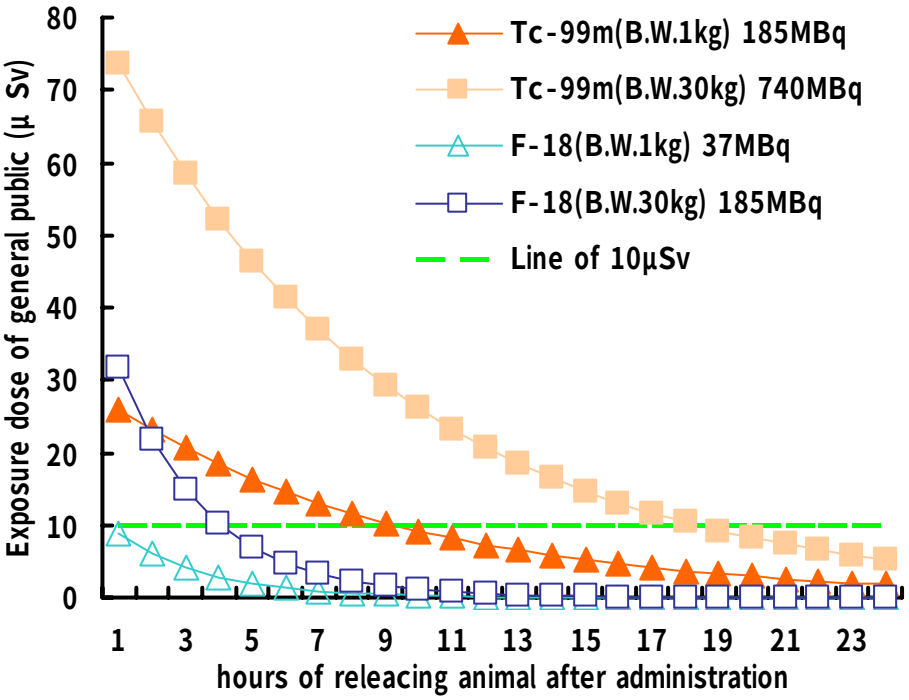

Fig 6. Exposure dose to the general public, assuming each detector is composed by air

3.1.3 The external radiation dose of the animal owner

Fig.7 shows that the external radiation dose to the animal owner from a dog released 12 hours after ^{99m}Tc and 2 hours after ^{18}F administration is below 5mSv. The cumulative dose 5 mSv is the dose constraint by IAEA recommendation for adults. Furthermore, the external radiation dose was less than 1mSv which was dose constraint IAEA recommended for children. This was achieved 1day after ^{99m}Tc and 6 hours after ^{18}F administration.

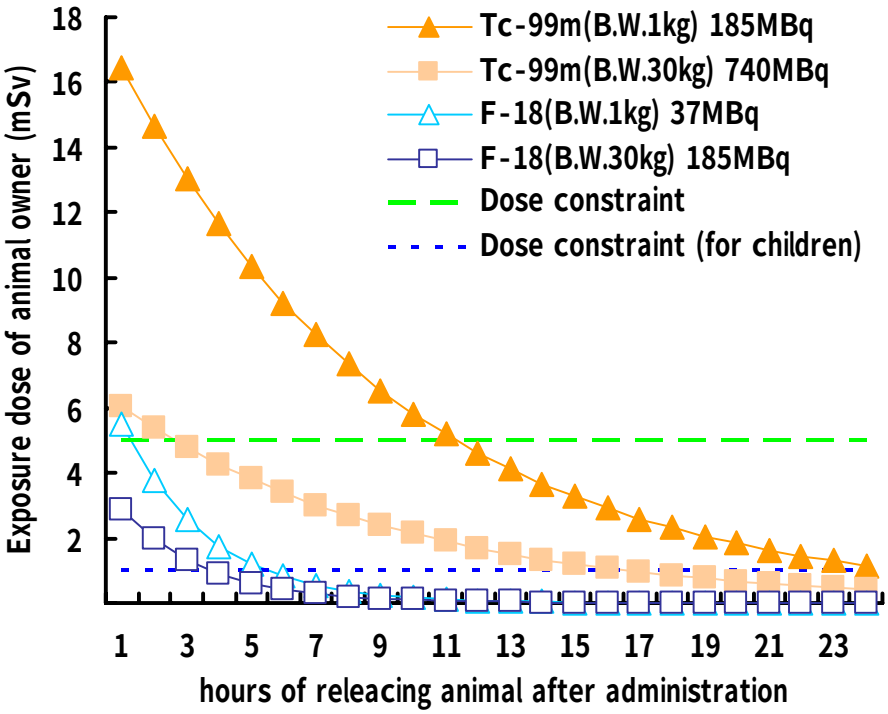

Fig 7. Exposure dose of the animal owner, assuming each detector is composed by air

3.2 Effect of lead apron on external exposure to veterinarians

External radiation dose to the veterinarian decreased by about 45% with 0.25mmPb and about 80% with 0.50 mmPb apron (Fig.8, 9). Therefore, lead apron does work against low energy emitter, ^{99m}Tc in veterinary nuclear medicine. In contrast to ^{99m}Tc, external radiation dose to the veterinarian by ^{18}F was only partly (about 10%) decreased with 0.50 mmPb apron (Fig.10, 11). Therefore, lead apron does not work enough against the annihilation radiation. Consequently, to prevent unnecessary radiation exposure from ^{18}F, short time handling and long distance were the very important rather than shielding by lead apron.

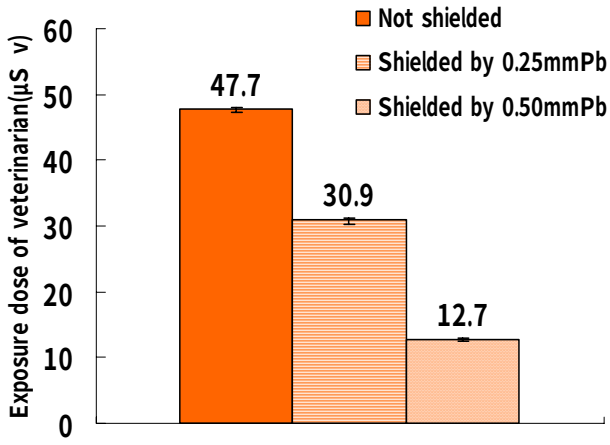

Fig 8. The ^{99m}Tc radiation dose to a veterinarian who wears lead apron (Detectors / water)

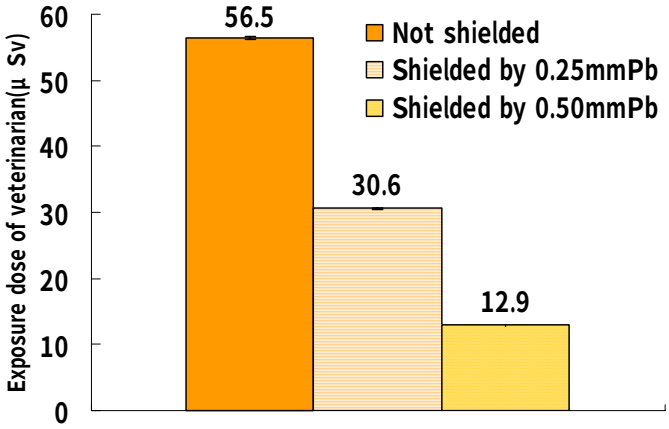

Fig 9. The ^{99m}Tc radiation dose to a veterinarian who wears lead apron (Detectors / air)

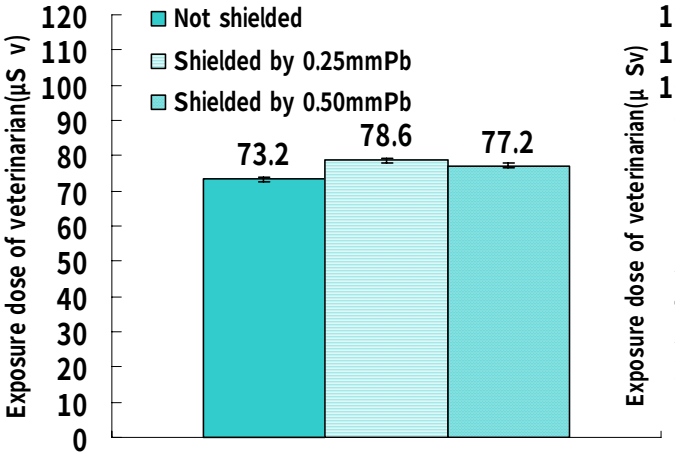

Fig 10. The ^{18}F radiation dose to a veterinarian who wears lead apron (Detectors / water)

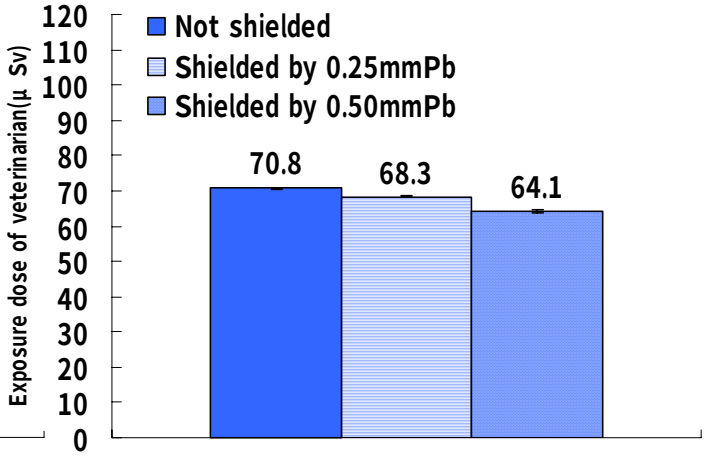

Fig 11. The ^{18}F radiation dose to a veterinarian who wears lead apron (Detectors / air)

4. Conclusions

Significant differences in external radiation exposure between ^{18}F and ^{99m}Tc were demonstrated by using EGS4 code. Most likely these are due to the significant difference in energy of γ ray and physical half life. Therefore understanding these physical property and interaction with animal body through the exposure to the human will become quite significant.

As to exposure, even under our overestimating condition, it was indicated that the exposure to veterinarians could be mimicked with adequate animal handling and usage of radiopharmaceuticals. And the external radiation dose of the animal owner was estimated to be less than 5mSv, which was dose constraint IAEA recommendation for adults, and less than 1mSv was achieved for children under particular releasing criteria. Moreover, even in our rough protocol, less than 1/100 of 1mSv, the dose limit of ICRP, was achieved for general public. Although in this study, all calculation settings were made for the risky side to overestimate the exposure. Therefore, by putting an effort with the better guidelines for decreasing the unnecessary exposure during the procedure for veterinary nuclear medicine, significant reduction in the external radiation to the personnel who are involved in veterinary nuclear medicine will be achieved.

5. Acknowledgement

This work was supported by High Energy Accelerator Research Organization. Numerous advices with Dr. Hirayama (KEK) are gratefully acknowledged.

References

1) G. A. Chibuzo, “The Digestive Apparatus and Abdomen”, in Miller’s Anatomy of the Dog, edited by H. E. Evans, (W.B. Saunders Co., Philadelphia, 1993), pp.396-462.

2) H. E. Evans, G. C. Christensen, “The Urogenital System”, in Miller’s Anatomy of the Dog, edited by H. E. Evans, (W.B. Saunders Co., Philadelphia, 1993), pp.494-558.

3) H. E. Evans, “The Heart and Arteries”, in Miller’s Anatomy of the Dog, edited by H. E. Evans, (W.B. Saunders Co., Philadelphia, 1993), pp.586-681.

4) ICRP Report 89, “Basic Anatomical and Physiological Data for Use in Radiological Protection: Reference Values”, The International Commission on Radiological Protection, Oxford (2001).

5) G. B. Daniel, A. Bahr, “Bone Scintigraphy”, in Nuclear Medicine Short Course, edited by A. Bahr, C. R. Berry, and G. B Daniel, (University of Tennessee, Knoxville, 2002), pp.1-9.

LUNG FIELD DOSE EVALUATION OF DIAGNOSTIC X-RAYS AND HIGH ENERGY RADIATION USING VOXEL BODY PHANTOM

K. Koshida, A. Chadani, and Y. Kikuchi

Division of Health Science, Graduate School of Medical Science, Kanazawa University

Abstract

In a dose simulation, it is not easy to evaluate the accuracy of a human body-like model. Many different types of phantom have been used as human body models. Recently, the voxel phantom has been used as a mathematical phantom. Therefore, the voxel phantom of a human body phantom was used as a model to evaluate the lung field dose distribution. The backscatter factor in the lung field was lower than the values reported previously (Cohen *et al.*, 1961; Bewly *et al.*, 1983). In the lung region, we examined the extent of irradiation of the normal lung tissue outside the tumor region. The usefulness of the Monte Carlo simulation was accepted for both diagnostic X-ray energy and 4MV X-ray energy.

1. Introduction

In recent years, the development of computer technology has facilitated simulation using mathematical rather than non-physical substitute phantoms. The Monte Carlo simulation using the mathematical phantom (voxel phantom) of a human body model allows determination of the details of the dose distribution in the human body. A mathematical phantom[1)] of a human body phantom is usually used as a model, to allow comparison with the measurements. However, it is not easy to evaluate the accuracy of a human body model in dose simulation. Therefore, a mathematical phantom was constructed from the CT data of the human body phantom, which could be used to measure the internal dose or the surface dose. The Monte Carlo simulation using this mathematical phantom was useful to determine the absorbed doses inside and at the surface of the phantom.

2. Materials and Methods

2.1 Materials

A human body phantom was used, which was made of PMMA including natural human bone and lung-like cork. The human body phantom has a number of the holes into which can be inserted TLD elements (hole grid), and is sliced at a thickness of 2 cm. Fig. 1 shows the human body phantom. The voxel phantom was made from CT images of the human body phantom. Fig. 2 shows the CT image (a) divided into 0.5-mm squares and the raw image (b) with pixels corresponding to 1.0 cm^2. CGVIEW Version 1.2 was used for display of the expanded image to 1.0 cm^2. The substance data of tissue substitutes used by EGS referred to ICRU Report 44[2)].

2.2 Diagnostic and 4MV X-ray energy spectra by simulation

The diagnostic X-ray energy spectrum was obtained by measuring the continuous output of the diagnostic unit (UD150-LR2: Shimadzu Inc., Kyoto, Japan). The continuous energy spectra were obtained with loading factors of 70 kV, 90 kV, and 110 kV tube voltages. The total filter thickness of the x-ray tube unit was 3.1 mmAl. Fig. 3 shows the continuous energy spectra.

The 4MV X-ray energy spectrum was calculated using the approximation formula of Schiff[3]. The obtained photon energy spectrum[4] was taken as the spectrum after filtering with a stainless steel flattening filter with an average thickness of 7.7 mm. Fig. 4 shows the sectional view of a linear accelerator showing the process of X-ray generation. Fig. 5 shows the 4MV X-ray energy spectrum determined in the simulation.

2.3 The conditions of EGS simulation and Voxel phantom

The Monte Carlo calculation was performed with Electron Gamma Shower Version 4 (EGS4) and Version 5 (EGS5). The conditions of EGS simulation were PCT<10 keV and ECUT<521 keV. The EGS4 code used was "ucphantom_cgp.mor," while that of EGS5 was "ucxyz_phantom.f." The number of photons was more than Photons of 10^6. The fractional standard deviation by the MORSE-CG method was less than ±10%.

In the diagnostic X-ray simulation, the backscatter factor (BSF) was calculated at the back surface position of voxel phantom, because chest radiography was assumed. In the diagnostic X-ray energy range, the back scatter factor[5), 6)] has been reported until an irradiation field of 18×18 cm^2, but there have been no reports beyond this size. Therefore, the irradiation fields were expanded to 35×35 cm^2, which was close to the width of the voxel phantom. Before examining the voxel phantom, the BSFs were investigated by simulation of the water phantom. The forms of the water phantom were 50 cm×50 cm×20 cm, 45 cm×30 cm×20 cm, and 45 cm×30 cm×20 cm, including the air region (39 cm×24 cm×14 cm).

On the other hand, the tumor of the chest region was targeted in the 4MV energy simulation. It was considered as a size of 2×2×2 cm^3, and was presupposed to be located in the center of the lung field. In this case, the irradiation fields were 2×2 cm^2, 5×5 cm^2, and 10 cm×10 cm^2. The obtained doses were normalized by setting the maximum dose to 100.

3. Results

3.1 Back scatter factor with diagnostic X-ray simulation

To obtain the BSF, we examined the water phantom and the voxel phantom. The water phantom was used for comparison with the values[5)6)] reported.

3.1.1 Back scatter factor by water phantom

Fig. 6 shows the BSF value for the form of the water phantom, 50 cm×50 cm×20 cm. The value of the BSF also increased with increases in the irradiation field. Fig. 7 shows the BSF value for the form of the water phantom, 45 cm×30 cm×20 cm. The value of the BSF also increased with increases in the irradiation field, but it tended to become a constant value from 20 cm or 25 cm. Fig. 8 shows the BSF value for the form of the water phantom, 45 cm×30 cm×20 cm including the air region (39 cm×24 cm×14 cm). Overall, the BSF value is low.

3.1.2 Back scatter factor by voxel phantom

Fig. 9 shows the BSF value for the voxel phantom. The BSF value was lower than that of the form of the water phantom, 45 cm×30 cm×20 cm including the air region (39 cm×24 cm×14 cm), and shows the maximum value nearly 20 cm from the side of the irradiation field.

3.2 Dose distribution for 4MV X-ray energy spectrum

Fig. 10 shows the dose distribution for irradiation simulation with two opposing fields. The irradiation field was 2 cm×2 cm. In the lung region, the irradiation of the lung region by the opposite side and irradiation to the spinal column were avoided as much as possible. Fig. 11 shows the dose distributions in the irradiation fields of 5 cm×5 cm and 10 cm×10 cm. These dose distributions show that the therapeutic dose was irradiated beside the tumor region.

4. Discussion

In the water phantom (50 cm×50 cm×20 cm), the value was almost the same as those reported valus[5)6)]. However, the human abdomen is full of water in the human body. The human body also has a chest and a head. It is difficult to evaluate these values in the same way. Although examination in the RAND phantom is also possible, it is difficult to unite with everybody. In this respect, as Monte Carlo simulation can be used to treat the phantom on a computer, and it is easy to modify. By this Monte Carlo simulation, we found that it was not suitable to fit the reported back scatter factors. It was generally lower than the reported back scatter foactors.

The disagreement between the calculated and actual measurement values in the chest were thought to be due to problems in the X-ray energy spectrum used in the simulation. The Percentage Depth Dose (PDD) of the X-ray spectrum (the approximation formula of Schiff) showed a difference of about 13% as compared to the measurement value. This was because a flattening filter of the special cone form used in the process of X-ray generation was calculated for an average thickness of 7.7 mm. In the lung region, irradiation of the lung region by two opposing fields and irradiation of the spinal column are avoided as much as possible. It is known that the therapeutic dose irradiates tissue adjacent to the tumor region. The Monte Carlo simulation is effective to determine the extent of this irradiation.

5. Conclusions

As a mathematical phantom, the voxel phantom has come to be used in recent years, and evaluation was performed. It is easy to evaluate the mathematical phantom for Monte Carlo simulations by the human body phantom. Its usefulness was accepted for both diagnostic X-ray energy and 4MV X-ray energy. In the lung field, it became lower than the values reported previously. In the lung region, the extent of irradiation of the normal lung tissue adjacent to the tumor region could be examined. Thus, the Monte Carlo simulation using this mathematical phantom was useful to determine the absorbed doses inside and at the surface of the phantom.

References

1. ICRU: Phantoms and Computational Models in Therapy, Diagnasis and Protection, ICRU Report 48 (1992).
2. ICRU: Tissue Substitutes in Radiation Dosimetry to Measurement, ICRU Report 44 (1989).
3. Schiff L.I. : Energy-angle distribution of thin target bremsstrahlung, Phys. Rev., Vol.82(2), 1951.
4. Kato H.: The Monte Carlo simulation with a personal computer, Jpn. J. Radio. Technol. Vol.55(2), 1999.
5. Cohen M. *et al.*: Depth Dose Tables for Use in Radiotherapy, Brit. J. Radiol., Supplement No.10 (1961).
6. Bewley D.K. *et al.*: Central Axis Depth Dose Date for Use in Radiotherapy, Brit. J. Radiol., Supplement No.17 (1983).

Fig. 1 Human body phantom

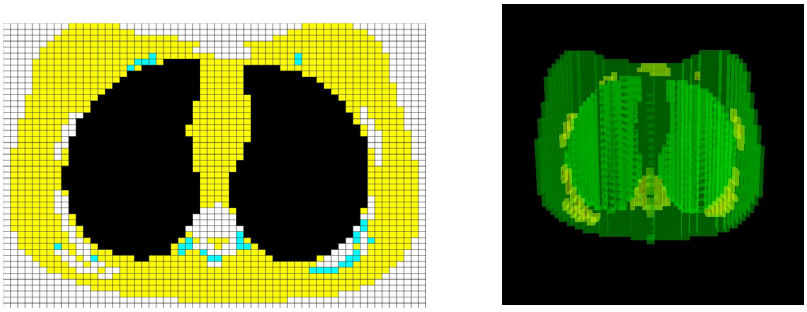

(a) (b)

Fig. 2 CT images: (a) divided into 0.5-mm squares and the raw image
(b) with pixels corresponding to 1.0 cm^2

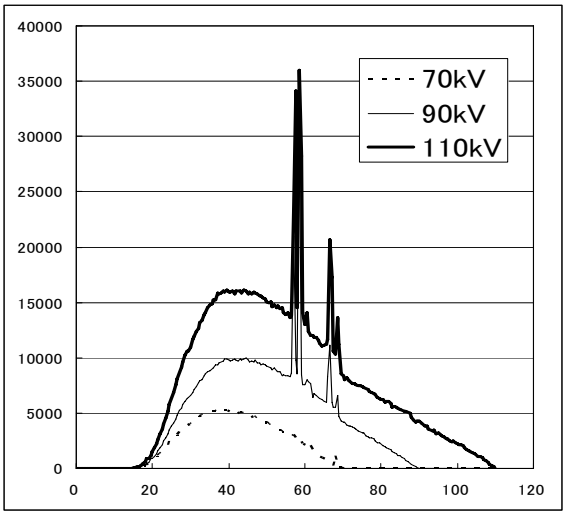

Fig. 3 Continuous energy X-ray spectra

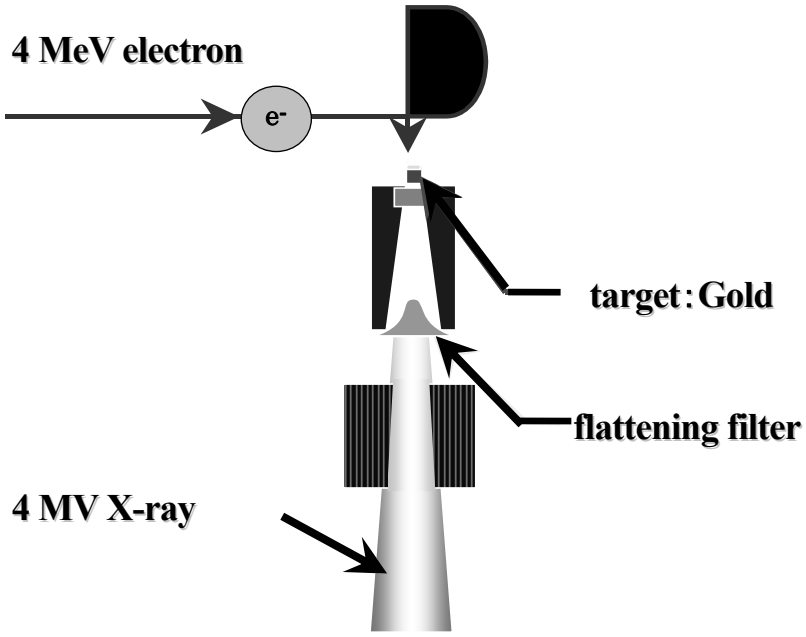

Fig. 4 Sectional view of a linear accelerator showing the process of X-ray generation

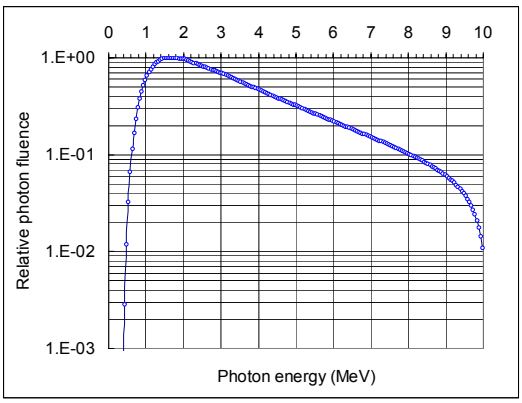

Fig. 5 4MV X-ray energy spectrum determined in the simulation

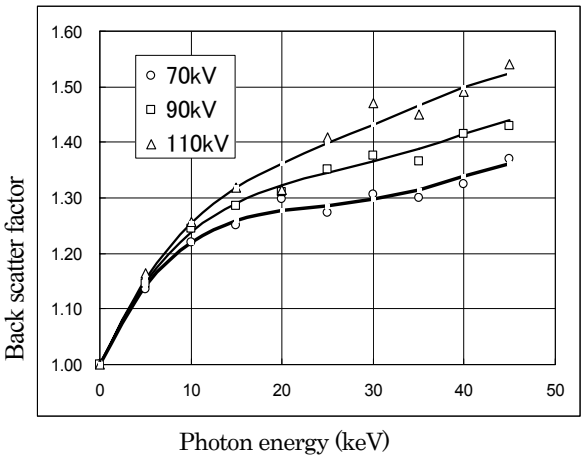

Fig. 6 BSF values for the form of the water phantom, 50cm×50cm×20cm

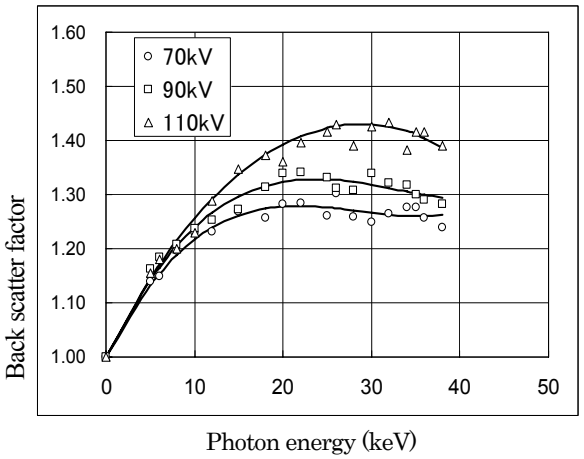

Fig. 7 BSF values for the form of the water phantom, 45cm×30cm×20cm

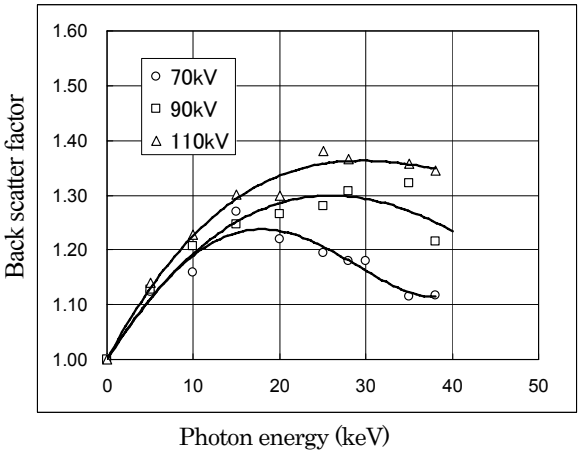

Fig. 8 BSF values for the for of the water phantom, 45cm×30cm×20cm including the air region (39 cm×24 cm×14 cm)

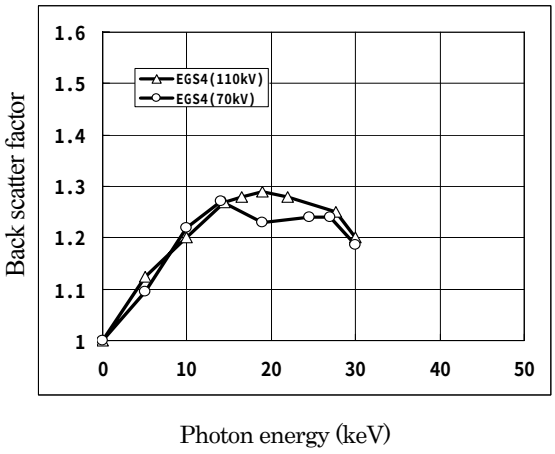

Fig. 9 BSF values for the voxel phantom

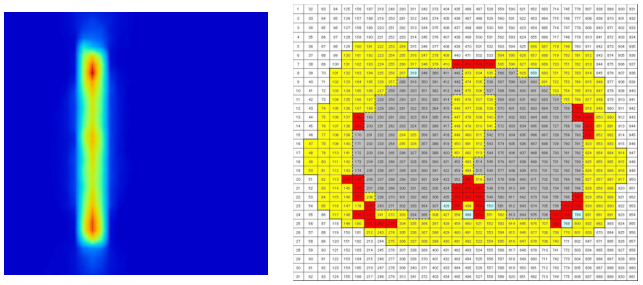

Fig. 10 Dose distribution for irradiation simulation with two opposing fields (irradiation field, 2 cm×2 cm)

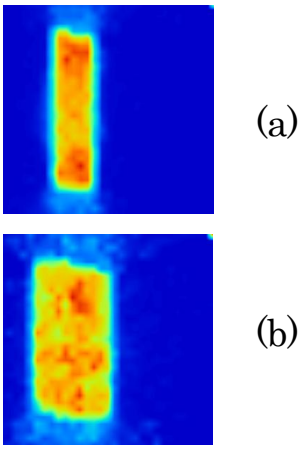

Fig. 11 Dose distributions in the irradiation fields of (a) 5cm×5cm and (b)10 cm×10 cm

EXAMINATION OF THE COMPONENT OF THE SCATTERED RADIATION BY EXTERNAL MONITOR CHAMBER USING THE EGS4

Y. Shiota, K. Tabushi and S. Kito

Department of Radiological Technology, Graduate School of Medicine, Nagoya University
1 - 1 - 20 Daikou – Minami, Higashi area, Nagoya, Japan
e-mail: j050212m@mbox.nagoya-u.ac.jp

Abstract

The output beams of the liner accelerator are radiated by an accelerated electron and a dose rate usually fluctuates. The variation affects the shape of a dose distribution in dosimetry. The external monitor chamber is often used for monitoring the variation. Generally the external monitor chamber is set above the water phantom. Therefore, if the irradiation field is small, the scattered radiation due to the external monitor chamber may affect a measurement dose. This work is to examine the component of the scattered radiation generated by external monitor chamber, and to investigate the effect on measurement dose using the EGS4 code and the Klein-Nishina formula. The shapes and the peak energies were corresponding to the spectra of EGS4 and the Klein-Nishina formula. Therefore the main interaction at the external monitor chamber is Compton scatter. The effect of the scattered radiation and the change of the dose distribution were few. However the dose decreased to about 1% under the position of the external monitor chamber. Therefore we should pay the attention to the distance between the external monitor chamber and the measurement chamber.

1. Introduction

In external radiotherapy, the linear accelerator generates X-rays or electron beams by the accelerated electron. An output dose rate fluctuates by some reasons such as the characteristic of an acceleration. In dosimetry, the variation or the fluctuation affects a measurement dose, as a result the accuracy of dose distributions reduces.

The external monitor chamber is often used, and detects the variation of the output dose. *JSMP* recommends that an ionization chamber should be used as monitor to detect the variation. [1]. The external monitor chamber is generally set above the water phantom, and placed at the corner of the irradiation field to avoid the effect on measurement dose. In case of the large irradiation field, the external monitor chamber is set easily, and the effect is small. However, if the irradiation field is small, the effect due to the scattered radiation becomes large because the horizontal distance between the external monitor chamber and the measurement chamber is small.

The purpose of this work is to examine the component of the scattered radiation generated by external monitor chamber, and to investigate the effect on measurement dose. However it is difficult to measure the scattered radiation, therefore we simulate the scattered radiation by Monte Carlo code EGS4 [2]. In addition, the component of the scattered radiation is estimated using the Klein-Nishina formula [3].

2. Materials and Methods

2.1 EGS4 simulation

A thimble ion chamber was used for the external monitor chamber as shown in figure 1. The external monitor chamber was unequipped a billed up cap because it was not used to measure an air dose. The materials of the wall and the central electrode were polymethylmethacrylate (PMMA) and aluminum (Al), respectively.

The source-surface-distance (SSD) is 100 cm, the water phantom size is30 × 30 × 30 cm^3, and the distance between the external monitor chamber and the phantom surface is 5 cm. The irradiation field size was 3 × 3 cm^2 on the phantom surface, as shown in figure 2 and 3. The external monitor chamber was located at the center of irradiation field to obtain the profile of the scattered radiation originated from the external monitor chamber. The energies of incident photon were 1.17 and 1.33 MeV (60Co γ-rays), and the incident history was 5 × 10^8. The cut-off energies of photon and electron were 10 keV and 521 keV (total energy), respectively, as shown in table 1.

The calculation voxel size was 0.5 × 2.0 × 0.1 cm^3, and its Y-direction was adjusted to the long axis of the external monitor chamber. The data calculated by EGS4 were spectra of the scattered radiation by the external monitor chamber on the water phantom surface, percentage depth dose (PDD) and off center ratio (OCR).

2.2 Calculation of effective energy

The effective energy was calculated to evaluate the reached depth of scattered radiation from the external monitor chamber. The result of EGS4 simulation was applied to the data of the scattered radiation spectrum, and it was chosen as photon spectrum only because the effect of electrons might be small. The following formula (1) was used to the calculation of a attenuation curve.

$$T(x) = \int_0^{E\max} \exp[-\mu(E)\cdot x]\cdot E\cdot F(E)\ \ dE \tag{1}$$

where *T(x)* was a transmission through a filter thickness (*x*), *μ(E)* was linear attenuation coefficient values of the filter materials at the photon energy *E* obtained from *XCOM* [4], and *F(E)* was relative photon spectrum calculated by EGS4. The filter material was Al, and the thickness was 0 to 15 cm. The energy range was 0 to 1.4 MeV, and *dE* was 0.1 MeV. The attenuation curve was obtained by this formula and half-value-layer (HVL) was used to evaluate the effective photon energy.

2.3 Estimation of scattered photon spectrum using Klein-Nishina formula

Klein and Nishina showed the following formula (2) of the differential cross section per unit solid angle with a free electron in a Compton process.

$$\frac{d\sigma}{d\Omega} = \frac{{r_0}^2}{2}\left(1+\cos^2\theta\right)\cdot\left[\frac{1}{1+\alpha(1-\cos\theta)}\right]^2\cdot\left\{1+\frac{\alpha^2(1-\cos\theta)^2}{[1+\alpha(1-\cos\theta)](1+\cos^2\theta)}\right\} \tag{2}$$

where r_0 is called Classical electron radius,

$$r_0 = \frac{ke^2}{m_0c^2} = 2.81794\times10^{-15}[m]$$

$$\left(k = 8.9875\times10^9\left[Nm^2/C^2\right]\ ,\ \ e = 1.6021892\times10^{-19}[C]\right)$$

α is the ratio of the energy of the photon ($h\nu$) to the rest energy of the electron (m_0c^2)

$$\alpha = \frac{h\nu}{m_0c^2}$$

θ is the scattering angle of the photon.

The energy of scattered photon ($h\nu'$) is calculated by the following formula (3).

$$h\nu' = h\nu\frac{1}{1+\alpha(1-\cos\theta)} \tag{3}$$

Each value of the differential cross section and the energy of scattered photon are calculated by the factor of scattering angle θ. The scattering angle θ is converted to the point on the phantom surface using the following formula (4).

$$dist = height \cdot \tan\theta \quad [cm] \tag{4}$$

where *dist* is distance from central axis to the point on a phantom surface. *Height* is the distance between the external monitor chamber and the phantom surface and is 5 cm.

The calculation point is set in the scatter material which is the external monitor chamber, such as figure 4. The differential cross section is calculated on every point, and the spectrum of scattered photon is estimated in local region on phantom surface. The vertical axis of estimated spectrum is differential cross section, and the horizontal axis is scattered photon energy.

3. Results and Discussions

The spectra of the scattered photon on the phantom surface are shown in figure 5. The upper right spectrum calculated by Klein-Nishina formula had reflected the differential cross section of the scattering angle 0 degree. Therefore the spectrum expresses the peak energies of the cobalt 60 γ-rays. On the other hand, the difference between the first and the second peak was large at the same point spectrum by EGS4. The scattered radiation from the long side of the external monitor chamber might affect the difference. At another position, the shapes and the peak energies were corresponding to the spectra of EGS4 and the Klein-Nishina formula. Therefore the interaction at the external monitor chamber is considered as Compton scatter mainly, and the number of the scatter is one times mostly.

The change of the effective energy of scattered photon by the distance from center is shown in figure 6. The maximum effective energy was 1.21 MeV at the center, and it decreased along with the distance from the center. The depth of maximum dose for 1.21 MeV is about 4 mm, therefore the scattered radiation may affect the absorbed dose in build up region.

The lateral dose profile of scattered radiation is shown in figure 7. The relative dose is normalized by the central axis dose at the phantom surface. The depth of maximum dose is the phantom surface, and it differed from the value calculated by the effective energy. The realistic depth of maximum dose is calculated by EGS4 because the irradiation angle of the scattered radiation is not considered for the determination of the effective energy.

The percentage-depth-dose (PDD) and off-center-ratio (OCR) are shown in figure 8. The percent local difference is +6.4% at the phantom surface and about -1% over the depth of maximum dose as shown in figure 9. The dose increased by the scattered radiation exists near the phantom surface, but the depth of maximum dose is not changed.

4. Conclusions

Using EGS4 and Klein-Nishina formula, we examined the effect of the scattered radiation of the external monitor chamber for the cobalt 60 γ-rays. The scattered radiation by the external monitor chamber was mainly caused by the Compton scatter. The effect of the scattered radiation existed near the surface, but the change of the dose profile was few. However the dose decreased about 1% under the position of the external monitor chamber. Therefore we should pay the attention to the distance between the external monitor chamber and the measurement chamber

References

1) Japan Society of Medical Physics, "Standard Dosimetry of Absorbed Dose in External Beam Radiotherapy (standard Dosimetry 01)," Tsusho-Sangyo Kenkyu-Sya, Tokyo, 2002.
2) R. Nelson, H. Hirayama, and D. W. O. Rogers, "The EGS4 Code System," SLAC-265 (Stanford Linear Accelerator Center, Stanford, CA, 1985).
3) Johns. H.E, Cunningham. J.R. "The physics of radiology 4th ed." Charles C Thomas, Springfield, 1983.
4) M. J. Berger and J. H. Hubbell, ''XCOM: Photon cross sections on a personal computer,'' National Bureau of Standards, NBSIR 87-3597, 1987.

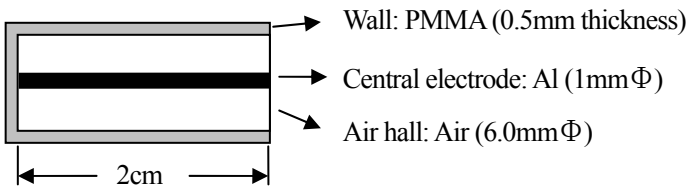

Figure 1. The model of the external monitor chamber

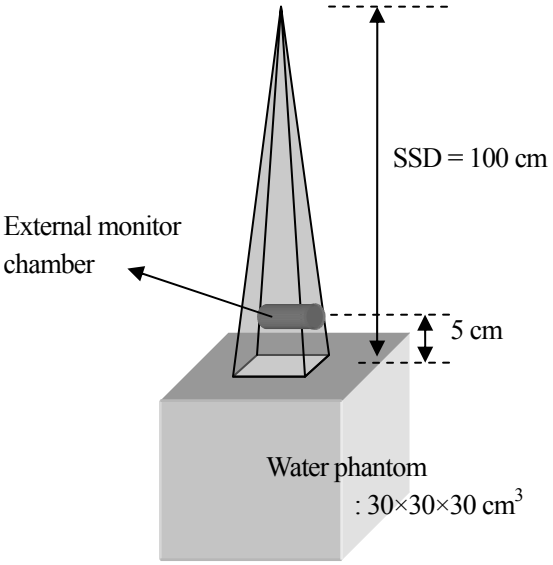

Figure 2. Geometry of this simulation

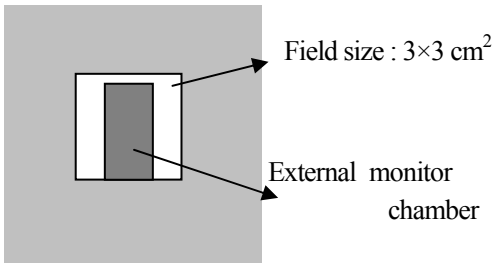

Figure 3. The irradiation field and the external monitor chamber

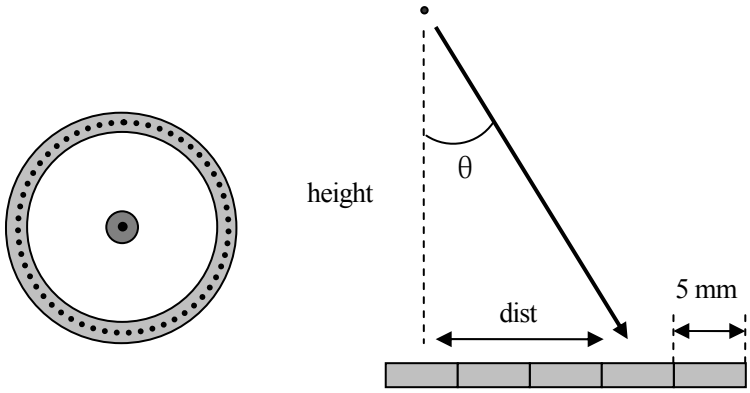

Figure 4. The simulation of the scattered photon spectrum using the Klein-Nishina formula. The left side figure shows the calculation point in chamber, and the black dots are calculation point. The right side figure shows translation for the scattering angle θ to the distance from center. The width of region to store the data on the phantom surface is set 5 mm.

Table 1 Material

Material	Components	PCUT [MeV]	ECUT [MeV]
PMMA	C, H, O	0.01	0.521
Al	Al	0.01	0.521
Air	H, O	0.01	0.521
Water	N, O, Ar	0.01	0.521

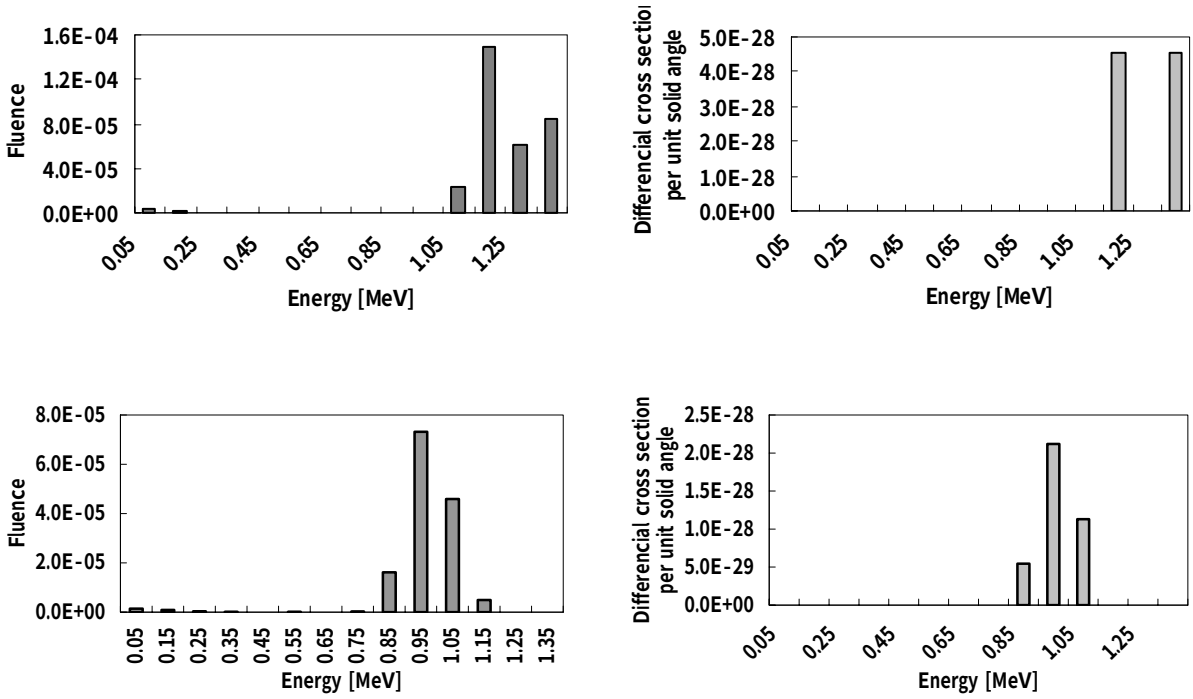

Figure 5. The energy spectrum of the scattered radiation calculated with EGS4 and the Klein-Nishina formula. For the upper row, distance from center was 0.0 cm, for the lower row, the distance from center was 2.5 cm. For the left column were calculated by EGS4, for the right column were calculated by using the Klein-Nishina formula.

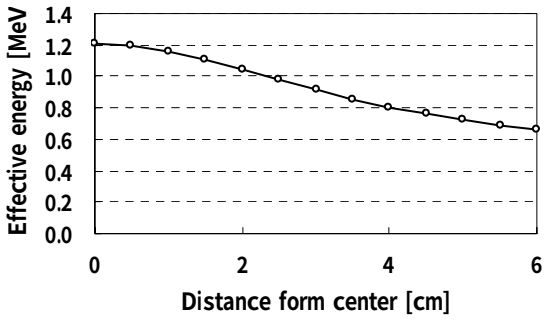

Figure 6. Effective energy of scattered photon

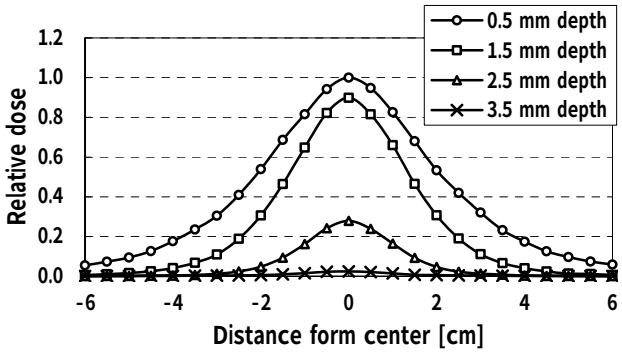

Figure 7. Lateral dose profile of scattered radiation

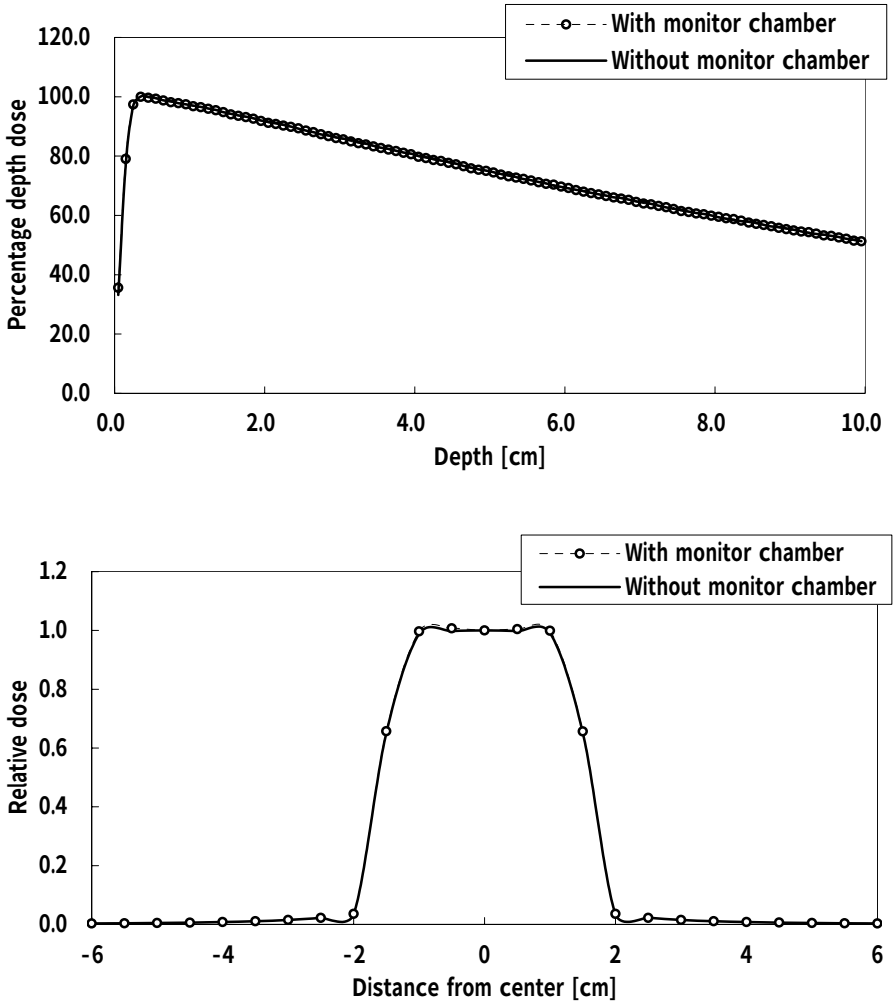

Figure 8. PDD curve at the center and OCR curve at the 5.0 cm depth. The dot profile, the external monitor chamber is set, and the solid line profile, the external monitor chamber is not set.

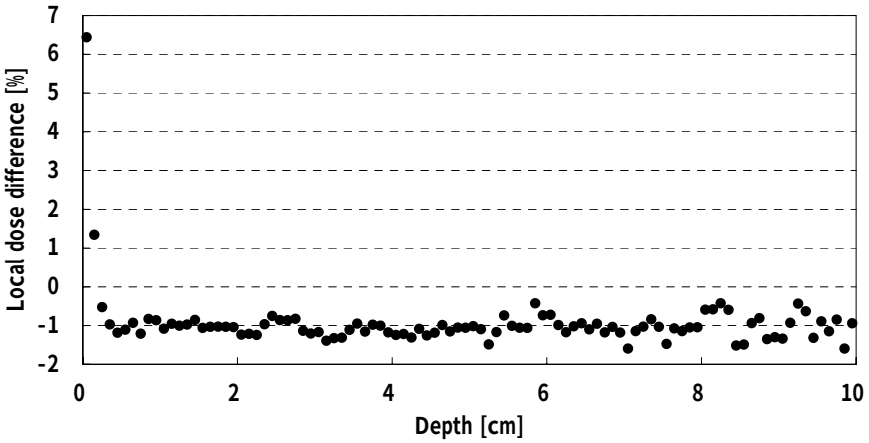

Figure 9. The percent local difference

A Study on Scattered Particles from Medical Linear Accelerator Head using Monte Carlo simulation

Tetsurou Katayose[1)], Hidetoshi Saitoh[1, 5)], Atsushi Myojoyama[1, 5)], Toru Kawachi[1)], Toru Kojima[1)], Yuichiro Narita[2, 5)], Tatsuya Fujisaki[3, 5)] and Kimiaki Saito[4, 5)]

[1)] Tokyo Metropolitan University Graduate School of Health Sciences, 116-8551, Japan
[2)] Kyoto University, Japan
[3)] Ibaraki Prefectural University of Health Sciences, Japan
[4)] Japan Atomic Research Institute, Japan
[5)] CREST, JST, Japan
e-mail: u5856601@gs.metro-hs.ac.jp

Abstract

In the absorbed dose calculation with Monte Carlo, Convolution and Superposition algorithm, actual energy spectrum of particles from treatment head is important information. To provide energy spectrum, Monte Carlo simulation is one of ideal method to reproduce actual beam properties, but it takes a lot of time to obtain adequate accuracy. Therefore, alternative simplified method is needed a replacement for the inefficient full Monte Carlo simulation of treatment head. In this report, to obtain properties of photons from treatment head, the energy, position, angle, charge, etc. of particles were sampled by simulation using the BEAMnrc Monte Carlo simulation code. And dose contribution of primary and scattered photons from each treatment head component to Head Scatter Factor (S_h) was analyzed. As a result, it was evident that the scattered photons, which are generated from a flattening filter, have the largest contribution to S_h.

1. Introduction

In the absorbed dose calculation with Monte Carlo, Convolution and Superposition algorithm, actual energy spectrum of particles from treatment head is important information. Monte Carlo simulation is one of ideal method to reproduce actual beam properties; variation of energy spectra and incident angle of particles due to field size and shape, because Monte Carlo method can most faithfully reproduce an actual physical phenomenon. But, it takes a lot of time for simulation.

Therefore, alternative simplified method is needed a replacement for the inefficient full Monte Carlo simulation of treatment head. For this purpose, it is needed to model treatment beam that the properties of particles from treatment head; energy spectrum, quantity and spatial distribution of primary and scattered particles. But, there are a few articles which reported properties of particles from each head component [1-4].

In this report, to obtain properties of photons from treatment head, the energy, position, angle, charge, etc. of particles were sampled by simulation using the BEAMnrc code. And dose contribution of primary and scattered photons from each treatment head component to Head Scatter Factor (S_h) [5] was analyzed.

2. Methods

2.1 Simulation

The BEAMnrc code [6] was used to simulate nominal 10 MV photon beams generated from a Clinac 21EX (Varian Medical Systems Co. USA). Fig. 1 shows schema of constructed treatment head and geometry of BEAMnrc simulation. The treatment head structure; target, primary collimator, beam window, flattening filter and secondary collimator were faithfully reproduced and the scoring plane was set in SSD 100 cm. Table 1

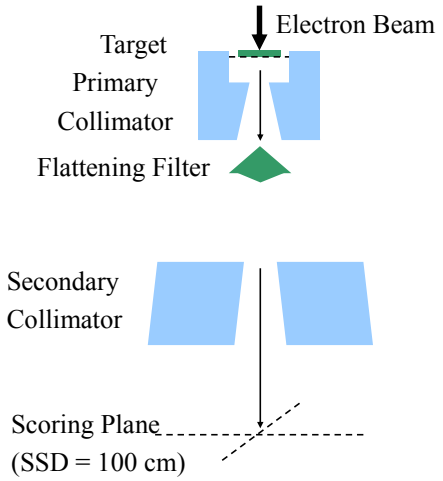

Fig. 1 Schema of constructed treatment head and geometry of BEAMnrc simulation.

Table 1 The input parameters of BEAMnrc simulation

Incident electron energy [MeV]	10.5
Energy distribution of incident electron [FWHM (%)]	3.0
Radial intensity distribution of incident electron [cm]	0.15
AE and ECUT [MeV]	0.700
AP and PCUT [MeV]	0.01
Number of incident electron	2×10^9

Table 2 The input parameters of DOSXYZnrc simulation

AE and ECUT [MeV]	0.521
AP and PCUT [MeV]	0.01
Number of incident particle	2×10^9

shows the input parameters of BEAMnrc simulation. Incident electron parameter was used the recommended value by Bagheri et al. [7] and A. Myojoyama et al. [8] for Clinac at nominal x-ray energy of 10 MV. The phase space files were created in air at scoring plane for several field sizes. The energy, position, angle, charge, etc. of particles were stored in a phase space file. The obtained phase space files were used for analysis of beam properties and as input data of the DOSXYZnrc code to calculate the dose distribution, namely, percentage depth dose (PDD) and off-axis ratio (OAR) in water. Table 2 shows the input parameters of DOSXYZnrc simulation.

2.2 Calculation of S_h

Collision kerma ($_{col}K$) of the water was calculated with obtained energy spectra at beam axis by using the following equation:

$$ {}_{col}K = \int_{E_{min}}^{E_{max}} E\,\Phi(E)\frac{\mu_{en}(E)}{\rho}\,dE \tag{1}$$

where $\Phi(E)$ is the photon fluence at energy E and $\mu_{en}(E)/\rho$ is the mass energy absorption coefficient for the water. The data of Seltzer, S.M. [9] was referred to the $\mu_{en}(E)/\rho$. The ratio of $_{col}K$ for several field sizes to 10 cm × 10 cm filed, namely, head scatter factor S_h were calculated by using the following equation:

$$ S_h(A) = \frac{{}_{col}K(A)}{{}_{col}K(A = 10\,\text{cm}\times 10\,\text{cm})} \tag{2}$$

2.3 Comparison of S_h

Calculated S_h was compared with measured. The relative deviation between the calculated S_h and the measured S_h was calculated by the following equation:

$$ \delta(A) = \frac{S_{h_c}(A) - S_{h_m}(A)}{S_{h_m}(A)} \tag{3}$$

2.4 Analysis of S_h

First, S_h is divided into primary and scattered component. Then, scattered component are divided into each head component to analyze contribution of S_h from each head component. Finally, scattered photon

component from the flattening filter was analyzed because the scattered photons from the flattening filter have the large contribution to the absorbed dose.

3. Results

3.1 Comparison of measured to calculated PDD and OAR

Calculated PDD was compared with the measured in 10 × 10 cm^2 field. Relative deviation at each depth deeper than the peak was less than 1 %. Calculated OAR was compared with the measured in 10 × 10 cm^2 field at depth in 2.5, 7.5 cm respectively. Relative deviation at each depth which is from - 4 cm to 4 cm was less than 2 % in field. The results of PDD and OAR are not shown on this paper because it is not main subject of this report, but it is confirmed that the treatment head simulation can reproduce actual treatment beam since simulated dose distribution is in good agreement with the measured one.

3.2 Comparison between measured and calculated S_h

Fig. 2 shows comparison between measured and calculated S_h as a function of field size. Fig. 3 shows relative deviation between measured and calculated S_h. Relative deviation at each field size was less than 1 %.

3.3 Relation of total, primary and scattered photons due to field size

Fig. 4 shows relation of total, primary and scattered photon fluence and Fig. 5 shows ${}_{col}K$ of water as a function of field size, respectively. There is significant variation of collision kerma owing to the scattered photons as the field size increased. On the other hand, there is slight variation of primary photons, because the data on central axis was used to calculate S_h. These results show that the variation of total photon fluence relates to variation of scattered photons owing to field size.

3.4 Component dependency

Fig. 6 shows relation of scattered photon fluence from each head component and field size and Fig. 7 shows the variation of ${}_{col}K$ of water of each component as a function of field size, respectively. It was evident that scattered photons from flattening filter have the largest contribution to absorbed dose and variation of S_h. and the contribution of secondary collimator to absorbed dose was not so significant.

Table 2 shows percentage of ${}_{col}K$ caused by scattered photons to ${}_{col}K$ caused by primary and scattered

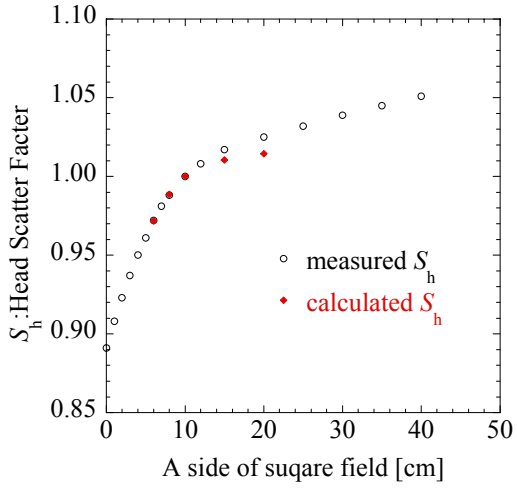

Fig. 2 Comparison between measured and calculated S_h as a function of field size.

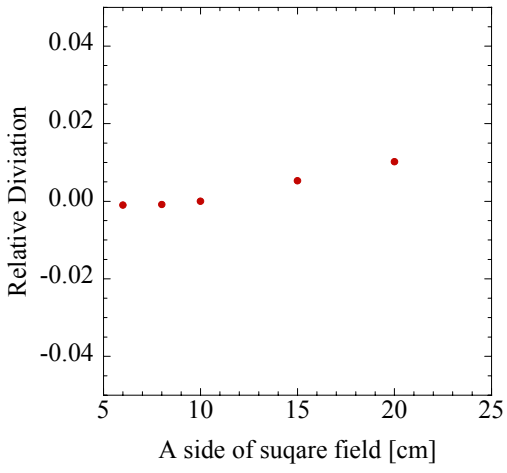

Fig. 3 Relative deviation between measured and calculated S_h.

photons as a function of field size. It was evident that the ratio of $_{col}K$ caused by scattered photons to $_{col}K$ caused by total photons is not so big. In 10 cm×10 cm field, dose contribution of the scattered photon to total photons was approximately 6.6%.

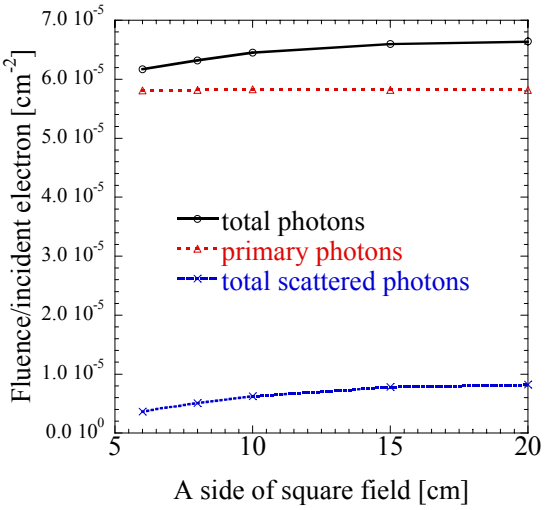

Fig. 4 Relation of total, primary and scattered photon fluence to field size.

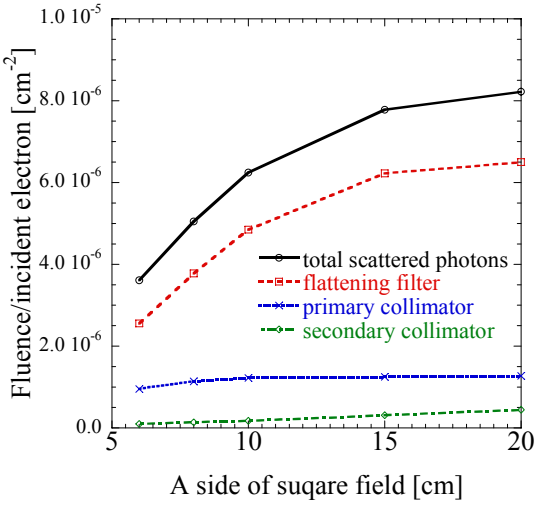

Fig. 6 Relation of scattered photon fluence from each head component to field size.

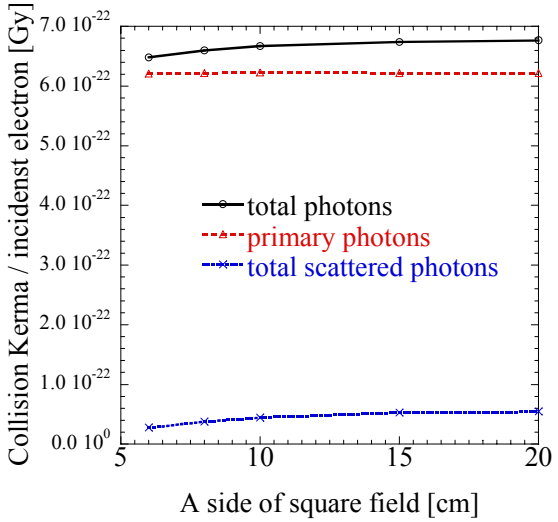

Fig. 5 Relation of $_{col}K$ caused by total, primary and scattered photons due to field size.

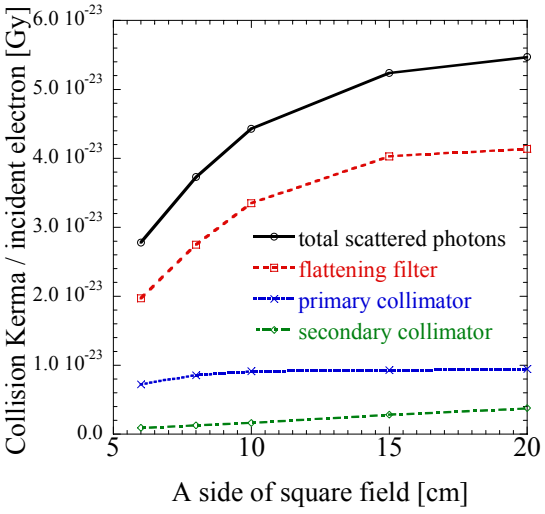

Fig. 7 Relation of $_{col}K$ caused by photons from each head component to field size.

Table 3 shows percentage of $_{col}K$ caused by scattered photons from each head component to that of total scattered photons as a function of field size. Among the dose contribution of the scattered photon, the percentage of the scattered dose which was generated from the flattening filter was 75.7%, 20.6%, from primary collimator and 3.7% from secondary collimator.

Table 2 Percentage of $_{col}K$ caused by scattered photons to $_{col}K$ caused by primary and scattered photons as a function of field size.

a side of square field [cm]	6	8	10	15	20
	4.3	5.7	6.6	7.8	8.1

Table 3 Percentage of $_{col}K$ caused by scattered photons from each head component to $_{col}K$ caused by total scattered photons as a function of field size

a side of square field [cm]	6	8	10	15	20
Primary collimator	25.9	22.9	20.6	17.8	17.3
Flattening filter	70.8	73.7	75.7	76.9	75.7
Secondary collimator	3.2	3.4	3.7	5.3	6.9

3.5 Analysis of scattered photons from flattening filter

The sampling plane was set under the flattening filter shown as fig. 8. By looking up at the flattening filter from central axis at 100 cm SSD, coordinate where scattered photons emitted from flattening filter surface were sampled.

Fig. 9 shows the relation between emitted position of scattered photon from flattening filter and number of scattered photon. In the vicinity of central axis, there is no variation due to field size, but number of photons decreased as the field size gets smaller in the outside.

4. Discussion

The dose contribution of the scattered photons from each head component to the S_h was analyzed. It was obvious that the variation of S_h mainly depended on photons scattered from flattening filter. But, scattered photons from primary collimator and secondary collimators might not be ignored for accurate dose calculation because variation of S_h was not quantitatively in agreement with variation of the only ${}_{col}K$ which scattered from flattening filter.

Emitted positions of scattered photons from flattening filter were sampled. In large field, scattered photons from the outside of flattening filter reached the sampling plane because the area where can be seen from the patient surface get more extensive. And there was a correlation between amount of scattered photon and thickness of the flattening filter. Therefore, there is a possibility that amount of scattered photons from a flattening filter can be determined using a area of flattening filter seen from the patient surface.

5. Conclusions

Photons which were generated at target, and scattered from primary collimator, flattening filter and secondary collimator were analyzed with Monte Carlo method. Furthermore, the dose contribution of scattered photons from each head component was analyzed.

As the results, it was evident that the scattered photons which were generated from the flattening filter have the largest contribution to S_h.

Acknowledgments

We appreciate Varian Oncology Systems Co. (USA) for giving us detailed data for the simulation of a medical treatment head.

References

1. Mohan, R., Chui, C. and Lidofsky, L.: Energy and angular distributions of photons from medical linear accelerators, Med. Phys. 12**,** 592－597, 1985.
2. D.V. Cormack and H. E. Johns: Spectral distribution of scattered photon beams, Phys. Med. Biol. 31, 839-858, 1986.
3. Saitoh, H., Fujisaki, T., Fukuda, K., et al.: Realistic energy spectra of a Cobalt-60 therapeutic beam, Jpn. J. Med. Phys. 18, 3a41-350, 1998.
4. E. L. Chaney, T. J. Cullip and T. A. Gabriel: A Monte Carlo study of accelerator head scatter, Med. Phys. 21, 1383-1390, 1994.
5. Khan FM, Sewchand W, Lee J, et al.: Revision of tissue-maximum ratio and scatter-maximum ratio concepts for cobalt 60 and higher energy x-ray beams, Med. Phys. 7, 230-237, 1980.
6. D.W.O. Rogers, B.A. Faddegon, G. X. Ding, et al.: BEAM: A Monte Carlo code to simulate radiotherapy treatment units, Med. Phys. 22, 503-524, 1995.

7. Sheikh-Bagheri D, Rogers DW.: Sensitivity of megavoltage photon beam Monte Carlo simulations to electron beam and other parameters, Med. Phys. 29, 379-390, 2002.

8. A. Myojoyama, H. Saitoh, T. Fujisaki, et al.: Optimal Parameters for Energy Spectral Calculations of Mega Voltage Photon Beam Using Monte Carlo Simulations, KEK proceedings 2005-3, 156-162.

9. Seltzer, S.M.: Calculation of Photon Mass Energy-Transfer and Mass Energy-Absorption Coefficients, Rad. Res. 136, 147-170, 1993.

CALCULATION OF BEAM QUALITY CORRECTION FACTOR USING MONTE CARLO SIMULATION

T. Kawachi[1], H. Saitoh[1], M. Inoue[2], A. Myojoyama[1], T. Katayose[1], T. Kojima[1] and K. Fukuda[1]

[1]Tokyo Metropolitan University Graduate School of Health Sciences, 116-8551, Japan
[2]Yokohama CyberKnife Center, 241-0014, Japan

Abstract

In recent years, a number of the CyberKnife systems (Accuray Co., U.S.) have been increasing significantly. However, the CyberKnife has unique treatment head structure and beam collimating system. Therefore, the global standard protocols can not be adapted for absolute absorbed dose dosimetry in CyberKnife beam. In this work, the energy spectrum of photon and electron from CyberKnife treatment head at 80 cm SSD and several depths in water are simulated with conscientious geometry using by the EGS Monte Carlo method. Furthermore, for calculation of the beam quality correction factor k_Q, the mean restricted mass stopping power and the mass energy absorption coefficient of air, water and several chamber wall and waterproofing sleeve materials are calculated. As a result, the factors k_Q in CyberKnife beam for several ionization chambers are determined. And the relationship between the beam quality index $PDD(10)_x$ in CyberKnife beam and k_Q is described in this report.

1. Introduction

It is widely recognized that the absorbed dose to water in high energy photon beam of quality $D_{w,Q}$ is given by:

$$D_{w,Q} = M_Q N_{D,w} k_Q \quad (1)$$

In this formula, M_Q is the corrected dosimeter reading in accordance with the reference conditions. $N_{D,w}$ is the calibration factor in terms of absorbed dose to water for the dosimeter at the reference quality of ^{60}Co gamma ray. And the beam quality correction factor k_Q is a chamber-specific factor which corrects for the difference between the reference beam quality and the user beam quality Q. For high-energy photons produced from clinical accelerators, the beam quality Q is specified by the tissue-phantom ratio $TPR_{20,10}$ or the percentage depth-dose at 10 cm depth $PDD(10)_x$ as beam quality index. The factors k_Q for a series of user beam qualities Q and a number of chamber types are provided by Andreo [1]. This method is recommended by the global standard protocols IAEA TRS-398 [2], AAPM TG-51 Report [3] and JSMP Standard Dosimetry 01 [4].

The CyberKnife system has unique and interesting treatment head structure and beam collimating system. For examples, it has no beam flattening filter, field shape is circular and shaped with cone collimator, normal treatment distance is 80 cm. Furthermore, although k_Q tabulated as a function of beam quality index $TPR_{20,10}$ or $PDD(10)_x$ for 100 cm SSD for 10 cm x 10 cm square field size in the standard dosimetry protocols, the field size is limited up to 60 mm field in diameter in CyberKnife system. CyberKnife beam unfortunately satisfy none of the reference dosimetry conditions, the global standard protocols consequently can not be adapted.

To solve this problem, it is indispensable to analyze the energy spectrum and calculate k_Q for beam

quality specification in CyberKnife beam. The Monte Carlo method is widely available for simulation of the particle transportation in the medical linear accelerator and absorbed dose distribution in various phantoms. At the moment, the beam commissioning approach by Monte Carlo simulation is the most accurate way of the beam modeling methods.

The purpose of this study is to establish the standard absorbed dose dosimetry for CyberKnife. Detailed description of the beam commissioning procedure will be discussed in following sections and the accuracy of our beam commissioning results will be proven by the various comparisons with measurement data. As a result, the beam quality correction factors k_Q corresponding to the beam quality index $PDD(10)_x$ for CyberKnife is reported.

2. Materials and Methods

2.1 Measurement of dose distribution

First of all, the PDD and the off-axis ratio; OAR in CyberKnife beam were investigated. The measured data include PDDs and OARs of 5 to 60 mm field diameter at 80 cm SSD. These data were measured in RFA300 water phantom (Scanditronix Wellhofer, Germany). The PDDs were measured using a PTW31014 PinPoint chamber (Physikalisch-Technische Werkstätten Germany) with a 0.015 cm^3 ionization volume and the OARs were measured using a Hi-*p*Si Stereotactic Field Detector (SFD) (Scanditronix Wellhofer, Germany) with a 0.6 mm diameter of active area for high spatial resolution.

2.2 Simulations

The treatment head was reconstructed on the simulation code with conscientious geometry and materials information prepared by Accuray Co. The energy spectra and dose distribution of CyberKnife were simulated using BEAMnrc and DOSXYZnrc which are developed by National Research Council of Canada (NRCC) [5, 6]. In the BEAMnrc code, the particle transport can be simulated with the reconstructed linear accelerator and the particles emitted from the accelerator can be sampled in Phase-space file. In the Phase-space file, information on the position, direction, charge and energy about all incident particles into the specified plane are preserved. Additionally, DOSXYZnrc is a code for 3-dimensional absorbed dose calculations and the Phase-space file can be available as input of energy spectrum on it.

The beam commissioning procedure using Monte Carlo simulation for CyerKnife can be classified into three main processes. The first process is the simulation using reconstructed treatment head and sampling of incident particles into Phase-space plane. Second is the calculation of dose distributions, and third process is estimation of the reproducibility by comparing the simulated dose distribution with the measured data.

In this work, the energy cutoffs were AE=ECUT=700 keV and AP=PCUT=10 kV for BEAMnrc simulations, and AE=ECUT=521 keV and AP=PCUT=10 kV for DOSXYZnrc.

2.2.1 Commissioning of PDDs

In principle, the energy spectrum of the x-ray beam is specified by energy of incident electrons on target. First, the energy of incident electrons on target was decided and Phase-space data was sampled at 80 cm SSD. Then, the PDD at intervals of 0.2 or 0.5 cm was simulated using the Phase-space data. In repetition of these simulations, the energy spectrum of x-ray beam which agreed with the actual PDD was determined by changing the properties of incident electrons. A comparison between the measured PDD; PDD_m and the calculated; PDD_c was estimated by relative deviations δ at each depth d_i in water and it is given by:

$$\delta(d_i) = \frac{PDD_c(d_i) - PDD_m(d_i)}{PDD_m(d_i)} \quad (2)$$

In addition, the beam commissioning was done by minimizing the sum of second power of these relative deviation $\Sigma\delta^2(d_i)$.

2.2.2 Commissioning of OARs

The calculated OARs were varied to agree with the measured by changing the spatial spread of incident electrons on target with Gaussian distribution. The Full Width at Half-Maximum; FWHM of Gaussian distribution was changed to 0, 2.0 and 4.0 mm, respectively. And the OARs at intervals of 2.0 mm for 80 cm SSD for 60 mm field were simulated in each FWHM.

2.3 Determination of k_Q

The beam quality correction factor k_Q is defined by:

$$k_Q = \frac{\left[\left(\bar{L}/\rho\right)_{w,air} P_{wall} P_{cav} P_{dis} P_{cel}\right]_Q}{\left[\left(\bar{L}/\rho\right)_{w,air} P_{wall} P_{cav} P_{dis} P_{cel}\right]_{^{60}Co}} \tag{3}$$

where, $(\bar{L}/\rho)_{w,\,air}$ is the mean restricted mass collision stopping-power ratio of water to air. P_{wall} is wall correction factor, P_{cav} is cavity correction factor, P_{dis} is displacement correction factor and P_{cel} is central electrode correction factor, respectively. In the equation (3), subscript Q shows user beam quality and ^{60}Co shows reference beam quality for ionization chamber calibration. To calculate these factors, the properties of ionization chambers were referred to IAEA TRS-398. In the following sections, more concrete procedure of k_Q determination is mentioned.

2.3.1 Mean restricted mass collision stopping power ratio; $(\bar{L}/\rho)_{med,\,air}$

The mean restricted mass collision stopping-power ratio of water and several wall and sleeve materials to that of air was computed in SPRRZnrc code [5] using the energy spectrum of the photons obtained by above mentioned method 2.2. In the SPRRZnrc, $(\bar{L}/\rho)_{med,\,air}$ was calculated by the following equation.

$$(\bar{L}/\rho)_{med,air} = \frac{\int_{\Delta}^{E_{max}} \Phi(E)\,(L(E)/\rho)_{med}\,\mathrm{d}E + \Phi(\Delta)\,(L(\Delta)/\rho)_{med}}{\int_{\Delta}^{E_{max}} \Phi(E)\,(L(E)/\rho)_{air}\,\mathrm{d}E + \Phi(\Delta)\,(L(\Delta)/\rho)_{air}} \tag{4}$$

where, Δ is cut off energy and it was set to10 keV.

2.3.2 Overall perturbation correction factor and beam quality correction factor; P_Q and k_Q

The mean mass energy absorption coefficient ratios of water to that of several chamber walls and water proofing materials are required to calculate the factor P_{wall}. The mean mass energy absorption coefficient ratio was calculated using simulated energy spectrum of photon in water and given by following equation.

$$(\bar{\mu}_{en}/\rho)_{water,med} = \frac{\int_0^{E_{max}} E\;\Phi(E)\,(\mu_{en}(E)/\rho)_{water}\,\mathrm{d}E}{\int_0^{E_{max}} E\;\Phi(E)\,(\mu_{en}(E)/\rho)_{med}\,\mathrm{d}E} \tag{5}$$

Using these parameters, the wall correction factor P_{wall} was calculated according to Hanson report [6]. The cavity correction factor P_{cav} is 1.000 when charged particle equilibrium is established [2]. The central

electrode correction factor P_{cel} was 1.000 or 0.994 according to report of Rogers [7]. The displacement correction factor P_{dis} was obtained by:

$$P_{dis} = \frac{PDD(d)}{PDD\left(d - 0.6r_{cyl}\right)} \tag{6}$$

where, r_{cyl} is a radius of ionization cavity.

3. Results and Discussion

3.1 Beam commissioning

The comparisons of PDD between the measured and the beam commissioned results at SSD 80 cm for 60 mm field diameter are shown in Fig. 1. These relative deviations in each depth are also in Fig. 1. The largest deviation between the two is 0.7 %, even if including an error bar, the deviation dose not exceed 1.0%.

Fig. 2 shows a comparison between the measured and the calculated OARs (a) at 5 cm and (b) at 15 cm depth in water at 80 cm SSD for 60 mm field. When FWHM is set to 4.0 mm, the calculated has best agreement with the measured OAR. The results of Fig. 1 and Fig. 2 show that reconstructed treatment head can reproduce the actual energy spectrum and intensity distributions.

It is important to evaluate the difference of the photon energy spectrum of CyberKnife system and the ordinary linear accelerator at the phantom surface. Fig. 3 shows normalized photon energy spectrum of the CyberKnife and an ordinary 6 MV linear accelerator at phantom surface. In comparison with ordinary linear accelerator, CyberKnife beam is softer because the beam hardening effect doses not take place by absence of flattening filter.

3.2 Beam quality correction factor; k_Q

Fig. 4 shows the beam quality correction factors k_Q as a function of depth in water and k_Q are plotted as a function of field diameter in Fig. 5, respectively. In the Fig. 5, k_Q for the chambers whose ionization cavity length is less than 10 mm are plotted. These results show that k_Q depend on field size and depth and k_Q slightly decreases as smaller field size and deeper point. From the Fig. 4, when k_Q at 10 cm depth in water is introduced, the uncertainty of k_Q by the depth is estimated from -0.23 to 0.28 %. Similarly, from the Fig. 5, when k_Q for 6 cm diameter field is introduced, the uncertainty of k_Q by field size is estimated from 0 to -0.46 %.

In the table 1, the factors k_Q for several ionization chambers are tabulated as a function of beam quality index $PDD(10)_{CK}$. $PDD(10)_{CK}$ is defined as PDD at depth of 10 cm, for 60 mm field diameter and 80 cm SSD. These k_Q are prepared for water sleeve thickness of 0.1 g cm^{-2}.

4. Conclusions

The beam quality correction factors k_Q as a function of $PDD(10)_{CK}$ for several ionization chambers are determined. The k_Q factors are recommended for the condition of 10 cm depth in water and 60 mm field diameter since depth 10 cm is in accordance with calibration depth in the global dosimetry protocols and variation of OAR in chamber length is negligible in 60 mm field for CyberKnife beam. In the recommended reference conditions, uncertainty of k_Q is estimated within ±0.3 % by depth and the up to -0.46 % by field.

Acknowledgments

We wish to thank Accuray Co., Chiyoda Technol Co. and Accelerator Technology Co. for courtesy of the valuable information related CyberKnife. We are also appreciative of the Dr. Tomaru's helpful suggestions. This work was supported by a specified research grant-in-aid 2004-2005 of JASTRO.

References

1) Andreo. P., Absorbed dose beam quality factors for the dosimetry of high-energy photon beams, Phys Med Biol 37 (1992) 2189-2211.
2) IAEA: Absorbed dose determination in external beam radiotherapy – An international code of practice for dosimetry based on standards of absorbed dose to water -, Code of practice for high energy electron beams, TRS-398, IAEA, Vienna, 2001.
3) AAPM Task Group 51: Protocol for Clinical Dosimetry of High-Energy Photon and Electron Beams, Medical Physics 26, 1847-1870, 1999.
4) JSMP: Standard dosimetry of absorbed dose in external beam radiotherapy, Standard Dosimetry 01, Tsusho Sangyo Kenkyu Sha, Tokyo, 2002.
5) Nelson, W.R.,Hirayama, H.D. and Rogers, D.W.O.: The EGS4 code system, SLAC Report SLAC-265, 1985.
6) Rogers, D.W.O., Faddegon, B.A.,Ding, G.X., et al.: BEAM: A Monte Carlo code to simulation radiotherapy treatment units, Med. Phys.22, 503-524,1995.
7) Hanson W. F., Dominguez Tinoco J. A.: Effects of plastic protective caps on the calibration of therapy beam in water, Med Phys 12 243-248, 1985.
8) Rogers DWO: Fundamentals of dosimetry based on absorbed-dose standards. (In) Teletherapy physics, present and future edited by Palta JR and Mackie TR 319-356, 1996 AAMP Washington DC.

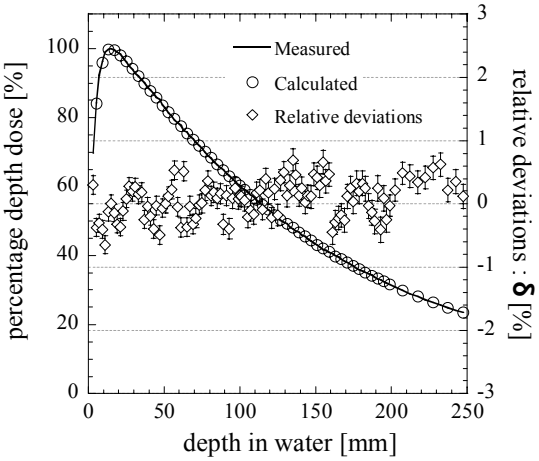

Figure 1. A comparison of PDD between the measured and calculated in water for 80 cm SSD with 60 mm field diameter. Relative deviations δ are also plotted as a function of depth in water.

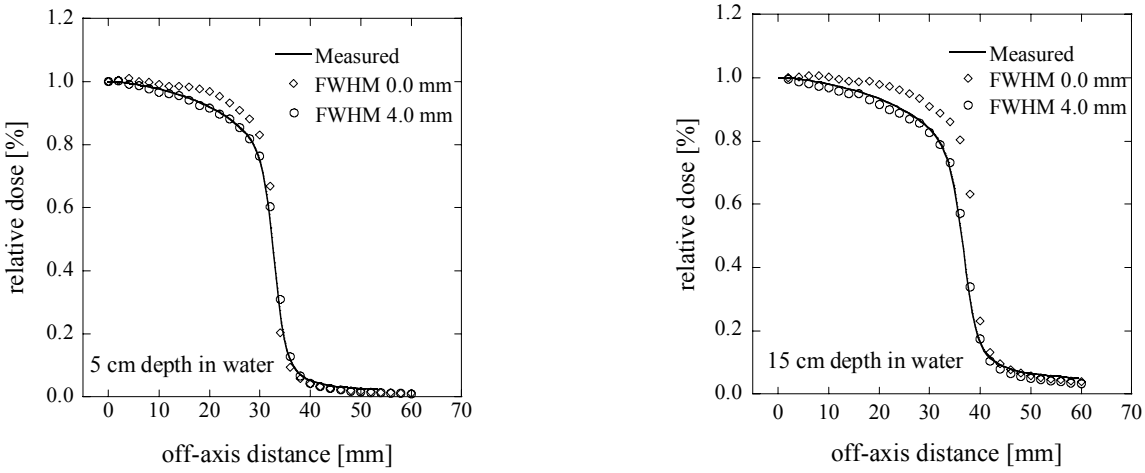

(a) 5 cm depth in water (b) 15 cm depth in water

Figure 2. A comparison of the OARs between the measured and calculated at (a) 5 cm and (b) 15 cm depth for 80 cm SSD with 60 mm field diameter

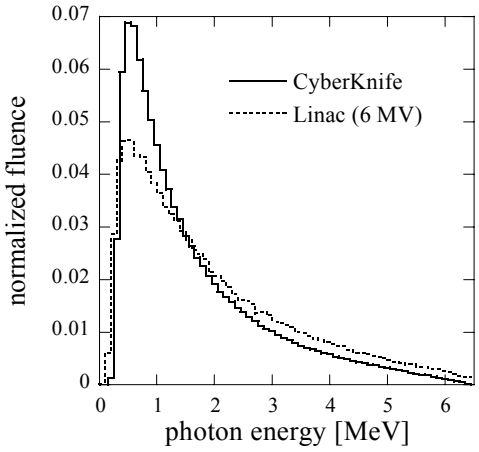

Figure 3. A comparison of photon energy spectrum between the CyberKnife and ordinary 6 MV linear accelerator at the phantom surface. (Field size is 60 mm in diameter for CyberKnife and 10 cm x 10 cm for linear accelerator.)

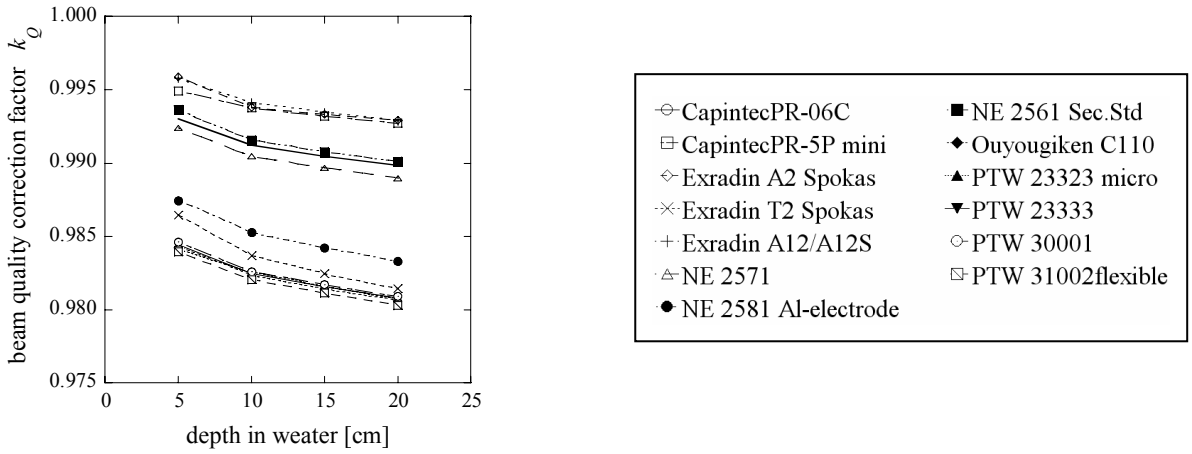

Figure 4. The beam quality correction factor k_Q for several ionization chambers for CyberKnife as a function of depth in water. (Field size = 60 mm in diameter).

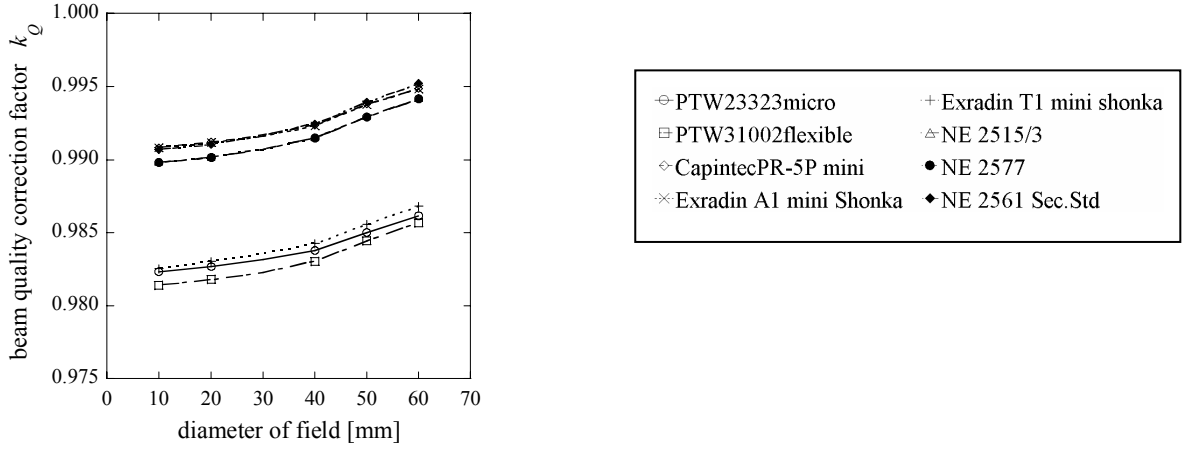

Figure 5. The beam quality correction factor k_Q as a function of field diameter for ionization chambers whose ionization cavity length are less than 10 mm.

Table 1. Beam quality correction factors k_Q of several ionization chambers for CyberKnife beam. (For field diameter=6 cm, depth in water=10 cm and PMMA 0.1 g cm^{-2} water proof sleeve)

Ionization chamber	$PDD(10)_{CK}$						
	58.0	59.0	59.5	60.0	60.5	61.0	62.0
Capintec PR-06C	0.993	0.992	0.992	0.992	0.991	0.991	0.990
Capintec PR-5P mini	0.995	0.994	0.994	0.994	0.994	0.994	0.993
Capintec PR-5 mini	0.995	0.994	0.994	0.994	0.994	0.994	0.993
Exradin A2 Spokas	0.995	0.994	0.994	0.994	0.994	0.994	0.994
Exradin T2 Spokas	0.988	0.986	0.985	0.984	0.984	0.983	0.981
Exradin A1 mini	0.995	0.994	0.994	0.994	0.993	0.993	0.993
Exradin T1 mini	0.988	0.986	0.985	0.984	0.983	0.982	0.981
Exradin A12/A12S	0.996	0.995	0.995	0.994	0.994	0.994	0.993
NE 2515/3	0.993	0.992	0.991	0.991	0.991	0.990	0.989
NE 2577	0.993	0.992	0.991	0.991	0.991	0.990	0.989
NE 2505/3, 3A	0.993	0.992	0.991	0.991	0.990	0.990	0.989
NE 2571 F	0.993	0.992	0.991	0.991	0.990	0.990	0.989
NE 2581 A-150 elec	0.988	0.986	0.986	0.985	0.984	0.984	0.982
NE 2581 Al elec	0.989	0.987	0.987	0.986	0.985	0.985	0.983
NE 2561 Sec.Std	0.993	0.993	0.992	0.992	0.992	0.991	0.990
Ouyougiken C110	0.985	0.984	0.984	0.983	0.982	0.982	0.980
PTW23323micro	0.986	0.984	0.984	0.983	0.982	0.982	0.980
PTW23331rigid	0.985	0.984	0.984	0.983	0.982	0.982	0.981
PTW23332rigid	0.985	0.984	0.984	0.983	0.982	0.982	0.980
PTW23333F	0.985	0.984	0.984	0.983	0.982	0.982	0.981
PTW30001F	0.986	0.984	0.984	0.983	0.983	0.982	0.981
PTW30010F	0.985	0.984	0.984	0.983	0.982	0.982	0.981
PTW30002/30011	0.992	0.991	0.991	0.991	0.990	0.990	0.989
PTW30004/30012	0.993	0.992	0.992	0.992	0.991	0.991	0.990
PTW30006/30013	0.985	0.984	0.984	0.983	0.982	0.982	0.981
PTW31002flexible	0.985	0.984	0.983	0.983	0.982	0.981	0.980
PTW31003flexible	0.985	0.984	0.983	0.983	0.982	0.981	0.980
Victoreen 30-348	0.992	0.990	0.990	0.989	0.989	0.988	0.987
Victoreen 30-351	0.992	0.990	0.990	0.989	0.989	0.988	0.987
Victoreen 30-349	0.992	0.990	0.990	0.989	0.989	0.988	0.987
Victoreen 30-361	0.992	0.990	0.990	0.989	0.989	0.988	0.987

A STUDY ON DEPTH-SCALING OF PLASTIC PHANTOM IN ELECRON BEAM DOSIMETRY

T. Kojima, H. Saitoh, T. Kawachi, T. Katayose, A. Myojyoyama

Tokyo Metropolitan University, Graduate School of Health Sciences, TOKYO, JAPAN
e-mail: tool@maple.ocn.ne.jp

Abstract

In recommendations of several standard dosimetry[1, 2, 3], water is defined as the reference medium, however, the water substitute plastic phantoms are highly discouraged. Nevertheless, in the case of accurate chamber positioning in water is not possible, or no waterproof chamber is available, their use is permitted at beam qualities $R_{50} < 4$ g/cm^2 ($E_0 < 10$ MeV). For the electron dosimetry using plastic phantom, a depth-scaling factor is used for converting ranges and depths measured in plastic phantoms into the equivalent values in water. In this report, three different kinds of depth scaling factor which are c_{pl} obtained from a ratio of electron average penetration depth; z_{av}, half value depth ratio; $(R_{50})_{w,m}$ from Monte Carlo dose calculation and that from measurements, are compared each other. As a result, there are slight differences in depth-scaling factor between obtained from simulation results and from measurements. These results indicate that c_{pl} has to be studied more detail for the sake of precise electron dosimetry in plastic phantoms.

1. Introduction

In several recommendations in standard dosimetry, water is defined as the reference medium, whereas the water substitute plastic phantoms (plastic phantoms) are discouraged because they have the largest discrepancies in the determinations of absorbed dose. However, almost users in hospitals are confusing because of difficulty in accurate chamber positioning in water, availability of a waterproof chamber and unpopularity to use a waterproof chamber. Therefore, plastic phantom use is permitted at beam qualities $R_{50} < 4$ g/cm^2 (i.e., $E_0 < 10$ MeV) for the electron dosimetry.

Ideally, any solid phantom material should be water equivalent, which requires that it has the same liner collision stopping power and the same linear angular power as water. This requirement can be met only if the phantom material has the same electron density and effective atomic number as water. The more popular nonwater phantoms are made of plastic, but because of their high carbon content, their effective atomic number is usually lower than that of water. This results in too low a linear angular scattering power when the linear collision stopping power equals that of water. The addition of a high Z material to the plastic can reduce this difference.

If the phantom is not water equivalent, then it will be necessary to correct the measured dose distribution for the effects of the phantom. The depth dose can be corrected (a) by properly scaling the depth in the phantom to its water-equivalent depth and (b) by applying fluence correction factors for converting the ionization measured in the phantom to that in water. Dose-distribution in a plastic phantom can be converted to appropriate dose-distribution in water by means of depth-scaling. To convert a measurement depth z_{pl} (g cm^{-2}) in a plastic phantom, appropriate depth in water z_w (g cm^{-2}), depth-scaling factor; k is used following expression

$$z_w = z_{pl} \cdot k$$

So far, several depth-scaling methods have been reported. In the ICRU Report 35[4], the linear continuous-slowing-down approximation (csda) range ratio of water to plastic phantom was introduced. This method is assuming that ranges are proportional to the csda range and accounts for continuous collision and radiative energy losses only. The depth-scaling factor obtained from csda range ratio can be calculated by following equation

$$(r_0)_{\mathrm{pl}}^{\mathrm{water}} \cdot \rho_{\mathrm{pl}}^{\mathrm{water}} = \frac{r_{0,\,\mathrm{water}}\,\rho_{\mathrm{water}}}{r_{0,\,\mathrm{pl}}\,\rho_{\mathrm{pl}}} \tag{1}$$

where, $r_{0,\mathrm{water}}$ and $r_{0,\mathrm{pl}}$ is the csda range (cm) in water and plastic phantom, ρ_{water} and ρ_{pl} is the density (g cm^{-3}) of water and plastic phantom, respectively.

AAPM Task Group 25[5] recommend an effective density; ρ_{eff} for depth-scaling. The ρ_{eff} means the ratio of half-value depth of either dose or ionization; R_{50} in plastic to that in water which is obtained from measurement of PDD or PDI curves, firstly. And then, the ratio of R_{50} in water to that in the plastic phantom; $(R_{50})_{\mathrm{w,m}}$ can be calculated following next equation

$$(R_{50})_{\mathrm{w,m}} = \frac{(R_{50})_{\mathrm{water}}}{(R_{50})_{\mathrm{plastic}}} = \rho_{\mathrm{eff}} \tag{2}$$

Although effective density is called different from depth-scaling factor, the use of this factor is the same. It should be emphasized, however, that scaling according to R_{50} strictly requires the knowledge of these two quantities both in plastic and in water. Therefore, full depth–dose distributions in the two media are needed; this is precisely what, in practice, the user wants to avoid by performing measurements in plastic confronted with the difficulties of measuring in water at low electron energies.

After that it has been cleared that multiple scattering could considerable affect penetration depths of electrons, the new depth-scaling methods using depth-scaling factor C_{pl}[6] (also in the IAEA TRS-381)[7] and c_{pl} (in the IAEA TRS-398[2] have been proposed. Both C_{pl} and c_{pl} are the ratio of the average depth of electron penetration in water to that in plastic phantom, nevertheless depth for C_{pl} is defined in unit of cm and for c_{pl} is expressed in g cm^{-2}. The c_{pl} is the ratio of the average electron penetration depth in water to that in plastic phantom, defined as

$$c_{\mathrm{pl}} = \frac{z_{\mathrm{av}}^{\mathrm{water}}\,\rho_{\mathrm{water}}}{z_{\mathrm{av}}^{\mathrm{pl}}\,\rho_{\mathrm{pl}}} \tag{3}$$

where, $z_{\mathrm{av}}^{\mathrm{water}}$ and $z_{\mathrm{av}}^{\mathrm{pl}}$ is an average penetration depth (cm) in water and plastic phantom, ρ_{water} and ρ_{pl} is density (g cm^{-3}) of water and plastic phantom material, respectively.

However, this depth-scaling factor, c_{pl} was calculated under the non-clinical condition, in which incident electrons on phantom surface did not have an angular distribution and beam divergence (i.e., pencil beam). That might have some effect on C_{pl} and c_{pl}. In order to adjust these two different situations, percentage depth dose (PDD) curves, which are measured under the clinical condition (i.e., broad beam), should be changed to parallel beam according to the way of calculating c_{pl}.

In this study, the properties, especially depth-scaling factor c_{pl} of two commercially available water substitute plastic phantoms were determined using EGSnrc ver.4.0 which was different from early reports. Furthermore, there were few studies on electron dosimetry comparing between these simulated scaling methods and the measurements of PDD by clinical beams. The aim for this study is to evaluate this calculated depth-scaling factor of several plastic phantoms and whether only one factor used for depth-scaling is suitable.

2. Materials and Methods

2.1 Calculation of two depth-scaling factors; c_{pl} & r_0

In this work, two different depth-scaling methods were calculated for two commercially available plastic phantoms; RMI-457 (GAMMEX RMI, Wisconsin, USA) and WE-211 (Kyoto Kagaku, Kyoto, Japan). The composition of two plastic phantoms were reproduced faithfully following IAEA TRS-398[1] and JSMP01[3].

2.1.1 Average penetration depth ratio: c_{pl}

To calculate z_{av}, original user code on EGSnrc ver.4.0 was coded newly. Monoenergetic electron pencil beam of energies from 1 to 20 MeV have been assumed to impinge normally on finite slab of water and the others. The transport of primary electrons has been followed down to the cutoff energy at 10 keV, penetration depths of each history were sampled and z_{av} was calculated. The number of simulated histories was 10^6 in each case. In standard dosimetry protocol[1,2], c_{pl} is adopted as averaging from at 6 to 10 MeV, in such a low energy, plastic phantoms are frequently used in electron dosimetry, due to difficulty in precise positioning of chamber in water.

2.1.2 Continuous-slowing-down approximation ratio: r_0

In this study, csda range in water and that in plastic phantoms were recalculated according to ESTAR[8] from energy of 1 to 20 MeV. Also in calculating c_{pl}, $(r_0)_{pl}^{water}$ is adopted as averaging from at 6 to 10 MeV.

2.2 Half value depth ratio $(R_{50})_{w,m}$ measurements

2.2.1 Measurements of $(R_{50})_{w,m}$ in clinical beam

For estimation of c_{pl} derived from z_{av} ratio, measurements were performed with the clinical electron beam (Clinac 2100C, Varian Medical Systems, U. S.) at nominal electron energy was 6 and 9 MeV. In this study, the measurement apparatus and conditions were followings, field size was 10 cm x 10 cm, SSD was 100 cm, plane-parallel chamber were either Markus type PTW 23343(Physikalisch-Technische Werkstätten, Germany) or NACP-02 (Scanditronix, Sweden) and digital electrometer was Keithley 35040 (Keithley, USA), respectively. In water, Markus type chamber had to be capped with a PMMA plate over the upper side of electrode, whereas uncapped in plastic phantom. In this respect, Markus type chamber was different from NACP chamber. Before measurements, in order to correct differences of density in each plastic phantom, weight and volume were carefully measured all plastic phantoms used in measurements. Moreover, for the sake of eliminating a charge storage problem, plastic phantoms whose thickness with exceeding 2 cm was kept out from these measurements[7].

Throughout measurements, PDI curves, after that, half-value depth (g cm^{-2}); R_{50} in water, RMI-457 and WE-211 were obtained. And then, $(R_{50})_{w,m}$, which means the R_{50} ratio of water to plastic phantom and same as ρ_{eff}, for each plastic phantom was calculated with equation (2).

2.2.2 Divergence correction with effective source to surface distance in the air[5]

The depth-scaling factor, c_{pl} was calculated under non-clinical condition, in which electron incident on phantom did not have angular distribution and beam divergence. That might have some effect on C_{pl} and c_{pl}. In order to adjust these two different situations, percentage depth dose (PDD) curves, which are measured with clinical broad beam, should be changed to parallel beam.

In order to correct for beam divergence, the measured values of dose or ionization at each depth should be multiplied by next factor.

$$\frac{(SSD_{eff}+d)^2}{(SSD_{eff})^2} \tag{4}$$

where, SSD_{eff} stands for effective source to surface distance which is a series of output measurements are made in a phantom at the depth of dose maximum as a function of the air gap g between the cone end (or the plane perpendicular to the beam axis at the nominal SSD) and the phantom surface. And Q_0 is the ionization charge reading with zero gap and Q_g is the reading with gap g.

In general, Q_0 and Q_g are affected by SSD and scattered radiation from inside phantom but in this study

incident electron fluence on phantom surface has to be considered. For the sake of eliminating the scattered electrons and photons from inside phantom, Q_0 and Q_g are measured without phantom, in other words, measured in the air. And PMMA discs with several thicknesses are put on the chamber to satisfy measurement at the maximum ionization depth. Then, in accordance with the assumption of the inverse-square law, following expression is obtained

$$\left(\frac{Q_0}{Q_g}\right)^{1/2} = \frac{g}{(\mathrm{SSD}_{\mathrm{eff}} + d)} + 1 \qquad (5)$$

where, d is the depth of measurement. By plotting $[Q_0/Q_g]^{1/2}$ as a function of g, a straight line is obtained having slope $1/(\mathrm{SSD}_{\mathrm{eff}} + \mathrm{d})$. The $\mathrm{SSD}_{\mathrm{eff}}$ is then equal to

$$SSD_{eff} = (1/\mathrm{slope}) - d \qquad (6)$$

2.3 Calculation of $(R_{50})_{w,m}$ with DOSXYZnrc

Two different kinds of scaling factor were taken from above two methods. These two methods are quiet different from each other. One is obtained from theoretical calculation and the other is measurement. In order to compare between two methods, $(R_{50})_{w,m}$ for two plastic phantom was calculated with DOSxyznrc of Monte Carlo simulation code.

In this simulation, PDD curve can be taken easily and input parameters were followings, monoenergetic broad beam electrons with 1 to 10 MeV hit on the phantom surface at 10x10 cm^2 field, SSD of 100 cm, and sampled voxel of 1x1x0.1 cm^3 along central axis, respectively. The cut-off energy for electrons was 0.01 MeV and that for photons was 0.01 MeV. The number of simulated histories has been 10^6 in each case. The $(R_{50})_{w,m}$ of WE-211 and RMI-457 were obtained from each PDD curve using equation (4).

3. Results

Figure 1 shows two depth-scaling factors c_{pl} of RMI-457 and WE-211 with EGSnrc ver.4.0 as a function of electron energy at phantom surface. The values of c_{pl} using both plastic phantoms were within 0.94 to 0.96 through 1 to 20 MeV. These values slightly depend on the incident electron energy E_0 at a phantom surface.

Table 1 shows a comparison of c_{pl} which is obtained from the z_{av} ratio both in our Monte Carlo simulation and in early reports from Saitoh[8] and csda range ratio calculated from ESTAR[9]. Although the number of particle histories was increased by 10 times, c_{pl} values were same as the results from Saitoh[8]. Compared to IAEA TRS-398, c_{pl} in this study is different by 0.3% higher.

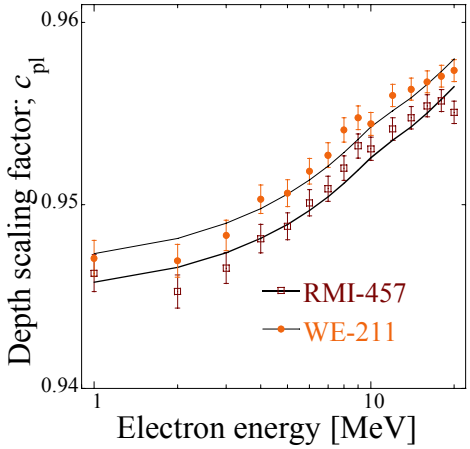

Figure 1. Depth-scaling factors, c_{pl}, from z_{av} ratio as a function of the incident electron energy [MeV].

Table 1. Comparison of c_{pl} obtained from z_{av} ratio and r_0.

	Histories	RMI-457	WE-211
TRS-398 [2,5]	2x10^5	0.949	—*1
Saitoh[8]	1x10^5	0.952	0.954
This study	1x10^6	0.952	0.954
r_0 *2	—	0.974	0.972

*1: no available data

*2: r_0 stands for csda range ratios calculated from ESTAR[8]

Figure 2(a) and (b) show the PDD curves at E_0 of 6 MeV using Markus type chamber in RMI-457 and WE-211, and (c) and (d) with NACP chamber in RMI-457 and WE-211, respectively. PDD curves in plastic phantom without correction got at deeper than water (i.e., in plastic, electron could penetrate deeper rather than water). To correct this difference, c_{pl} correction was adopted. As a result, contrary to without correction, corrected PDD curve went to shallower depth. According to these results, depth correction with c_{pl} derived from z_{av} might make range in plastic shorten, in other words, depth-scaling factor was overestimated.

Same tendencies are also observed in at E_0 of 9 MeV with both chambers and both phantoms. Because of the repetition of the results at 6 MeV, results at 9 MeV are not printed on this paper.

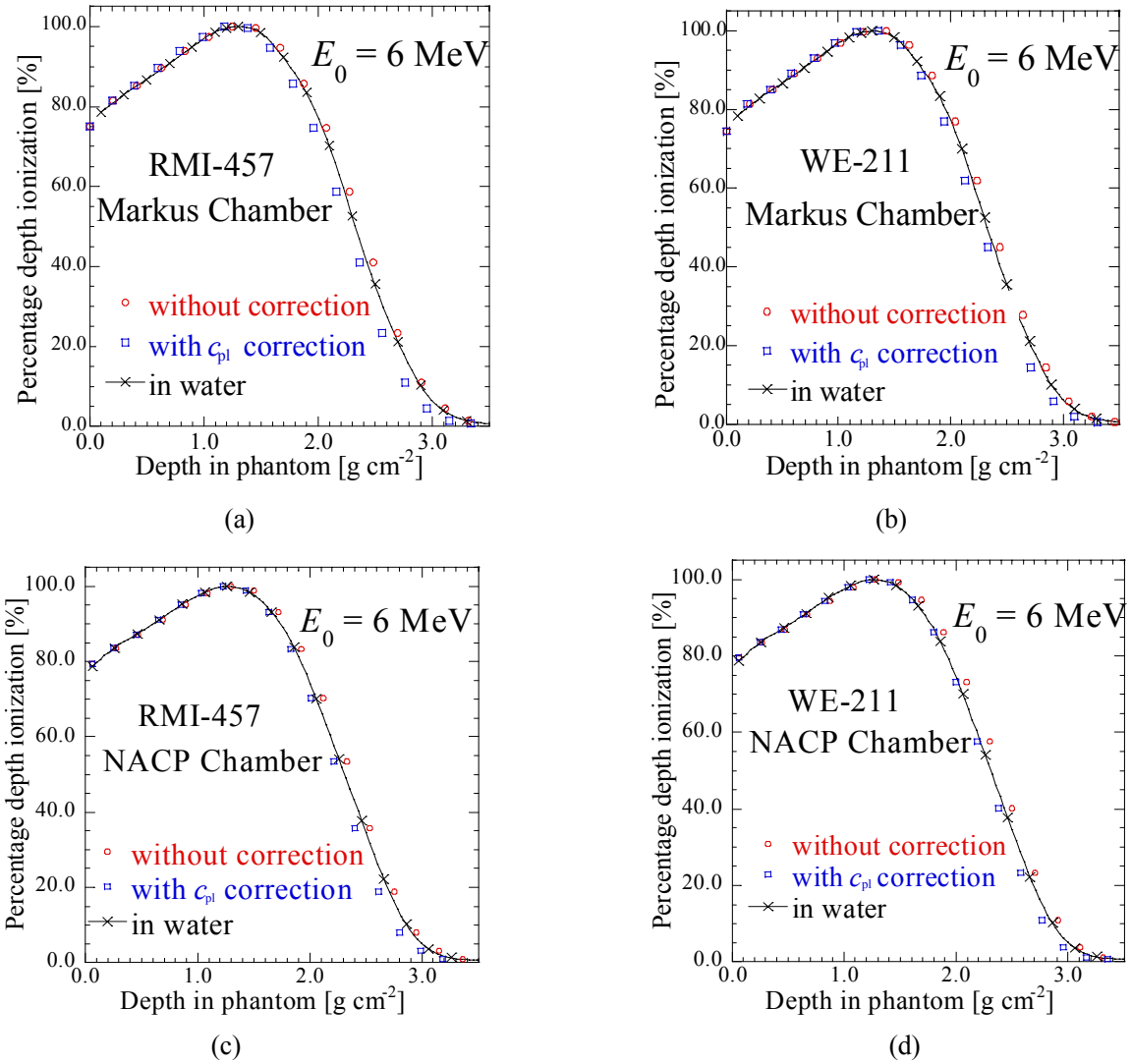

Figure 2. PDI curves measured at E_0 of 6 MeV in RMI-457 (a) and WE-211 (b) with Markus type chamber, and each phantom with NACP chamber (c), (d), respectively.

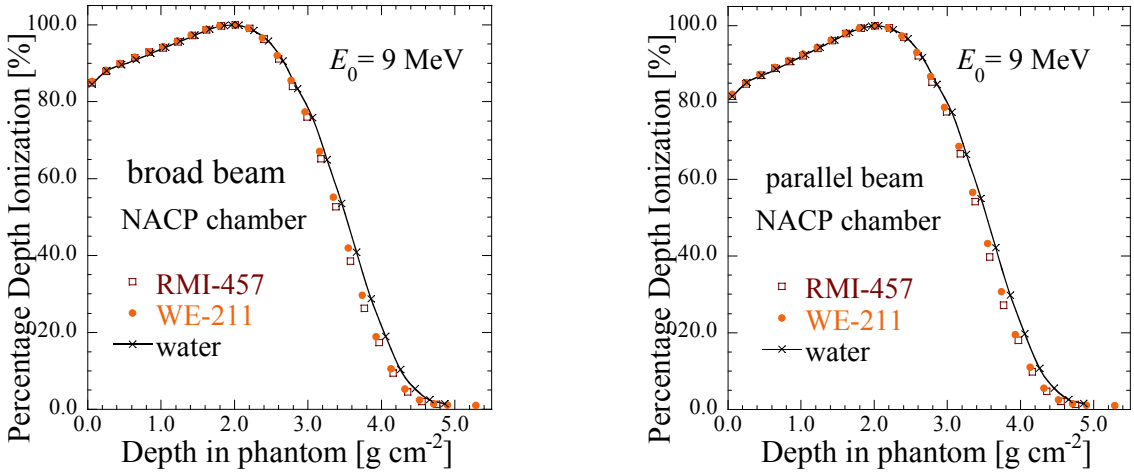

Figure 3. PDI curves in two plastic phantoms at E_0 of 9MeV with NACP chamber. (a) without beam divergence correction (broad beam), (b) with correction (parallel beam).

Figure 3(a) and (b) are PDD curves in each water and plastic phantoms at E_0 of 9 MeV without (a) and with (b) beam divergence correction with effective SSD, respectively (i.e., (a) is in broad beam, (b) is in parallel beam). These data are measured with NACP chamber. There are no differences between parallel beam and broad beam, and differences between PDD in water and that in plastic phantom were still remaining.

Table 2 shows $(R_{50})_{w,m}$ as depth-scaling factor obtained from the measured PDI curves in two plastic phantoms. Table 2 also shows results just for RMI-457 reported from Nisbet and Thwaites[10]. On their report, depth-scaling factors were measured with NACP chamber and ABB Dynaray CH20 linear accelerator. Most of the measurement condition and apparatus between this study and reported from Nisbet are consistent. And our results are also similar with their results.

Figure 4 shows a $(R_{50})_{w,m}$ from Monte Carlo calculation coded by DOSxyznrc. These results are different from c_{pl} from z_{av} ratio by 0.5% higher.

To summarize, several depth-scaling factors including this study are listed in Table 3. Results from measurements were calculated as the ratio of half-value depth in water to that in phantom. Our measured depth scaling factors were not identical with Monte Carlo simulation derived c_{pl} value by 2%. Through this study, depth scaling factors were no quiet difference between measurements with Markus type and those with NACP. And also, the results were not affected whether RMI-457 or WE-211 was used.

Table 2. Comparison of measured depth-scaling factors in this study and that from Nisbet[10].

	Chamber	RMI-457*3	WE-211*3
This study	Markus*1	0.979	0.976
		0.984	0.980
	NACP*1	0.976	0.969
		0.976	0.977
Nisbet[10]	NACP*2	0.977	—
		0.973	—
		0.970	—

*1: upper row is measured at 6 MeV, lower is at 9 MeV
*2: from upper row, $(R_{50})_{w,m}$ at 7, 12 and 17 MeV, respectively
*3: density of RMI-457 and WE-211 are 1.047±0.009 and 1.025±0.009 (g cm^{-3}) in our study. RMI-457 is 1.04±0.01 (g cm^{-3}) from Nisbet.

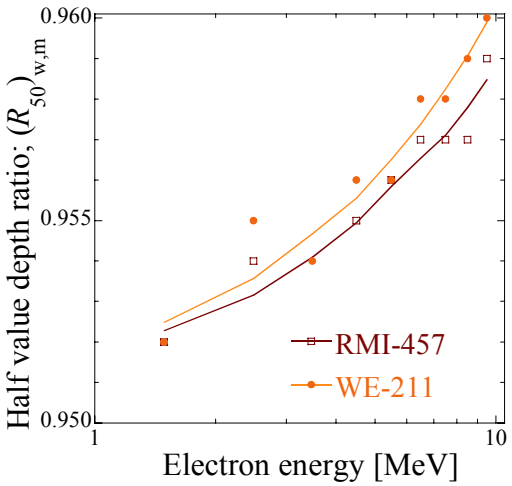

Figure 4. Half value depth ratio; $(R_{50})_{w,m}$ for RMI-457 and WE-211 from DOSxyznrc. It was taken from the ratio of half value depth from PDI or PDD curve between water and plastic phantom.

According to these results, $(R_{50})_{w,m}$ factors were not influenced by changing measurement apparatus.

Table 3. Depth-scaling factors in this study and the others.

		RMI-457	WE-211
c_{pl} from z_{av} simulation	TRS-398 [2]	0.949	—*4
	Saitoh [8]	0.952	0.954
	This Study	0.952	0.954
$(R_{50})_{w,m}$ from measurements*1	Markus*2	0.979	0.976
		0.984	0.980
	NACP*2	0.976	0.969
		0.976	0.977
Nisbet[10] *1,3		0.977	—*4
r_0 (csda ratio)		0.974	0.972

*1: data from ratio of R_{50} in water to that in plastic phantom
*2: upper row is measured at 6 MeV, lower is at 9 MeV
*3: data is measured at 7 MeV
*4: no available data

4. Discussion

To obtain an accurate PDD curve also half value depth of the absorbed dose R_{50} is needed to decide a beam quality factor, calibration depth and water/air restricted mass stopping power ratio. Thus, it is very important to settle the depth-scaling factor precisely. Furthermore, dose calculation in the radiation treatment planning system is based on dose distribution in water. In case of using an anthropomorphic phantom made of water substitute plastic materials used in electron dosimetry, it might make a certain extent of dose error between calculation and measurement.

One of the our current plans is to simulate an electron depth-dose relation with a reconstructed gantry head structure, of course including electron tubes, with Monte Carlo simulation by BEAM code. In this case, each electron has an angular and energy distribution and contaminant photons can be taken into account. Those properties of electron might effect on a depth-dose relation in each phantom.

5. Conclusions

Depth-scaling factor c_{pl} of the several plastic phantoms has been recalculated by EGSnrc ver.4.0, and for the sake of evaluating this factor, measurement in clinical beam and also Monte Carlo dose calculation coded by DOSxyznrc was performed. As a result, the c_{pl} of simulation was not agreed with that of measured. These results suggest that c_{pl} have to be studied more detail so as to carry out precise electron dosimetry in plastic phantoms.

References

1) IAEA: Absorbed Dose Determination in External Beam Radiotherapy, -An international code of practice fordosimetry based on standards of absorbed dose to water-, Technical Reports series No.398, IAEA, Vienna, 2000.
2) AAPM Task Group No.51: AAPM's TG-51 protocol for clinical reference dosimetry of high-energy photon and electron beams. Med Phys., 26(9), 1847-1870, 1999.
3) JSMP: Standard dosimetry for Radiotherapy (JSMP01), Tsusho-Sangyo Kenkyu-sha, Tokyo, 2002.
4) ICRU: Radiation dosimetry. electron beams with energies between 1 and 50 MeV, ICRU Report 35, 1984.
5) AAPM Task Group No.25: Faiz M. Khan, Karen P. Doppke, Kenneth R. Hogstrom et al.: Clinical electron-beam dosimetry: Med. Phys. 18(1), 73-109, 1991.
6) J. M. Fernandez-Varea, P. Andreo and T. Tabata: Detour factors in water and plastic phantom and their use for range and depth scaling in electron-beam dosimetry, Phys. Med. Biol. 41, 1119-1139, 1996.
7) IAEA: The use of plane parallel ionization chamber in high energy electron and photon beams –An international code of practice for dosimetry-, Technical Reports series No.381, IAEA, Vienna, 1997.
8) H. Saitoh, T. Tomaru, T. Fujisaki et al.: A study on properties of water substitute solid phantom using egs code, KEK Proceedings 18, 55-64, 2002.
9) http://physics.nist.gov/PhyRefData/Star/Text/ESTAR.html
10) A. Nisbet and D. I. Thwaites: An evaluation of epoxy resin phantom materials for electron dosimetry, Phys. Med. Biol. 43, 1523-1528, 1998.

DEVELOPMENT OF NUMERICAL CALCULATION PROGRAM OF HIGH ENERGY PHOTON SPECTRA USING RANDOM SAMPLING ALGORITHM

S. Kitou and K. Tabushi

Department of Radiological Technology, Graduate School of Medicine, Nagoya University
1-1-20 Daikou-Minami, Higashi area, Nagoya city, Japan
E-mail: versaplan@hotmail.com

Abstract

Recently, the high precision dose calculating algorithms such as the convolution or the super position algorithm are used for a treatment planning system in external radiotherapy. These algorithms need the data of the energy spectra of the bremsstrahlung X-rays emitted from a linear accelerator to calculate dose distributions in a patient. The energy spectra are generally found by calculating the numerical method such as eigenvalue method or iterative perturbation method, or using Monte Carlo simulation because of difficulty to measure the high energy spectra. In this research, a new numeric calculation method using the random sampling that was able to consider the influence of the errors was designed, and the calculation of the energy spectra of bremsstrahlung X-rays was executed by using this numeric calculation method and the dose distribution also calculated by EGS4. Functioning of the random sampling algorithm was evaluated by comparing input energy spectra and the energy spectra which were calculated by that. Although the spectra reconstructed by random sampling algorithm did not completely agree with the input spectra, the shapes of the spectra and its mode energies agreed well with the input spectra. Therefore the algorithm is available to calculate the high energy photon spectra. However, we should improve the algorithm to calculate the energy spectra more correctly.

1. Introduction

Recently, the high precision dose calculating algorithms such as the convolution or the super position algorithm are used for a treatment planning system in external radiotherapy. These algorithms need the data of the energy spectra of the bremsstrahlung X-rays emitted from a linear accelerator to calculate dose distributions in a patient. It is very difficult to measure the high energy spectra, therefore the energy spectra is generally found by calculating the numerical method such as eigenvalue method[1] or iterative perturbation method[2] using attenuation measurements or Monte Carlo simulation[4)-6)]. Although the method to find the energy spectra by Monte Carlo simulation is examined in a lot of recent papers, it needs a number of input parameters. In case of numerical methods[1)-3)], the number of the input parameters is less than that of Monte Carlo method, but several or a lot of candidates of the energy spectra are usually calculated by those methods because of the influence of errors in measurement and calculation, therefore it is very difficult to specify a true spectrum. Hence, the development of the numeric calculation method that can consider the influence of such errors is needed for calculating the spectrum.

In this research, the new numeric calculation method using the random sampling that was able to consider the influence of the errors was designed, and the energy spectra of bremsstrahlung X-rays were calculated by our numeric method using dose distributions calculated by EGS4. Then the utility was examined.

2. Materials and Methods

2.1 Numerical Integration Method for Solution of High Energy Photon Spectra Function

Dose distributions for bremsstrahlung X-rays are composed of the dose distributions for various monochromatic photons. Therefore, the dose measured at a depth d ($D_{mes}(d)$) is expressed as

$$D_{mes}(d) = \int_0^{E_{\max}} D(d,E) \cdot F(E) \cdot dE \qquad \cdots (1)$$

where D(d,E) is the dose that is obtained for the incident photon energy E at a depth d per unit photon fluence, F(E) is the fluence for the photon energy E.

Equation (1) can be rewritten as

$$D_{mes}(d) = \sum_{i=1}^{n} D(d,E_i) \cdot F(E_i) \cdot dE_i \qquad \cdots (2)$$

where n is the number of partitions of photon energy, E_i is mean energy of i'th energy partition. The function of energy spectra F(Ei) is calculated as the solution that satisfies the equation (2).

2.2 Method of Random Sampling Algorithm

First, the photon energy is divided into n energy partitions. Secondary, random numbers are used to determine the relative photon fluence in each energy partition, and the variety of trial energy spectrum is generated at random. Using the trial spectrum, the dose distribution is calculated by equation (2) and converted into percent depth dose (PDD). Then, the deviation σ of calculated and measured PDDs is evaluated by the following expressions:

$$\sigma_{abs} = \sqrt{\frac{1}{N} \cdot \sum_{p=1}^{N} \left[\left| D_{cal}(p) - D_{eval}(p) \right|^2 \right]} \qquad \cdots (3)$$

or

$$\sigma_{rel} = \sqrt{\frac{1}{N} \cdot \sum_{p=1}^{N} \left[\left| \frac{D_{cal}(p) - D_{eval}(p)}{D_{eval}(p)} \right|^2 \right]}, \qquad \cdots (4)$$

where σ_{abs} is the value to evaluate the absolute difference between calculated and measured PDDs, also σ_{rel} is the value to evaluate the relative difference between them. Only either σ_{abs} or σ_{rel} is used for one research to examine the functioning of random sampling algorithm with each σ. If the deviation σ become smaller than the threshold α (input parameter that decides the errors of the measurement and calculation), the trial spectrum is adopted. These processes are iterated until the number of the adopted trial spectra reaches 100,000 pieces. Finally, the average of the trial spectra (gained the weight) is adopted as the spectrum of incident photon energy.

2.3 Evaluation of Random Sampling Algorithm

Functioning of the random sampling algorithm was evaluated by comparing input energy spectra and the energy spectra reconstructed using dose distributions for various incident photon energies.

First, the dose distributions in water for various incident photon energies were calculated by EGS4. Secondly, the dose distribution for the bremsstrahlung X-ray energy spectra which were referenced previous report data[4] were also calculated by EGS4 and converted into PDD. Then, the bremsstrahlung X-ray energy spectra were reconstructed by the

random sampling algorithm using those dose distributions and those PDDs.

2.4 Condition of EGS4 Calculation

The geometry of the EGS4 calculation is shown in figure 1. The phantom was water, and air (natural temperatures) was the material of the around of the phantom. Cut off energy were 10 keV and 561 keV for the photon and the electron, respectively. Irradiation field with fan beam was square field (field size: 5.0×5.0 cm^2 at the phantom surface), and the distance from source to the surface was 100 cm. Calculation voxel size was set $0.5 \times 0.5 \times 0.5$ cm^3, and the number of cases was $3.0 \sim 8.0 \times 10^8$ to reduce statistical errors less than 1.0 %.

3. Results

The dose distributions in water for various incident photon energies (0.25MeV to 11.0 MeV) are shown in figure 2. The relation between the photon energy spectra reconstructed with σ_{abs} and threshold α for 4MV X-ray is shown in figure 3. Furthermore, input PDD and reconstructed PDDs are shown in figure 4. The spectrum reconstructed with the smaller threshold α is closer to the input spectrum, and the deviation between input PDD and the reconstructed PDD is also smaller. On the other hand, the relation between the spectra reconstructed with σ_{rel} and threshold α for 4MV X-ray is shown in figure 5. Input PDD and reconstructed PDDs are shown in figure 6. The spectra reconstructed with σ_{rel} is more similar to the input spectra than that with σ_{abs}.

Figure 7 shows the relation between the reconstructed spectra and the number of energy partitions. Input PDD and reconstructed PDDs are shown in figure 8. The spectra with a larger number of energy partitions are more irregular. However, the shapes of those spectra are reasonably same to each other, and those PDDs are almost same to each other.

The results of the spectra and the reconstructed PDDs for 10MV X-ray are shown in figures 9 to 14. The results for 10MV X-ray show a similar tendency to the results for 4 MV X-ray. However, the reconstructed spectra for 10MV X-ray more accurately reproduce the input spectrum than that for 4MV X-ray.

4. Discussions

The characteristic of the random sampling algorithm we developed was checked, and parameters that changed the reconstructed spectra were investigated. The shapes of the reconstructed spectra were not almost changed for the number of solutions, if it was not too small. Threshold α made the shape of the reconstructed spectra largely change, therefore we should consider the relation between the measurement errors and threshold α. Also, the number of energy partitions made the shapes of the spectra change. Although the changes of the spectra are not assumed large if the number of energy partitions is not too large or not too small. The reconstructed spectra with σ_{rel} more correctly reproduced the input spectrum than that with σ_{abs}. The convergence of the solution of spectra function was more rapid because the evaluation by σ_{rel} increased the influence of errors at the deeper depth against the evaluation by σ_{abs}.

The spectra calculated by random sampling algorithm did not completely agree with the input spectrum. Though, the shapes of the spectra and its mode energies agreed well with the input spectrum. Therefore it is thought that the algorithm we developed is available to calculate the high energy photon spectra.

5. Conclusions

Random sampling algorithm that we have developed can bring about the good photon energy spectra of X-rays in the radiation therapy. However, we should improve the algorithm to calculate the energy spectra more correctly.

References

1) Rober G. Waggener and Melissa M. Blough, "X-ray spectra estimation using attenuation measurements from 25kVp to 18MV," Med. Phys. **26**, 1269-1278 (1999).
2) P. Francois and A. Catala, "Simulation of x-ray spectral reconstruction from transmission data by direct resolution of the numeric system AF=T," Med. Phys. **20**, 1695-1703 (1993).
3) William H. Hinson and J. Daniel Bourland, "Spectral reconstruction of high energy photon beams for kernel based dose calculations," Med. Phys. **29** (2002).
4) Daryoush Sheikh-Bagheri and D. W. O. Rogers, "Monte Carlo calculation of nine megavoltage photon beam spectra using the BEAM code," Med. Phys. **29**, 391-402 (2002).
5) Michael K. Fix, Harald Keller, and PETER Ruegsegger, "Simple beam models for Monte Carlo poton beam dose calculations in radiotherapy," Med. Phys. **27**, 2739-2747 (2000).
6) Radhe Mohan and Chen Chui, "Energy and angular distributions of photons from medical linear accelerators," Med. Phys. **12**, 592-597 (1985).

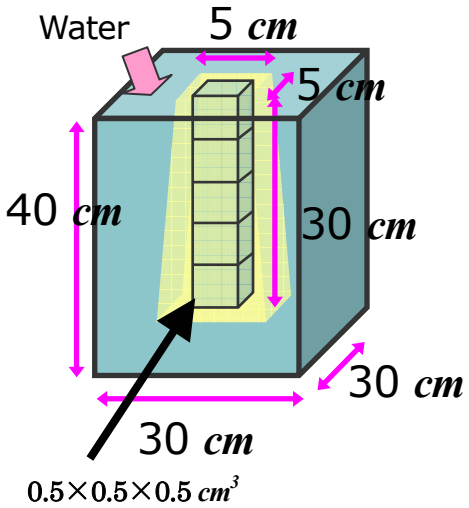

Figure 1. Schematic view of EGS4 geometry to calculate dose distributions in water.

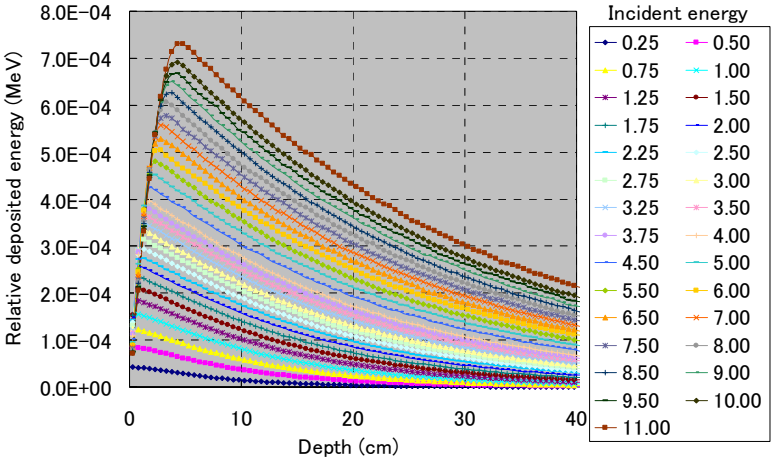

Figure 2. Dose distributions in water for various incident photon energies (0.25MeV to 11.0 MeV) calculated by EGS4.

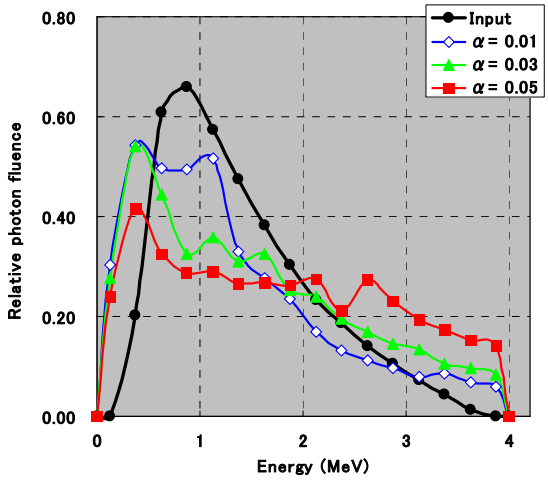

Figure 3. Relation between photon energy spectra reconstructed with σ_{abs} and threshold α for 4MV X-ray.

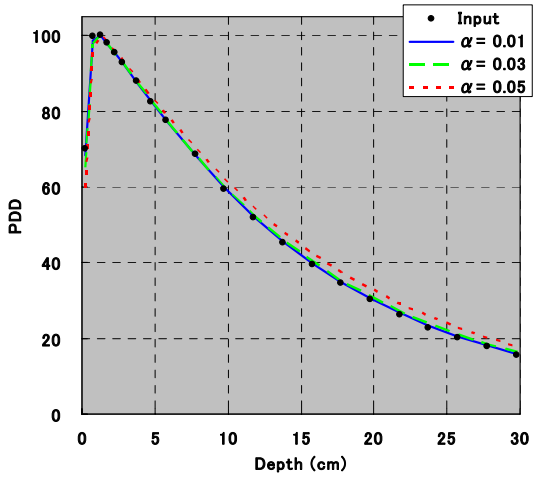

Figure 4. Comparison of input PDD and PDDs reconstructed with σ_{abs} and several thresholds α for 4MV X-ray.

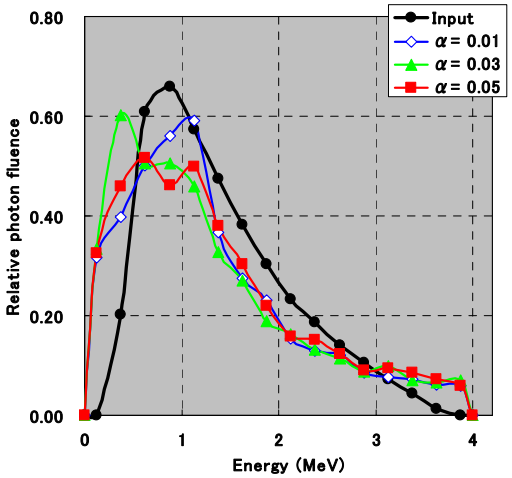

Figure 5. Relation between photon energy spectra reconstructed with σ_{rel} and threshold α for 4MV X-ray.

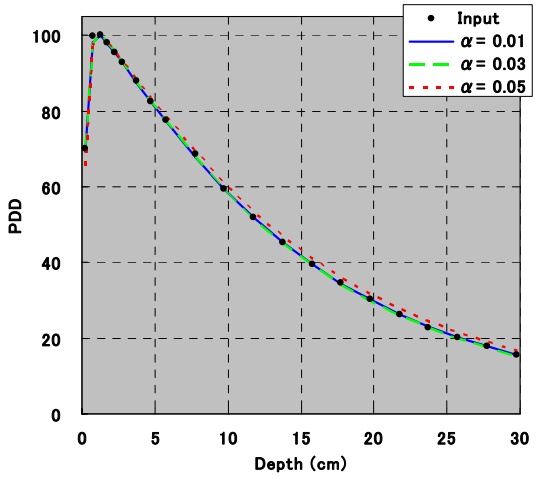

Figure 6. Comparison of input PDD and PDDs reconstructed with σ_{rel} and several thresholds α for 4MV X-ray.

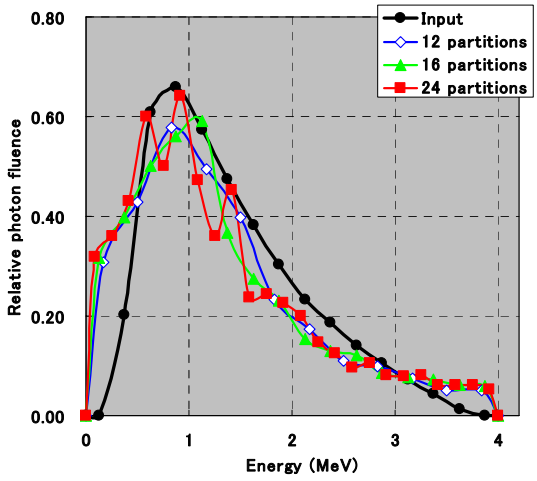

Figure 7. Relation between photon energy spectra reconstructed with σ_{rel} and the number of energy partitions for 4MV X-ray.

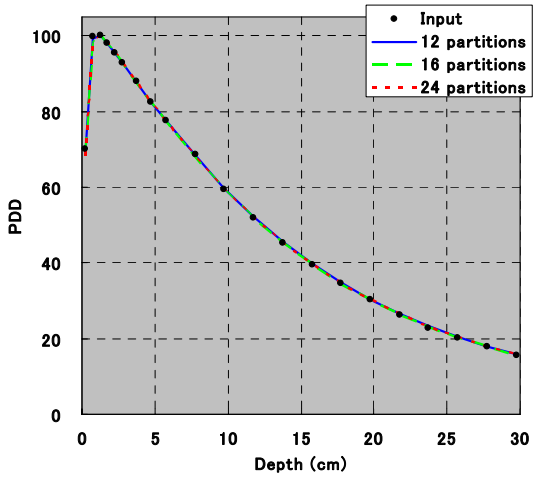

Figure 8. Comparison of input PDD and PDDs reconstructed with σ_{rel} and several the number of energy partitions for 4MV X-ray.

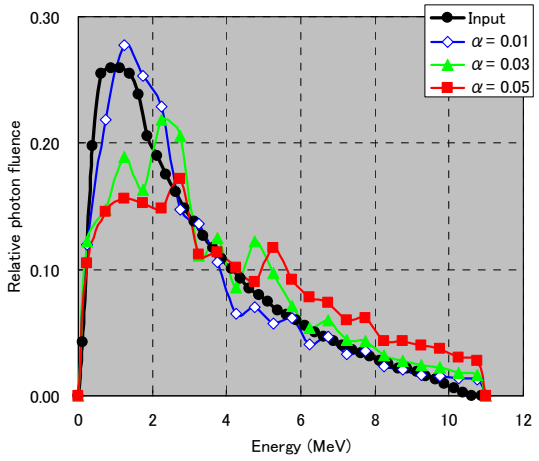

Figure 9. Relation between photon energy spectra reconstructed with σ_{abs} and threshold α for 10MV X-ray.

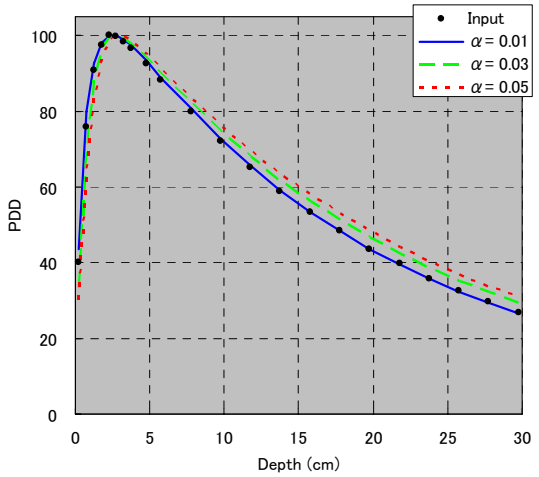

Figure 10. Comparison of input PDD and PDDs reconstructed with σ_{abs} and several thresholds α for 10MV X-ray.

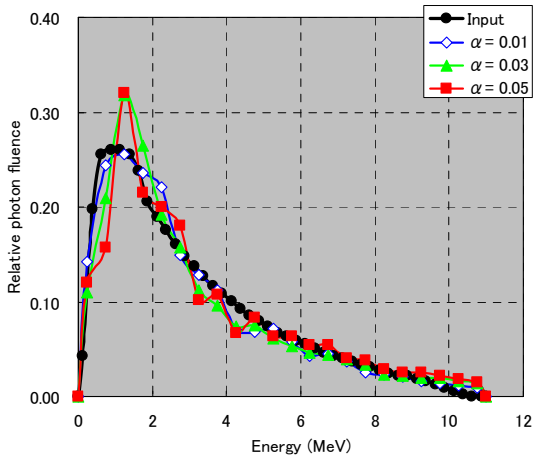

Figure 11. Relation between photon energy spectra reconstructed with σ_{rel} and threshold α for 10MV X-ray.

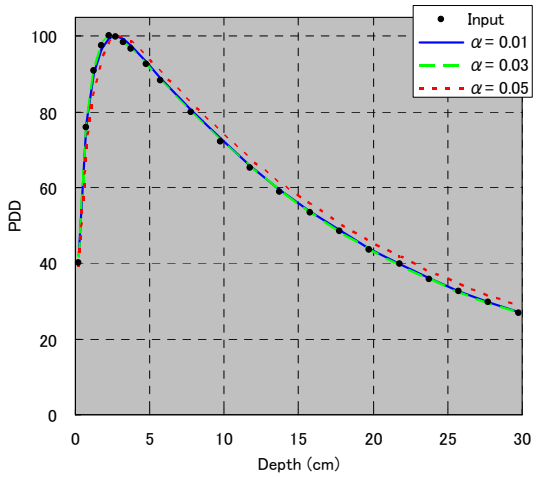

Figure 12. Comparison of input PDD and PDDs reconstructed with σ_{rel} and several thresholds α for 10MV X-ray.

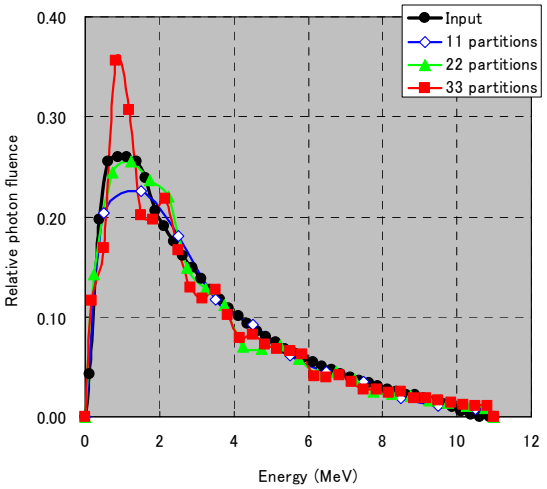

Figure 13. Relation between photon energy spectra reconstructed with σ_{rel} and the number of energy partitions for 10MV X-ray.

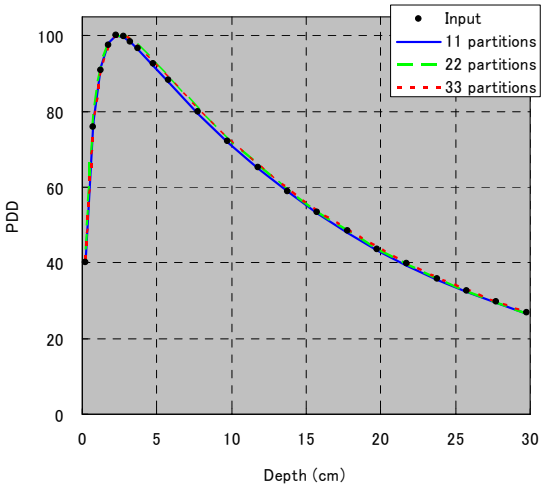

Figure 14. Comparison of input PDD and PDDs reconstructed with σ_{rel} and several the number of energy partitions for 10MV X-ray.

BASAL STUDY OF CT BASED ON CHERENKOV RADIATION USING EGS4

N. Kadoya, K. Tabushi

Department of Radiological Technology, Graduate School of Medicine, Nagoya University

Abstract

We investigated whether we would obtain the CT image based on Cherenkov radiation last year. In this experiment, it was possible to obtain a CT image based on Cherenkov radiation. However, the factors contributing to the exposure on the film are not only Cherenkov radiation, but also the scattered radiation. Consequently we examined the scattered radiation and the relation between absorbed dose to Cherenkov radiation using EGS4. The ratio of the number of the scattered particles passing through the cavity of prisms to the particles from other places is 1 to 2.The total scattered particles can be reduced by improved the CCT collimator. In the simulation of Cherenkov radiation, percent depth dose (PDD) matches the Cherenkov photons normalized to the maximum value.

1. Introduction

The velocity of light in water is less than that of light in vacuum. Therefore it is possible for a charged particle to move at a velocity faster than the speed of light in water. When it does so, a faint radiation is produced from water. It is called Cherenkov radiation. The light propagates away in a cone forward of the place where the interaction took place, as shown in Fig.1.V is the velocity of the particles and n is the refractive index of medium, and θ is Cherenkov angle. Cherenkov light is emitted with in a Cherenkv angle θ, given by

$$\cos\theta = \frac{c/n}{V} = \frac{c}{nV}$$

The maximum emission angle is given by

$$\cos\theta_{\max} = \frac{1}{n}$$

In case of the secondary electron due to Co-60 gamma-rays, the maximum emission angle is 42 degrees in water.

This phenomenon is mostly used in study of engineering and physics. However, it is not very useful in study of medicine. In the experiment carried out before, the distribution of Cherenkov light which was generated by Co-60 gamma-rays in water was similar to that of absorbed dose in water for Co-60 gamma-rays. Therefore we noted the relation of the absorbed dose to Cherenkov light. We investigated whether we would obtain the CT image based on Cherenkov radiation last year. When the Cherenkov light passed the collimator which is set outside the water phantom, the Cherenkov radiation was measured with the film(Figs.2,3). Here, we calls the collimator which collimates Cherernkov radiation a CCT collimator. The CCT collimator was consisted of the thirty prisms; the outer size of the prism was $5\times5mm^2$ and the aperture size was $4\times4mm^2$. The length of the prisms is 4.4 cm and two aluminum boards are attached on and under the collimator. Then as the available turn table was rotated at step of 15 degrees, 24 films were used for the experiment. These were got from 0 to 345 degrees. Then 24 films were read and the image was reconstructed using back projection with Sheep & Logan Filter created by Fortran. The CT image is shown in Fig.4 and the density values are divided into 100 steps with gray scale.

Thus, in this experiment, it was possible to obtain a CT image based on Cherenkov radiation. However, factors contributing to the exposure on the film are not only Cherenkov radiation, but also the scattered radiation. Consequently

we considered the effect of the scattered radiation and the relation between absorbed dose to Cherenkov radiation using EGS4.

2. Materials and Methods

2.1 Energy spectra of the scattered radiation

First, we simulated the energy spectra at the front of the CCT collimator and the back of it for the consideration of the scattered radiation. In this simulation, the energies were 1.17, 1.33MeV (Co-60 gamma-rays) and the cut-off energies for transport calculation of electron (ECUT) and photon (PCUT) were set to 521keV and 1keV, respectively. As shown in Fig.5, source-surface distance is 62.3cm and the irradiation field size is 8.6 x 4.6 cm^2 at same deep as the CCT collimator. Moreover, Fig.6 shows the geometry of the CCT collimator. That is the same as the CCT collimator in the experiment. The incident particles were from 100 million to 200 million.

2.2 Variation of the component of scattered radiation by improved CCT collimator

Second, we evaluated the variation of the component of scattered radiation due to the improved CCT collimator with EGS4. In the simulation, 5 models of the CCT collimator were used. The collimator of model ① is the same as the CCT collimator in the experiment and that of ② is the CCT collimator which is removed the two woods. That of ③ is the CCT collimator replaced the aluminum board with the lead board. That of ④ is the CCT collimator where we double up the lead board. That of ⑤ is the CCT collimator which is the only prisms. We simulated the energy spectra at the only front of the CCT collimator in this simulation.

2.3 Simulation of Cherenkov radiation

The simulation of Cherenkov radiation with EGS4 is very important. As a first step of it, we simulated the Cherenkov photons in the regions that were along the beam axis [1], and the number of the Cherenkov photons was normalized to the maximum value. Moreover, the percent depth dose (PDD) was calculated with EGS4. The two results of the simulation were compared. Fig.7 shows the geometry of the simulations. The size of the region is 0.1 x 0.1 x 0.5 cm^3 and the regions of 60 are sat. In this simulation, the energies were 1.17 and 1.33MeV (Co-60 gamma-rays) and the cut-off energies for transport calculation of electron (ECUT) and photon (PCUT) were set to 512 and 1keV, respectively.
The procedure for simulating the Cherenkov radiation is the following. First, we check whether the particle has the electric charge. If it is so, we check whether the energy of the particles (E(NP)) is above the threshold of Cherenkov radiation. Next, we calculate the Cherenkov angle(θ) using E(NP), and using the well known formula [2] to get the number Nc of Cherenkov photons emitted per path length s in Cherenkov angle(θ)

$$\frac{dN_c}{ds} = 2\pi\ \alpha \int \frac{\sin^2\theta}{\lambda^2} d\lambda$$

Here, in the wavelength band 350-500nm,

$$N_C = 390\sin^2\theta$$

This formula is used in our simulation. It is necessary to modify the AUSGUB subroutine for the simulation of Cherenkov radiation.

3. Results

3.1 Energy spectra of the scattered radiation

Fig.8 shows comparison of energy spectra at the front of the CCT collimator and that at the back of the CCT collimator in the center and edge of the CCT collimator. The width of the energy bin was set to 10keV. The component of

the scattered radiation that is less than 300keV is reduced drastically. The spectrum has the peak at about 100keV.

3.2 Variation of the component of scattered radiation by improved CCT collimator

Fig.9 shows comparisons of the energy spectra based on the model ① , ② , ③ , ④ and ⑤. Longitudinal axis is scattered particles per total incident particles. Horizontal axis is energy. The number of total scattered particles were reduced 11%, 64%, and 66% when the CCT collimator of model ① was changed to that of ②, ③ and ④. On the other hand, the values were increased to 3% when the CCT collimator of model ① was changed to ⑤. Thus, the scattered particles of model of ③ were the smallest in all simulations.

3.3 Simulation of Cherenkov radiation

Figure 10 shows the comparison of PDD with relative Cherenkov photons normalized to the maximum value. The difference between two values is very small with an uncertainty of 3.74 %.

4. Discussion

In the consideration of the scattered radiation, when the number of incident particles is one million, 32 particles affect the film. The intensity of Co-60 was 13.5TBq, and the irradiation time was 30 minutes in the experiment. Therefore, the number of the scattered particles is 1.4×10^{12} and the scattered particles may expose the film in the experiment. It is assumed that the component of the scattered particles is mainly the particles passing through the cavity of prisms. However, the spectrum depended heavily on the material objects set on and under the CCT collimator as the result of the variation of the component of scattered radiation by improved CCT collimator. It follows that the scattered particles from upper and under side of CCT collimator is larger than the number of the scattered particles passing through the cavity of prisms. Moreover, the scattered particles were reduced with the models of ③ and ④ and the spectrum of ③ was the same as ④. We regard the scattered particles in ③ and ④ as the scattered particles passing through the cavity of prisms. The particles passing through the cavity of prisms cannot be reduced. As the result, the ratio of the number of the scattered particles passing through the cavity of prisms to the number of the particles from other places is 1 to 2.That is to say that the total scattered particles can be reduced by improved CCT collimator.

In the simulation of Cherenkov radiation, PDD matches the relative Cherenkov radiation. The greater the number of the charged particles is, the greater the number of Cherenkov photons is. Moreover, the higher the charged particle energy is, the greater the number of Cherenkov photons is. However, we don't know the clear reason.

5. Conclusions

In the experiment run last year, the CT image may involve a certain level of scattered radiation. The ratio of the number of the scattered particles from the cavity of prisms to the number of the particles from other places is 1 to 2.Thus there is the possible to reduce the scattered particles, and the remedial measure is to exchange the aluminum board on and under the CCT collimator to the object with the strong stopping power.

In the simulation of Cherenkov radiation, Cherenkov radiation is also related to the absorbed dose.

References

1) A. Mishev, E. Duverger, L. Makovicka, J. Stamenov, "Modelling and study of the Cherenkov effect" Radiation Physics and Chemistry 61 (2001) 371-373
2) J. V. Jelley, "Cherenkov radiation and it's applications" Pergamon Press(1958) United kingdom Atomic Energy Authority

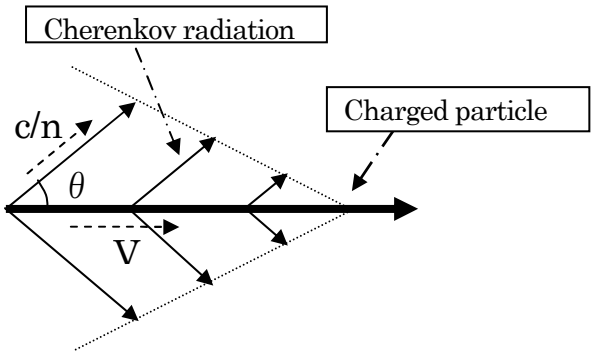

Fig.1 Principle of Cherenkov radiation

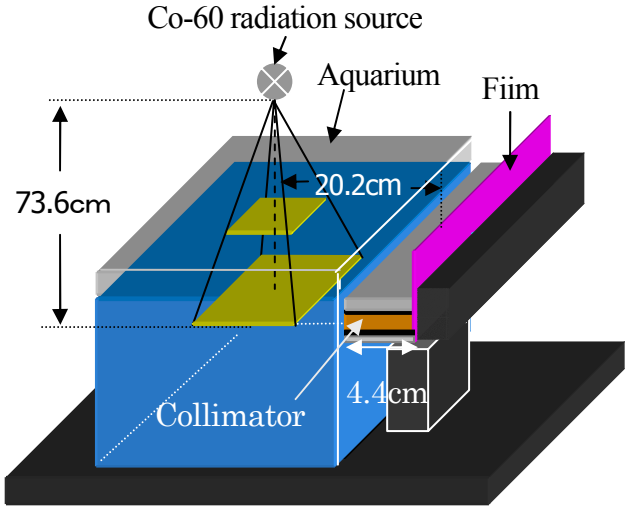

Fig.2 Arrangement of equipment for the experiment.

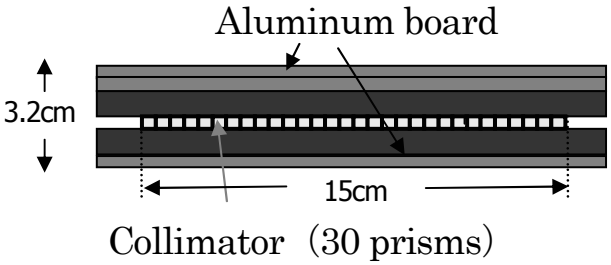

Fig.3 Structure of collimator.
Two aluminum boards are attached on the collimator and one is attached under.

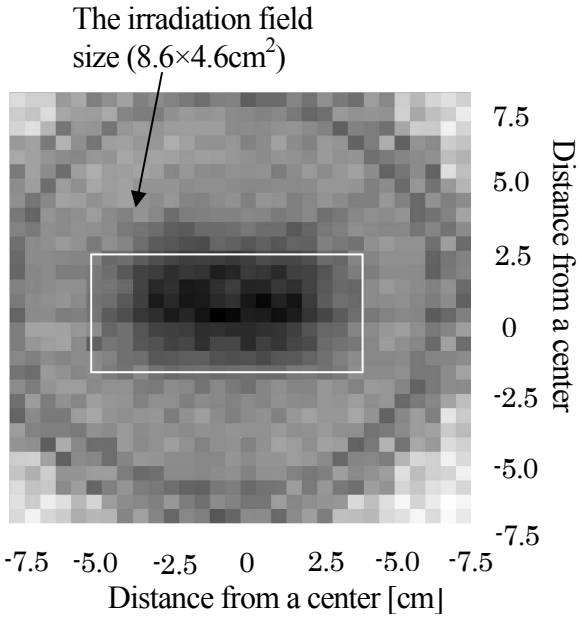

Fig.4 The CT image obtained in the experiment. Density values are divided into 100 steps with gray scale.

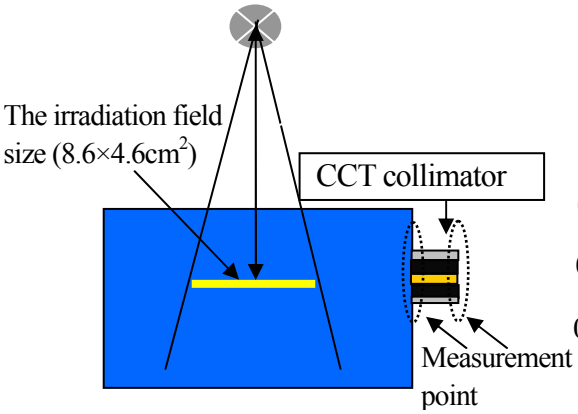

Fig.5 Geometry of simulation

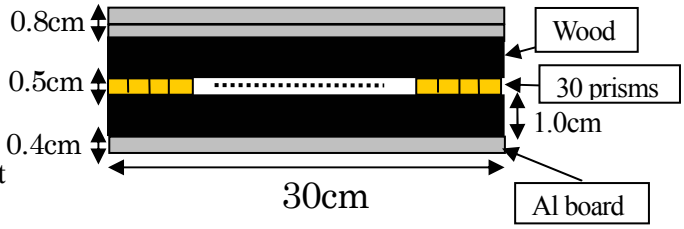

Fig.6 Geometry of CCT collimator

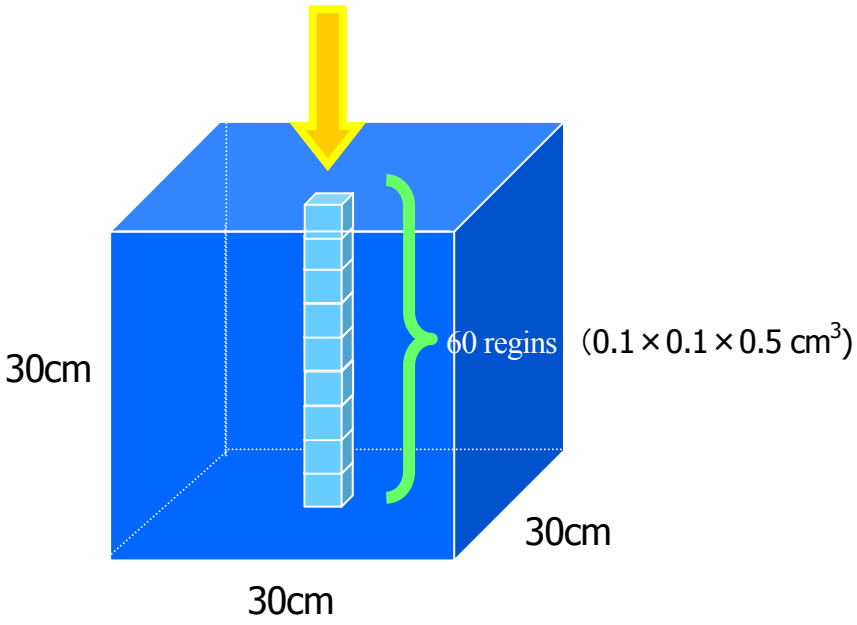

Fig.7 Geometry for Cherenkov simulation

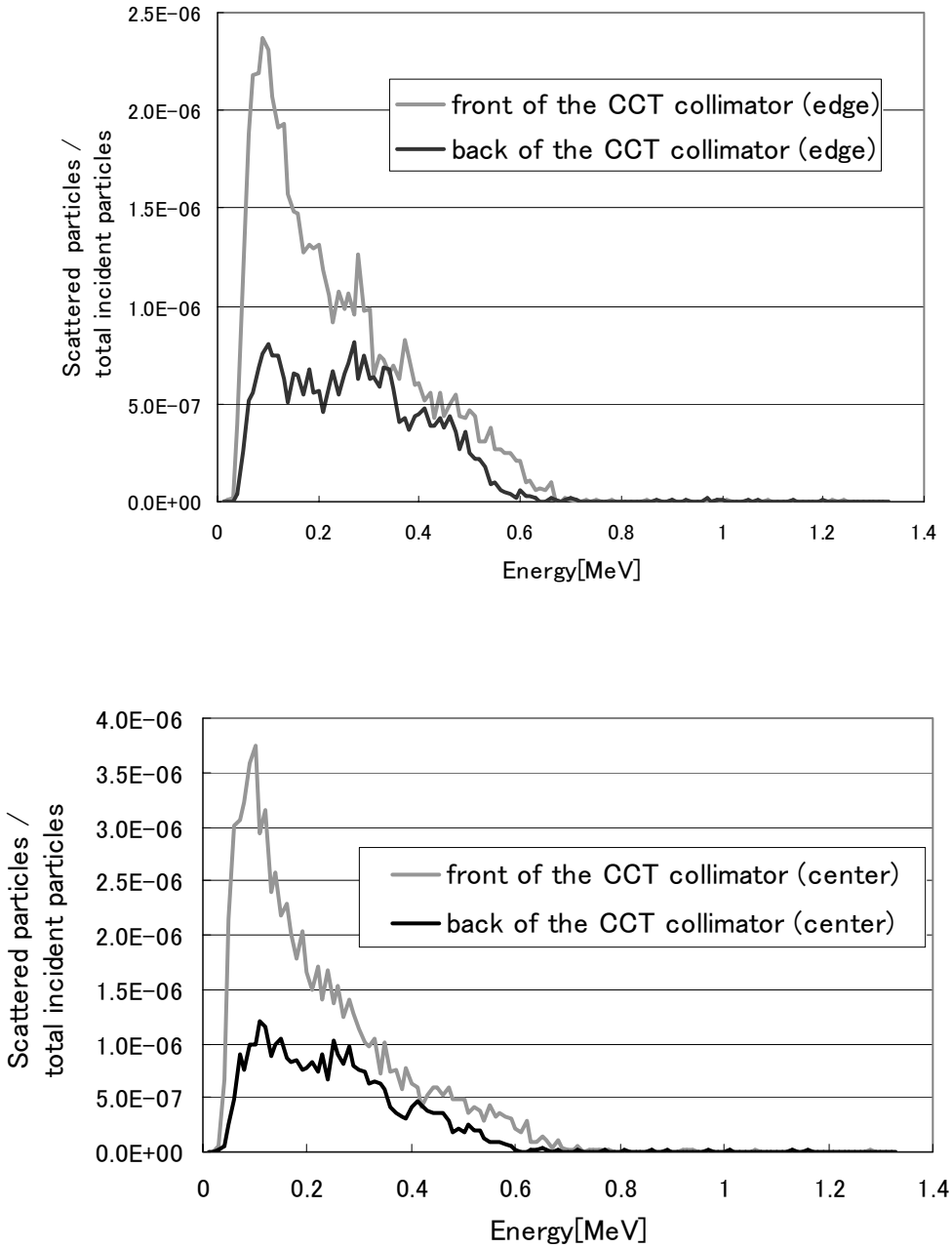

Fig.8 Comparison of energy spectra at the front of CCT collimator and the back of CCT collimator

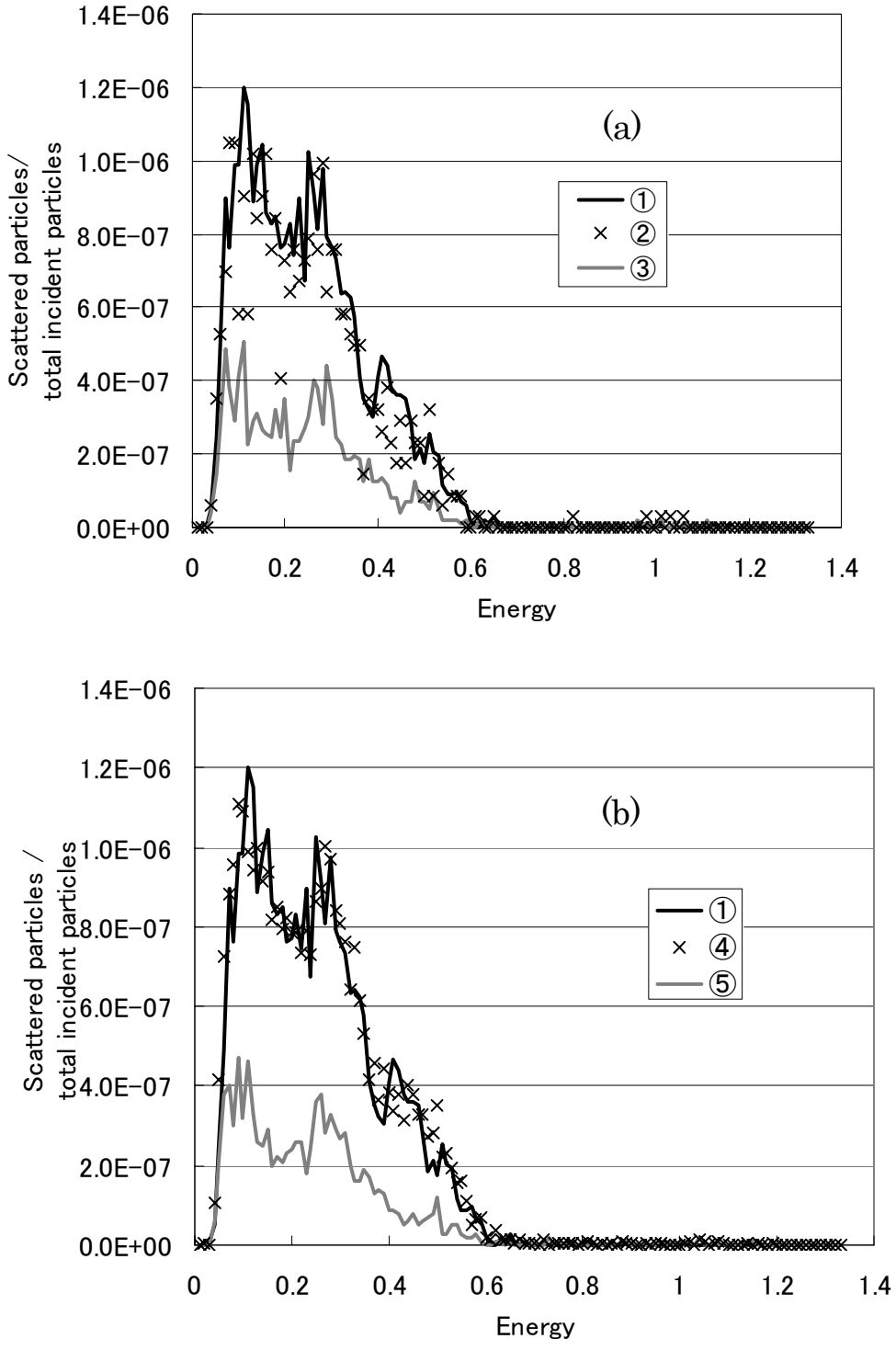

Fig.9 Comparisons of the energy spectra.
The collimator of model ① is the same as the CCT collimator in the experiment and that of ② is the CCT collimator which is removed the two woods. That of ③ is the CCT collimator replaced the aluminum board with the lead board. That of ④ is the CCT collimator where we double up the lead board. That of ⑤ is the CCT collimator which is the only prisms.

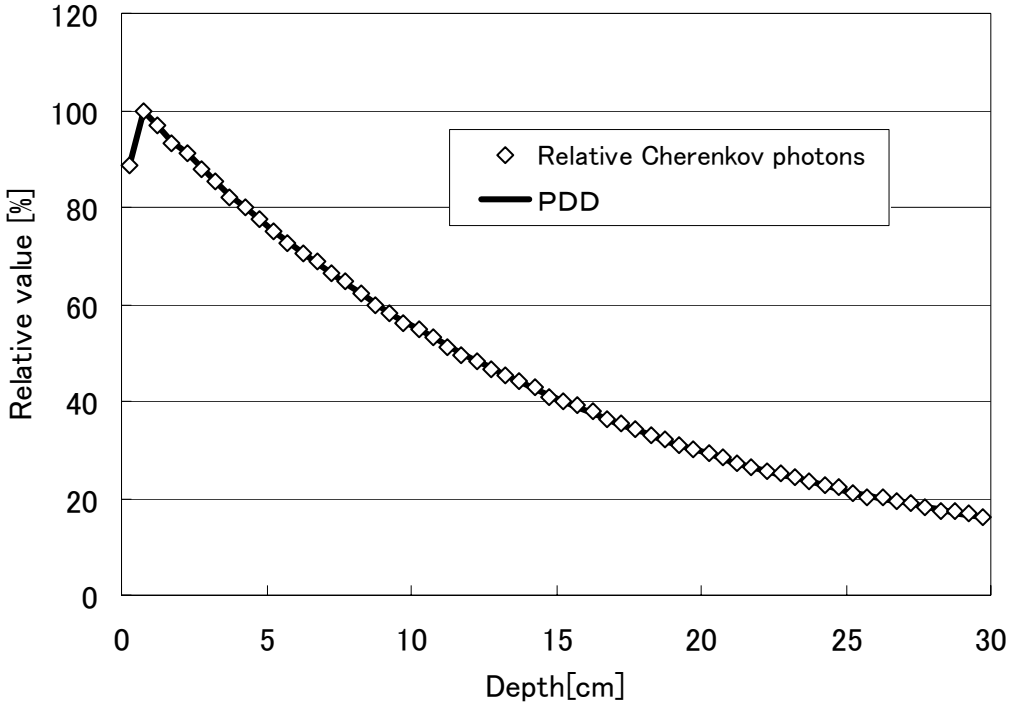

Fig.10 Comparison with the relative Cherenkov photons normalized to the maximum value and the percent depth dose.

Measurement of two-dimensional dose distribution by TL sheets for the clinical radiotherapy

K. Okei[A], H. Shishido[B,C], S. Tsuji[D], T. Tominaga[B], O. Motoda[E], I. Yamamoto,[F] and T. Wada[A]

[A] *Okayama University, Okayama , Japan*
[B] *Hiroshima International University, Hiroshima, Japan*
[C] *Hiroshima Heiwa Clinic, Hiroshima, Japan*
[D] *Kawasaki Medical School, Kurashiki, Japan*
[E] *Okayama Kyokuto Hospital, Okayama , Japan*
[F] *Okayama University of Science , Okayama , Japan*

Abstract

The possibility of the TL sheets to measure the spatial dose distribution of clinical photon beam in the radiotherapy has been examined. TL sheets in the water-equivalent phantom were irradiated to 6 MV photon beams for the stereo-tactic radiotherapy. And EGS simulation code was applied to estimate the absorbed dose distribution in the TL sheets at different depths of water. The preliminary results show the applicability of the TL sheets in the measurements of two-dimensional absorbed dose distribution for the clinical radiotherapy planning.

1 Introduction

A thermoluminescent (TL) sheet and its two dimensional read-out system have been developed to detect high energy hadoronic and electromagnetic cascade showers [1, 2, 3, 4, 5]. These have been applied as a positioning detector of heavy ion beam in accelerator experiments [6] and also in nuclearite search experiments [7]. In the clinical radiotherapy planning, thermoluminescent dosimeter(TLD) is common used to measure absorbed dose at a point, but TL sheets have been only reported in the application to in vivo dosimetry in intracavitary radiotherapy [8].

TL sheet has a wide dynamic range of eight order of magnitude [4], and is able to be handled under the room light because of its insensitivity to visible light, and it is enough thin and flexible to be reformed its size and shape easily. Furthermore its re-usability by means of annealing the irradiated sheet can economize its cost performance.

To examine the applicability of TL sheet as two-dimensional dosimeter for the radiotherapy planning, TL sheets were exposed to 6 MV photon beams of clinical linac and Cyberknife. In this paper, simulation results to estimate the absorbed dose in the TL sheets and preliminary experimental results are presented.

2 EGS simulation

The TL sheet is a mixture of teflon and $BaSO_4$:Eu doped. Figure 1 compares the photon cross sections in the TL sheet and water. Due to the larger atomic number elements, the TL sheet absorbs photon energy much efficiently than water at lower energy. In order to study how the TL sheet absorbs the photon beam energy at different depths of water, Monte Carlo simulations using the EGS code have been performed. In the simulations, Varian 6 MV spectrum tabulated in ref. [9] is used.

Figure 2 shows energy deposited in the target material (the TL sheet or water) of thickness 0.04 cm at different depths of water. The source to surface distance (SSD) was set to be 100 cm. Two

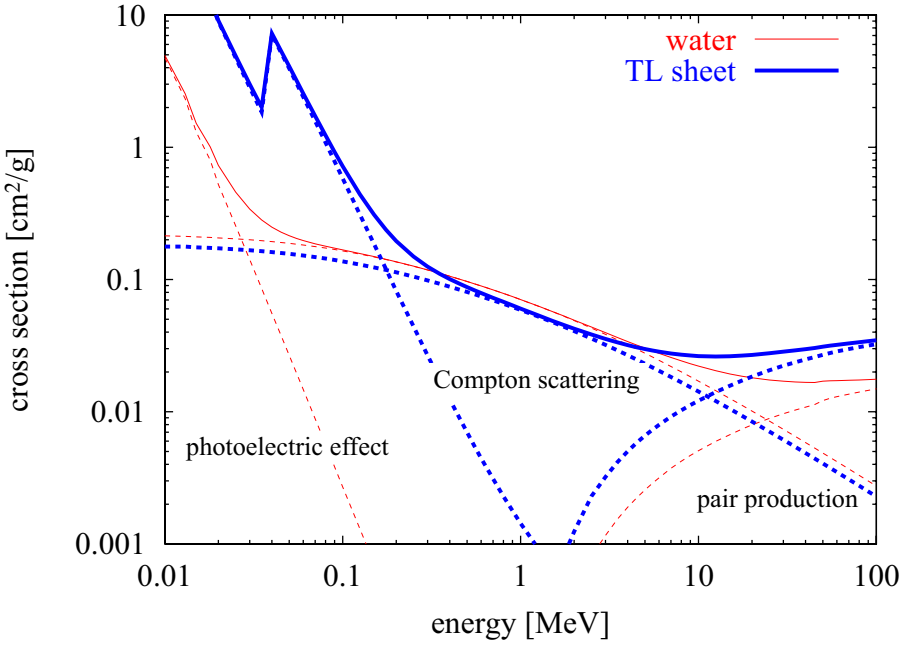

Figure 1: The photon cross sections in the TL sheet (thick blue curve) and water (thin red curve).

different irradiation field size of 4×4 cm^2 and 10×10 cm^2 were simulated. For the 4×4 (10×10) cm^2 field case, the energy deposited D in the central target area of 2×2 (4×4) cm^2 was scored.

To compare the energy deposition per weight, that is, the dose for the TL sheet and water, the ratio $(D_{\mathrm{TL}}/\rho_{\mathrm{TL}})/D_{\mathrm{water}}$ is shown in figure 3. Here, ρ_{TL} is the density of the TL sheet. In the case of the 4×4 cm^2 field size, except at the surface, the difference of the target material is not important since the dose is dominated by electrons produced in water upstream of the scoring region. On the other hand, in the case of 10×10 cm^2 field size, there is some contribution from low-energy scattered photons.

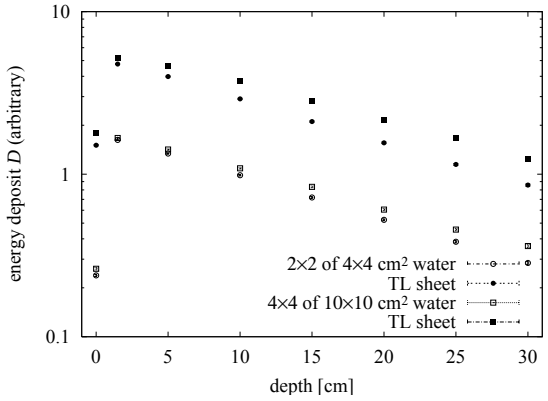

Figure 2: The deposit energy in 0.04 cm of the TL sheet (closed symbols) and water (open symbols) at different depths of water. Circles (squares) show the results of the 4×4 (10×10) cm^2 irradiation field simulations.

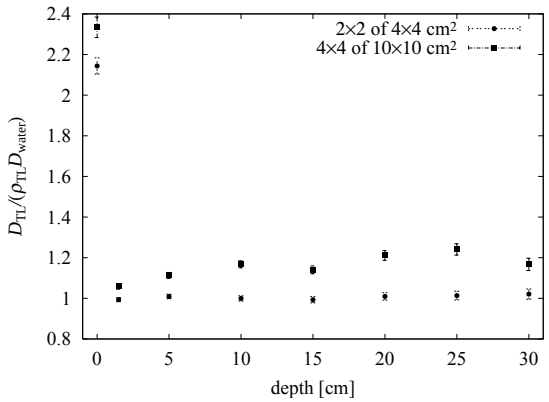

Figure 3: The ratio $(D_{\mathrm{TL}}/\rho_{\mathrm{TL}})/D_{\mathrm{water}}$ at different depths of water. Circles (squares) show the results of the 4×4 (10×10) cm^2 irradiation field simulations.

3 Experiment

The 6 MV photon irradiation experiments were made at Hiroshima International University (Mitsubishi Linac EXL-12SP) and Okayama Kyokuto Hospital (Cyberknife). We readout the irradiated TL sheets at Okayama University of Science.

Figure 4 shows the schematic view of the two dimensional readout system. The TL sheet is heated with an iron which has a temperature controller and TL photons are detected with a cooled CCD camera (SBIG ST-8) which is connected to a PC. The CCD has 1530×1020 pixels and the number of photons is stored at 16 bits per pixel. Conveniently, the whole readout system is portable.

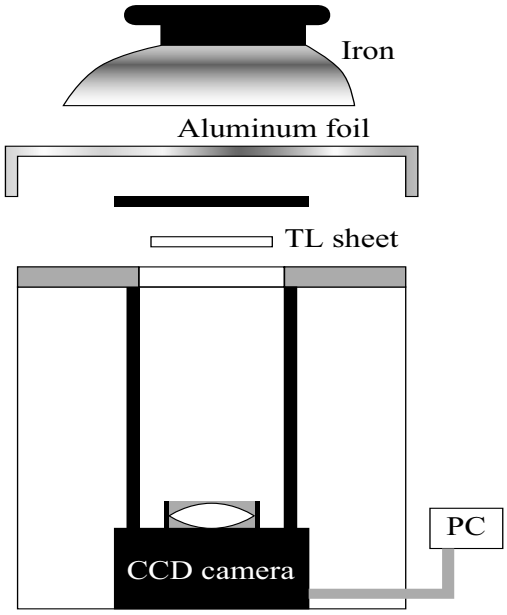

Figure 4: The schematic view of the two dimensional TL readout system.

The greyscale image shown in figure 5 is an example of the TL readout. This TL sheet was uniformly irradiated 50 Gy of photons by Mitsubishi Linac. Note that the image was reduced by 1/5, that is, by dividing into 306×204 square blocks, each having 5×5 pixels and taking the median value. The right panel of figure 5 shows the horizontal TL intensity profile obtained by averaging intensities of central pixels. This data can be regarded as "flat field" and shows the relative sensitivity of the CCD system. The sensitivity difference is only of the order of ten percent within the TL sheet region.

Figure 6 shows another example of the TL readout. The three TL sheets were irradiated, from left to right, 30, 10 and 5 Gy respectively. Figure 7 shows the detected number of TL photons per pixel as a function of dose. These figures demonstrate the linear response of the TL sheet.

Finally, we show the readouts of the TL sheets which were irradiated 30 Gy of Cyberknife beam in figures 8 and 9. From these figures, it can be said that the TL sheet is suitable for measuring the beam profiles or the spatial dose distributions of clinical accelerators.

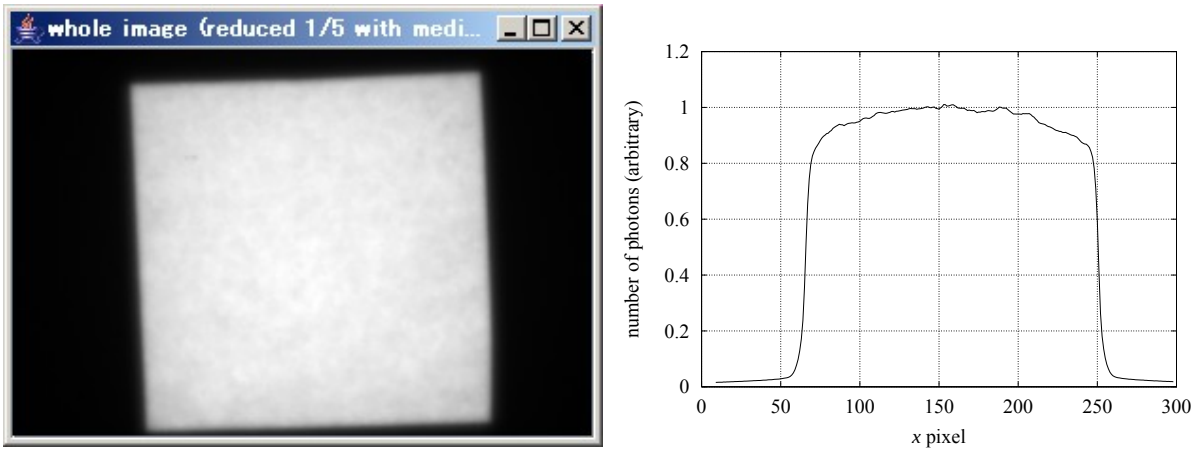

Figure 5: The readout of TL sheet which was uniformly irradiated 50 Gy of photons.

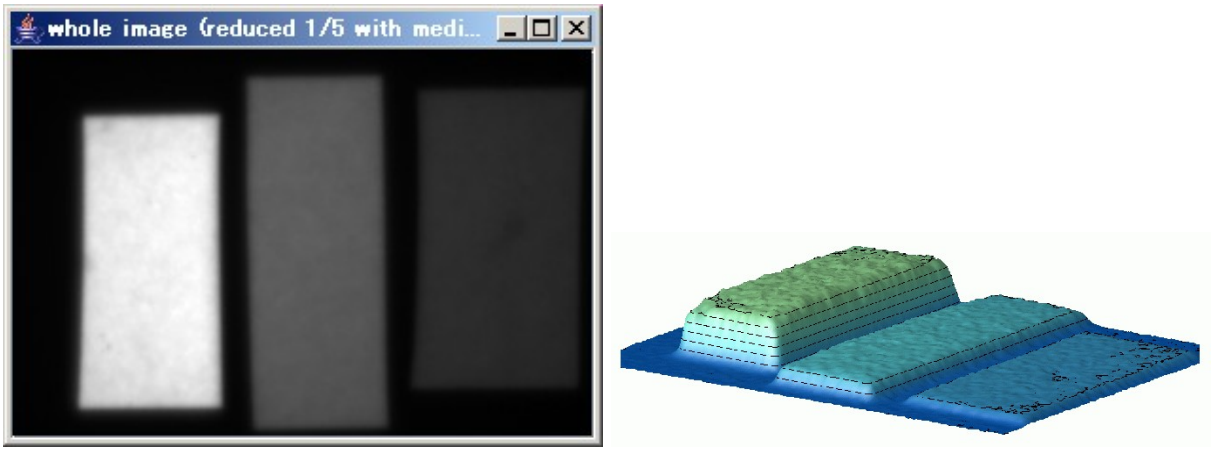

Figure 6: The readout of TL sheets which were irradiated, from left to right, 30, 10 and 5 Gy respectively.

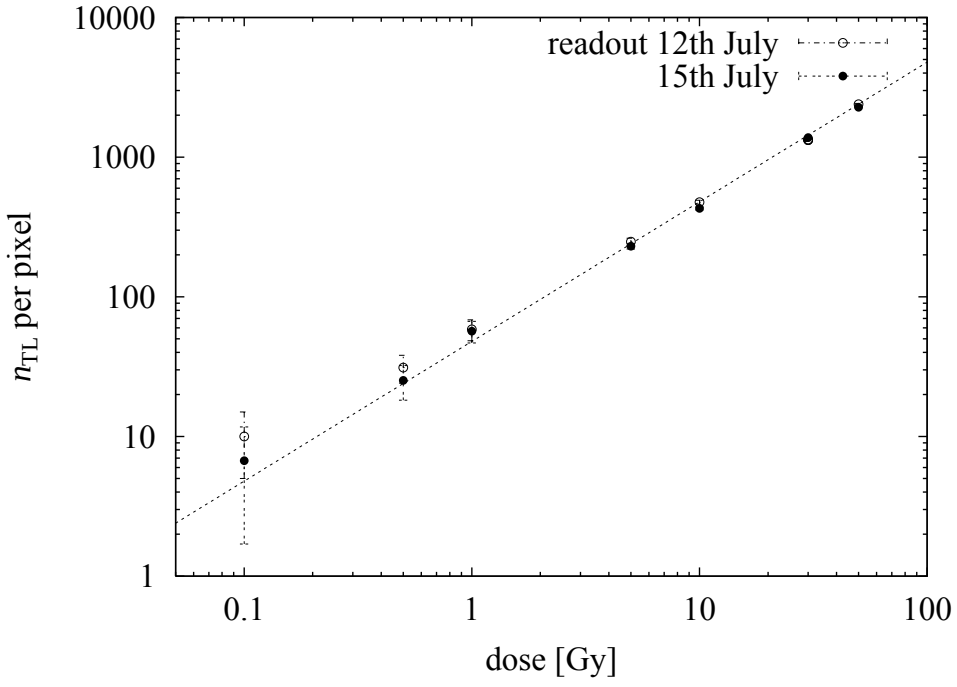

Figure 7: The detected number of TL photons per pixel as a function of dose. The irradiation was made at 11th July 2005 and the readouts were made at 12th (open circles) and 15th (closed circles) July 2005.

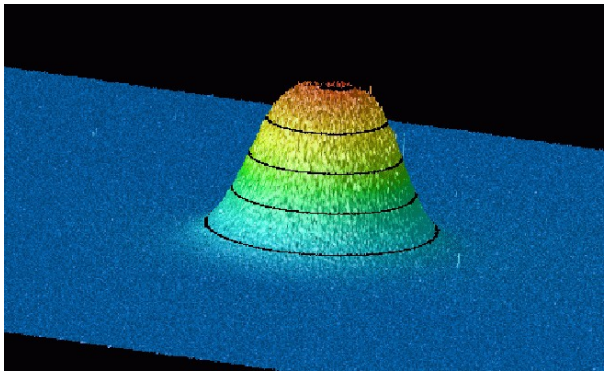

Figure 8: The readout of TL sheet which was directly irradiated Cyberknife beam.

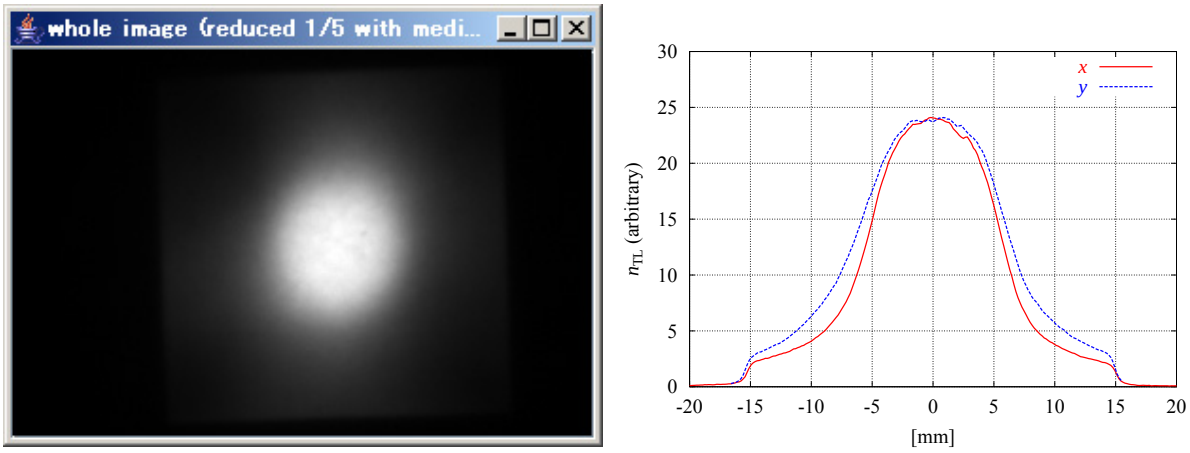

Figure 9: The readout of TL sheet which was irradiated Cyberknife beam using a human head phantom.

4 Conclusion

The applicability of the TL sheet and its two-dimensional read-out system has been examined as two-dimensional dosimeter for the radiotherapy planning. The number of emitted TL photon to absorbed dose has a linear response from at least 0.1 Gy to 50 Gy with enough sensitivity to measure the spatial dose distribution for the stereo-tactic radiotherapy. However more experiments to estimate the fluctuation on the number of emitting TL photon and the effect of fading to absorbed dose, and more simulations to compare with the experimental data , would be necessary to establish the advantages of the TL sheet for the dosimetry of radiotherapy planning.

References

[1] K. Imaeda et al., *Nucl. Instr. and Meth.* A **241**, (1985) pp.567–571

[2] Y. Okamoto et al., *Nucl. Instr. and Meth.* A **243**, (1986) pp.219–224

[3] I. Yamamoto et al., *Nucl. Instr. and Meth.* A **256**, (1987) pp.567–575

[4] T. Wada, N. Takahashi and I. Yamamoto, *Nucl. Instr. and Meth.* A **261**, (1987) pp.368–372

[5] N. Takahashi, *Nucl. Instr. and Meth.* A **270**, (1988) pp.347–353

[6] K. Iwata et al., *2000 Annual Report of the Research Project with Heavy Ions at NIRS-HIMAC*, (2001) 11P036

[7] K. Okei et al., *J. Phys. G: Nucl. Part. Phys.* **27**, (2001) pp.855–865

[8] K. Iwata et al., *Cancer Detection and Prevention* **19**, (1995) pp.367–373

[9] Daryoush Sheikh-Bagheri and D. W. O. Rogers, *Medical Physics* **29**, (2002) pp.391-402

INVESTIGATION OF THE ENERGY CHARACTERISTIC FOR RADIOPHOTOLUMINESCENT GLASS ROD DOSIMETER WITH EGS4

K. Shimomura[1], K. Tabushi[1], S. Kito[1], Y. Shiota[1], N. Kadoya[1], S. Ban[2], and Y. Namito[2]

[1]Nagoya University, 1-1-20 Daikou Minami, Higashiku, Nagoya-shi, Aichi-ken, 461-8673,Japan
[2]KEK, 1-1 Oho, Tsukuba-shi, Ibaraki-ken, 305-0801, Japan
e-mail: k_shimo0812@yahoo.co.jp

Abstract

A Radiophotoluminescent glass rod dosimeter (GRD) system is applied to the dosimetry for broad energy range. When GRD is compared to a thermoluminescent dosimeter (TLD), GRD has the following characteristics: the first is the small variation among elements; the second is to be able to repeat reading; the third is the good repeatability of the read value. However, the energy response is not reported well for the low energy photon, and modified by encasing the element in the tin filter. To carry out the more accurate dosimetry for the low energy photon, the energy response for the monochromatic photon should be investigated. Therefore, we have obtained the more accurate energy response of GRD for the monochromatic photon generated by the synchrotron radiation at Photon Factory (PF), High Energy Accelerator Research Organization. Furthermore, the energy response of GRD was evaluated with EGS4. As the result, the energy response steeply decreased in the region of less than 25keV. Moreover, the dispersion of the read value steeply increased in the region of less than 20keV. The causes of these results have been investigated by calculating the absorbed dose of GRD element using EGS4.

1. Introduction

A radiophotoluminescent (RPL) glass rod dosimeter (GRD) is used to the dosimetry for broad energy range of the radiation. As compared with a thermoluminescent dosimeter for the high energy photon, GRD has the good characteristics such as the energy response, the repeatability of the read value and the dispersion among the GRD elements [1] [2] [3]. However, the energy response is not reported well for the low energy photon. So the energy response is modified by encasing the element in the tin filter. To carry out the more accurate dosimetry for the low energy photon, the energy response for the monochromatic photon should be investigated. There is no public report of that. Therefore, we have obtained the more accurate energy response of GRD for the monochromatic photon generated by the synchrotron radiation at Photon Factory (PF), High Energy Accelerator Research Organization. Furthermore, the energy response of GRD was evaluated with EGS4.

2. Materials and methods

2-1 Radiophotoluminescent glass rod dosimeter system

The GRD system utilizes the principle of RPL, the physical properties of GRD and the readout method of RPL published previously [1][2][3][4]. The size of the GRD element used in this study was 1.2mm in length and 1.5mm in diameter and the readout of GRD was performed with the standard-dose range mode using the GRD reader (FGD-1000

made by ATG). Fig.1 shows the schematic diagram of the standard-dose range mode of the reader. In order to convert of RPL to the air absorbed dose, beforehand, FGD-1000 had been calibrated by the element delivered the air absorbed dose of 6mGy by irradiating the gamma ray of Cs-137. Equation (1) shows the conversion of RPL to the air absorbed dose.

$$D_{air} = \frac{L}{L_{662keV}} \cdot D_{air\ 662keV} \qquad \text{-------(1)}$$

where L is RPL detected by FGD-1000, and D-air is the air absorbed dose.

2-2 Experimental configuration at KEK-PF

Fig.2 shows the experimental configuration at KEK-PF. The beam collimated to $0.98 \times 0.98 cm^2$ was irradiated to the element and the exposure rate of the beam was measured by the free air ionization chamber (FAIC). Five elements were horizontally set to slits of the foam polystyrene with the interval of 2.5cm, and were scanned across the slits to uniformly irradiate to the elements. The elements were irradiated without and within the holder. As shown in Fig.3, the elements were irradiated form the single side and another elements were irradiated from the two opposite sides. Each element was read four times by FGD-1000.

2-3 Calculation of the energy response of GRD using EGS4

To evaluate the energy response of GRD for the low energy photon, the simulation of the absorbed dose distribution in the element was performed by EGS4 with the code to accurately calculate the transport of the low energy particle. Fig.2 shows the geometry of the simulation, too. The simulation by EGS4 was assumed that the incident position of the photon is the surface of the upstream kapton for the irradiation direction of the photon beam and the element is not encased in the holder. The energies of the incident photon were 10 to 80keV and 662keV. The calculation for 662keV was performed to simulate the element used for the calibration of FGD-1000. The calculation was carried out until the fractional standard deviations of the absorbed doses became less than 1%. ECUT and PCUT set to 0.512 and 0.001MeV, respectively. The energy response of GRD for this simulation was theoretically obtained from the absorbed dose of the read area in the element according to equation2.

$$\text{Relative dose rate for air} = \frac{L_{EkeV} / L_{662keV}}{D_{air\ EkeV} / D_{air\ 662keV}} = \frac{D_{glass\ EkeV} / D_{glass\ 662keV}}{D_{air\ EkeV} / D_{air\ 662keV}} \qquad \text{-------(2)}$$

Experiment　　EGS

3. Results and discussions

The energy response obtained from the experiment at KEK is shown in Fig.4. For the range of less than 25keV, the energy response steeply decreased in comparison with the ratio of the mass energy absorption coefficient of the element to that of air. Fig.5 shows the dispersion for the read value applied to the energy response. The dispersion for the single side irradiation was much higher than that for the two opposite side irradiations in the range of less than 20keV.

3-1 Comparison of the energy response obtained by EGS4 and that of measurement

Fig.6 shows the energy responses obtained from the simulation by EGS4 and from the experiment at KEK, and the ratio of both responses. The response calculated by EGS4 is higher than that of the measurement for all energies. The cause of

that is gathered that the real irradiation situation for the calibration element could not be certainly reproduced at the simulation for 662keV. However, the both tendencies are agreement with each other, RPL distribution could indirectly be obtained from the absorbed dose distribution in the element calculated by EGS4.

3-2 Relationship between the RPL distribution and the readout value

Fig.7 shows the dose profile curves obtained from the absorbed dose distribution of the element calculated using EGS4. The profile curves were obtained by irradiating the single side and the two opposite sides to the element as shown in Fig.3. The shadow regions in Fig.7 are the areas irradiated by the ultraviolet laser in order to read RPL. The high absorbed dose at the element surface can be observed in comparison with that at the element center for the energies of less than 25keV. The energy response could be demonstrated by the decrease of the ratio of the read dose to the total dose for the energies of less than 25keV. Because the set position of the element on the reader is not always same, the incident position of the ultraviolet laser is not constant, and then, that of the read area is fluctuated. For the energies of less then 25keV, the gradients of the profile curves are very steep. Therefore, the dispersion of the read value might be occurred by the read system.

4. Conclusion

In this study, we could indirectly obtain RPL distribution of GRD element from the absorbed dose distribution of the element calculated by EGS4. Thereby, for the low energy photon, the causes of the energy response and the dispersion of the read value might be the readout method of GRD reader and the steep gradient of RPL distribution in the element. The element is often encased in the tin filter to modify the energy response. Because the characteristics of GRD are varied by the shield effect of the filter for the low energy photon, it should be study in detail.

5. References

1) F. Araki, T. Ikegami, T. Ishidoya, and D. H. Kubo, ‘‘Measurements of Gamma-Knife helmet output factors using a radiophotoluminescent glass rod dosimeter and a diode detector,’’ Med. Phys. **3**0, 1976–1981(2003).
2) M. Tsuda, ‘‘A few remarks on photoluminescence dosimetry with high energy x-rays,’’ Jpn. J. Med. **2**0, 131–139 (2000).
3) F. Araki, N. Moribe, T. Shimonobou, and Y. Yamashita, “Dosimetric properties of radiophotoluminescent glass rod detector in high-energy photon beams from a linear accelerator and Cyber-Knife” Med. Phys. **3**1, 1980–1986(2004).
4) Asahi Techno Glass Corporation, “Explanation material of RPL glass dosimeter: Small element System.” Tokyo. Jpn. 2000.

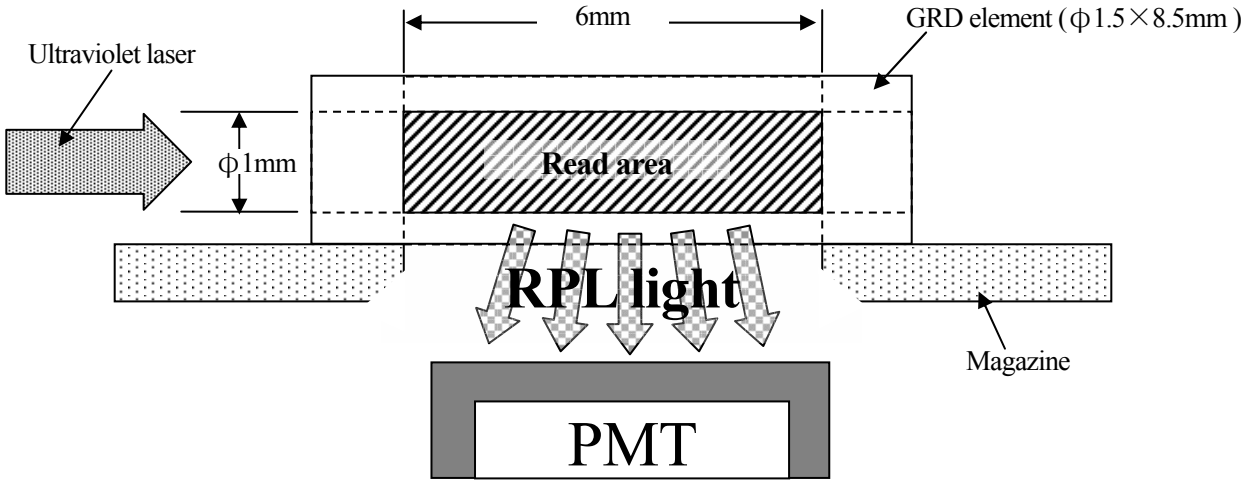

Fig.1 Schematic diagram of the readout principle of GRD

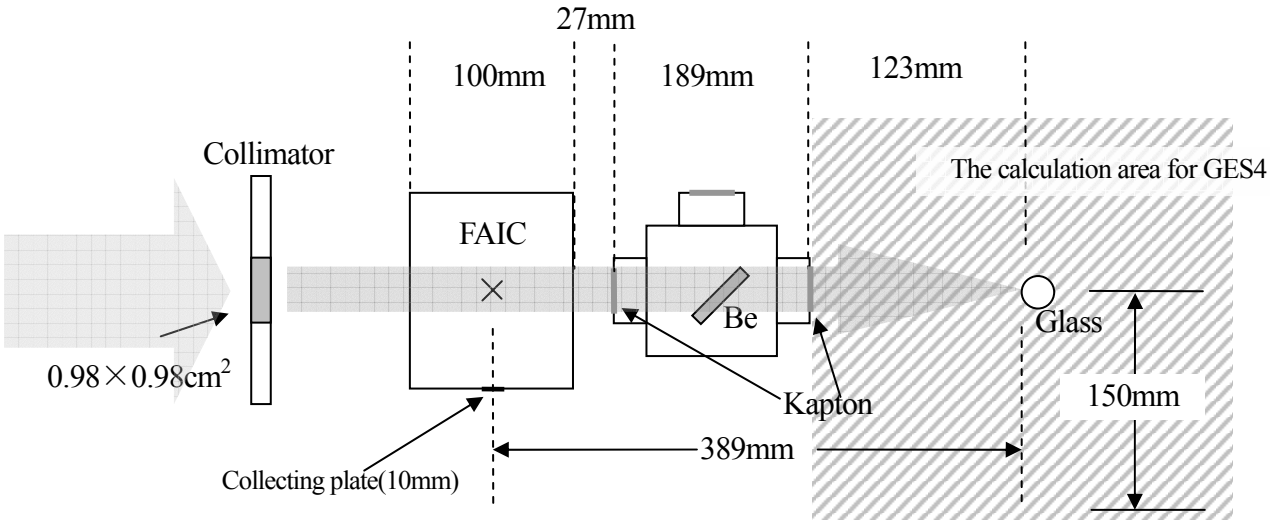

Fig.2 Configuration of experiment

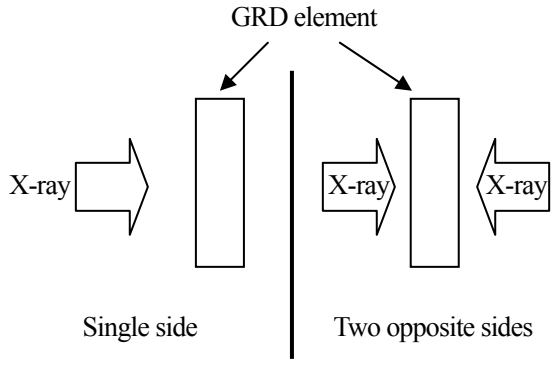

Fig.3 Irradiation direction to GRD element.

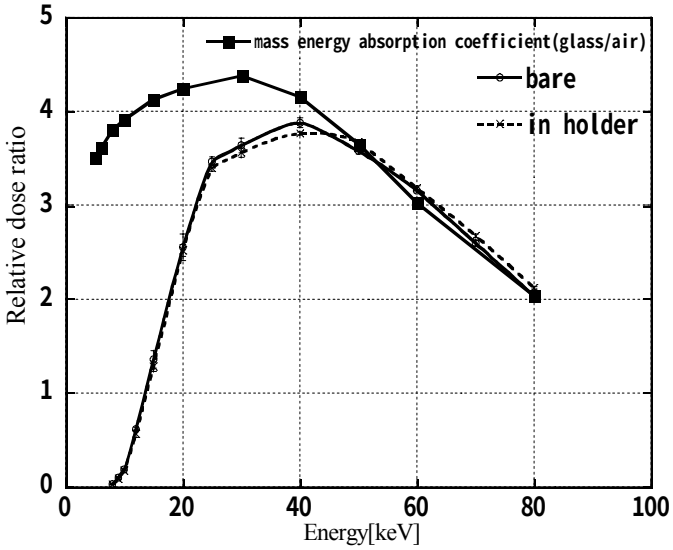

Fig.4 Comparison of the energy response of GRD to the mass energy absorption coefficient ratio.

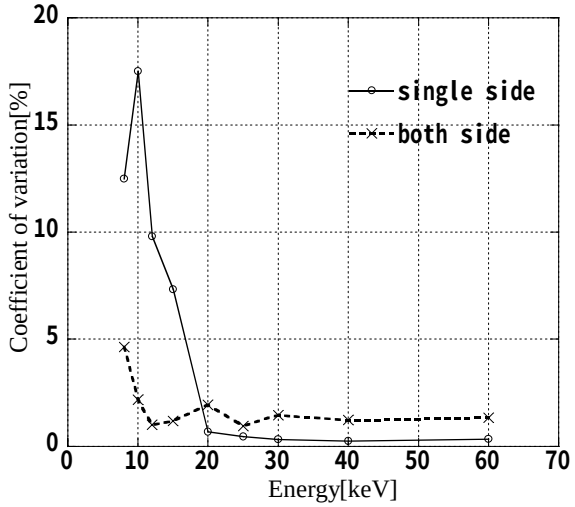

Fig.5 Dispersion of the read value for each GRD elements without the holder.

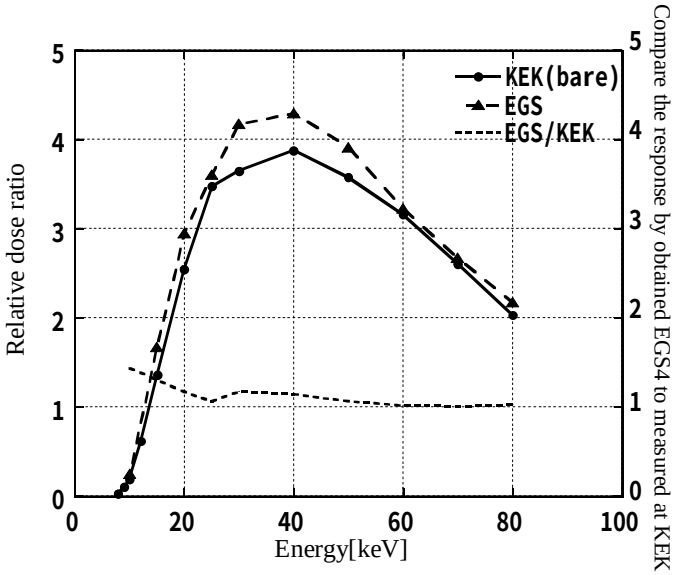

Fig.6 Comparison of the energy response obtained from the simulation by EGS4 and that obtained from the experiment at KEK.

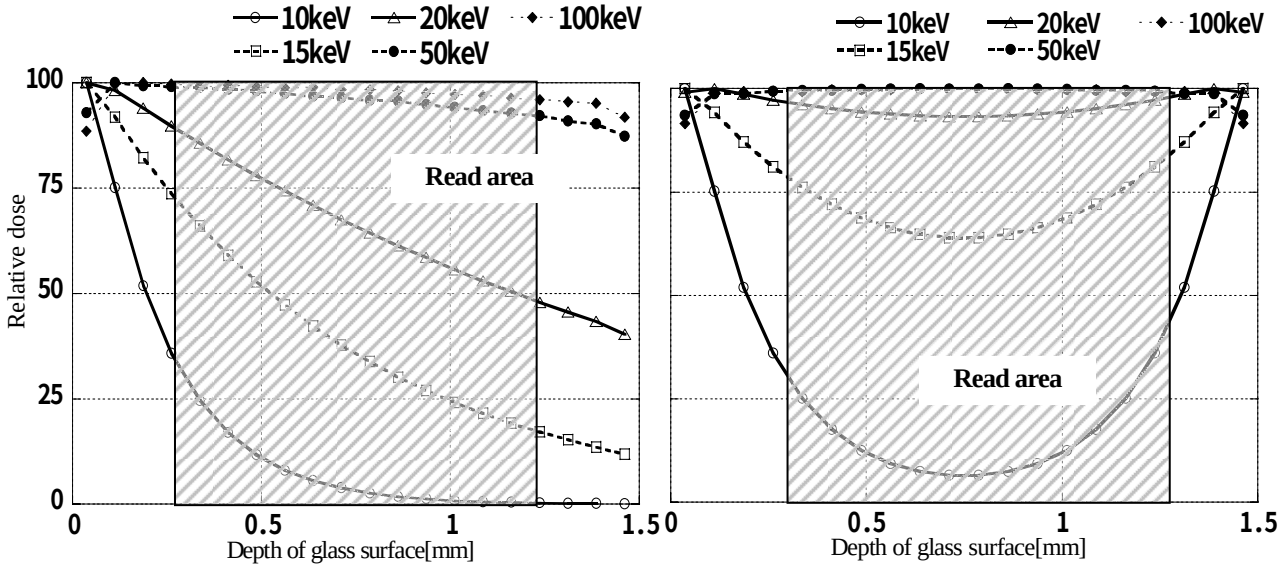

The single side direction

The two opposite side directions

Fig.7 The profile curves in GRD element calculated by EGS4.

DEVELOPMENT OF GAMMA-RAY-SUPPRESSION TYPE OF SMALL-SIZED NEUTRON DETECTOR BASED ON A ^{6}LI-GLASS SCINTILLATOR

T. Matsumoto[1], H. Harano[1], T. Shimoyama[1], A. Uritani[2], K. Kudo[1],

[1]National Metrology Institute of Japan,
National Institute of Advanced Industrial Science and Technology, Tsukuba 305-8568, Japan
[2] School of Engineering, Nagoya University, Nagoya 464-8603, Japan
e-mail: t-matsumoto@aist.go.jp

Abstract

A small-sized thermal neutron detector based on a ^{6}Li-glass scintillator and a plastic optical fiber was developed for measurement of a dose distribution of thermal neutrons in a thermal neutron standard field. A contribution of gamma rays can not be neglected in the neutron measurement with this detector, although the ^{6}Li-glass scintillator can be distinguishable for the neutrons and the gamma rays by difference of each pulse height. Moreover, to reduce an uncertainty of neutron counts caused by the gamma ray background around a discrimination level, we suggested a gamma-ray-suppression type of small-sized thermal neutron detector with a ^{6}Li-glass scintillator, a hollow CsI(Tl) scintillator and plastic optical fibers. The detector can reject signals due to the gamma rays with an anti-coincidence method. In the present paper, we evaluated an ability of a gamma-ray suppression of the detector using the EGS4 electron-photon transport Monte-Carlo code with the PRESTA routine. As the results, the sufficient gamma-ray suppression effect was shown.

1. Introduction

We have a thermal neutron standard field at the National Metrology Institute of Japan (NMIJ), the National Institute of Advanced Industrial Science and Technology (AIST). It is often necessary to determine a dose distribution of thermal neutrons in the standard field. The standard field was established in the outside of graphite pile (190 cm x 190 cm x 230 cm) with a neutron source such as an ^{241}Am-Be or a ^{252}Cf [1]. A neutron fluence rate obtained from the standard field has ranges from 50 to 10^{4} $cm^{-2}s^{-1}$. So far we used an activation method with a gold foil for measurements of the neutron-dose distribution. However, using the activation method, it takes a lot of hours for precise measurement of the neutron-dose distribution in a low intensity field such as the standard field. Last year, we developed a tiny thermal neutron probe [2] composed of a ^{6}LiF neutron converter, a ZnS(Ag) scintillator and a plastic optical fiber for the measurement of the neutron-dose distribution. The small detector with the optical fiber has merits that less disturbance of a neutron field and real-time measurement are possible together [2-4]. However, this type detector is sensitive to both thermal neutrons and gamma rays that are mixed in the thermal neutron standard field [5, 6]. In this work, we developed a small-sized thermal neutron detector based on a ^{6}Li-glass scintillator with a plastic optical fiber, because the ^{6}Li-glass scintillator is distinguishable for the neutrons and the gamma rays by difference of each pulse height and has large detection efficiency for the thermal neutrons. Moreover, to reduce an uncertainty of

neutron counts caused by a gamma-ray background, we suggested a gamma-ray-suppression type of small-sized thermal neutron detector based on a ^{6}Li-glass scintillator. In an ideal case a contribution of the gamma rays is removed from the pulse-height spectrum around the discrimination level. In the present paper, response functions of the gamma rays were calculated about the gamma-ray-suppression type detector by the EGS4 electron-photon transport Monte-Carlo code with the PRESTA routine [7, 8]. We evaluated characteristics for the gamma-ray suppression effect.

2. Design of small-sized thermal neutron detector

2.1. Small-sized thermal neutron detector based on a ^{6}Li-glass scintillator (SLS)

The small-sized thermal neutron detector based on a ^{6}Li-glass scintillator (SLS) is the 1.0-mm diameter by 2.0-mm cylindrical ^{6}Li-glass scintillator mounted on an end surface of a plastic optical fiber of 1.0-mm diameter. A thin aluminum cap covers the scintillator for light shielding. The scintillation light from the glass is detected by a photomultiplier that is connected with another end of the fiber. **Figure** 1 shows the pulse-height spectrum measured by the SLS in the thermal neutron standard field with the ^{241}Am-Be source. The ^{6}Li-glass scintillator detects both thermal neutrons and gamma rays as well known [9]. The peak around 400 ch. is caused by the thermal neutrons and the counts below 150 ch. are caused by the gamma rays in figure 1. This figure indicates that the neutrons and the gamma rays can be distinguished when a discrimination level is set to a valley of the pulse-height spectrum. Then the sensitivity of the SLS for unit neutron fluence was 8.46×10^{-3} cm^{2}. The SLS is useful in the thermal neutron field of the low intensity. Around the discrimination level, the gamma-ray discrimination ability of the ^{6}Li-glass scintillator is however not so good because elements of the neutrons and the gamma rays overlap each other. For more precise measurement of the neutron-dose distribution it is very important to improve the SLS so as to suppress the gamma-ray background.

2.2. Gamma-ray suppression type of small-sized detector (GSS)

Figure 2 shows a schematic drawing of the gamma-ray-suppression type of small-sized thermal neutron detector (GSS). The GSS is a 1.0-mm diameter by 2.0-mm cylindrical ^{6}Li-glass scintillator that is centered in a 3.4-mm outer diameter by 5.0-mm hollow CsI(Tl) scintillator. Because a crystal of cesium iodide is soft and less brittle than a sodium iodide, it is easy to finely process. The CsI(Tl) is also less hygroscopic and is low priced. For these reasons, we adopted the CsI(Tl). A movement of scintillation light between the ^{6}Li-glass and the CsI(Tl) is interrupted by an aluminum foil of a thickness of about 40 μm. Plastic optical fibers are used for transmission of the scintillation light from the ^{6}Li-glass and the CsI(Tl) scintillators. The scintillation light from the CsI(Tl) is collected by summing up the signals from the several fibers on a photomultiplier.

In the GSS, an alpha particle and a triton produced by the interaction of the thermal neutron with a ^{6}Li have ranges in the glass of about 7 and 40 μm, and are stopped in the glass. In contrast, incident gamma-ray photons produce secondary electrons by the interaction with the glass such as the Compton scattering, the photoelectric effect and the electron pair production. Most of the electrons will escape from the glass and will travel to the hollow CsI(Tl) scintillator because the electron has ranges of a millimeter or more [10]. Finally, signals due to the gamma rays are rejected by an anti-coincidence method.

3. EGS4 simulation and results

We evaluated the ability of the gamma-ray suppression of the GSS using the EGS4 electron-photon Monte-Carlo code with the PRESTA (Parameter Reduced Electron-Step Transport Algorithm) routine that was developed to minimize the dependence of the results on the step length in the electron transport simulation [7, 8]. In the calculation, the emission angles of the positron and electron produced by the pair production and a bremsstrahlung photon were sampled using IPRDST and IBRDST options [11-13]. Lower discrimination levels of the pulse-height spectra were set to 100 keV and 200 keV for the ^{6}Li-glass and the CsI(Tl) scintillators, respectively.

The geometry routines were written according to the cylindrical models as shown in **Figure** 3 for the GSS detector assembly. The parallel distribution beam of the gamma rays was assumed to impinge on the vertical and parallel planes for an axis of the GSS detector assembly as shown in figure 3. The sources of incident gamma rays were assumed to be circular and rectangular with the same cross sections as the vertical and parallel planes, respectively. The monoenergitic gamma rays from 1.0 MeV to 4.0 MeV were assumed to generate in the outside of the GSS detector assembly. We did not consider contributions of beta rays and capture gamma rays produced by the interaction between the neutrons and the GSS in this calculation.

Figure 4 shows the calculated pulse height spectra of the ^{6}Li glass scintillator with and without the anti-coincidence method in the GSS. The deposit energy in the glass cannot exceed 1.5 MeV because a small volume of the glass. The peak around 280 keV in the pulse-height spectrum without the anti-coincidence method is caused by the electron pair production because the relative importance of pair production rises with the gamma-ray energy. **Figure** 5 shows the comparison of the efficiencies with and without the anti-coincidence method. These were derived from summing up counts in the calculated pulse-height spectra. Figures 4 and 5 indicate that the ability of the gamma-ray suppression is good sufficiently by the anti-coincidence method above 2.0 MeV. Track length of the secondary electron depends on the gamma-ray energy. Therefore, the probability of the coincident observation with the ^{6}Li-glass and the CsI(Tl) scintillators is high as the gamma-ray energy increase. Although the ability of gamma-ray suppression is not so good below the gamma-ray energy of 1.5 MeV, the deposit energy is small and the gamma rays scarcely affect the pulse-height spectrum around the discrimination level. In the case of gamma irradiation from the parallel plane for the detector axis, the calculated results show the same tendency as that from the vertical plane as shown in figure 5. As these calculated results, the ability of the gamma-ray suppression of the GSS is good sufficiently for the gamma-ray irradiation from the whole direction. Therefore, it is predict that the GSS gives more precise dose distribution of the thermal neutrons than the SLS.

4. Conclusions

We developed a small-sized thermal neutron detector with a ^{6}Li-glass scintillator and a plastic optical fiber for measurement of a neutron-dose distribution in a thermal neutron standard field. The detector based on the ^{6}Li-glass scintillator has large efficiency and is useful in a thermal neutron standard field that has low fluence rate. For more precise measurement of the neutron dose distribution we suggested a gamma-ray-suppression type of small-sized thermal neutron detector that consists of a ^{6}Li-glass scintillator, a hollow CsI(Tl) and plastic optical fibers. The good ability of the gamma-ray suppression and the precise measurement of the dose distribution are expected from results calculated by the EGS4-PRESTA code. Now we have made a prototype of the gamma-ray-suppression-type detector.

References

1) T. Michikawa, *Researches of the Electrotechnical Laboratory*, **No. 746** (1974) (in Japanese).
2) Y. Ito, G. Katano, H. Harano, T. Matsumoto, A. Uritani, K. Kudo, K. Kobayashi, T. Yoshimoto, Y. Sakurai and T. Kobayashi, *Radiat. Prot. Dosim.*, **110**, 619-622 (2004).
3) C. Mori, T. Osada, K. Yanagida, T. Aoyama, A. Uritani, H. Miyahara, Y. Yamane, K. Kobayashi, C. Ichihara and S. Shiroya, *J. Nucl. Sci. Technol.*, **31**, 248-249 (1994).
4) M. Ishikawa, K. Ono, Y. Sakurai, H. Unesaki, A. Uritani, G. Bengua, T. Kobayashi, K. Tanaka and T. Kosako, *Appl. Radiat. Isot.*, **61**, 775-779 (2004).
5) K. Kudo, N. Takeda and A. Fukuda, *IEEE Trans. Nucl. Sci.*, **43**, 1851-1854 (1996).
6) K. Kudo, N. Takeda, S. Koshikawa, H. Toyokawa, H. Ohgaki and M. Matzke, *Nucl. Instr. Methods*, **A476**, 213-217 (2002).
7) W. R. Nelson *et al., SLAC-265, Stanford University*, Dec (1985).
8) A. F. Bielajew and D. W. O. Rogers, *Nucl. Instr. Methods*, **B18**, 165-188 (1987).
9) G. L. Jensen and J. B. Czirr, *Nucl. Instr. Methods,* **205**, 461 (1983).
10) G. F. Knoll, "*Radiation detection and measurement, third edn.*" (New York: Jhon Wiley & Sons, Inc.) (2000)
11) A. F. Bielajew, R. Mohan, and C. S. Chui, *National Research Council of Canada Report PIRS-0203*, (1989).
12) H. W. Koch and J. W. Motz, *Rev. Mod. Phys.*, **31**, 920 - 955 (1959).
13) J. W. Motz, H. A. Olsen, and H. W. Koch, *Rev. Mod. Phys.*, **41**, 581 - 639 (1969).

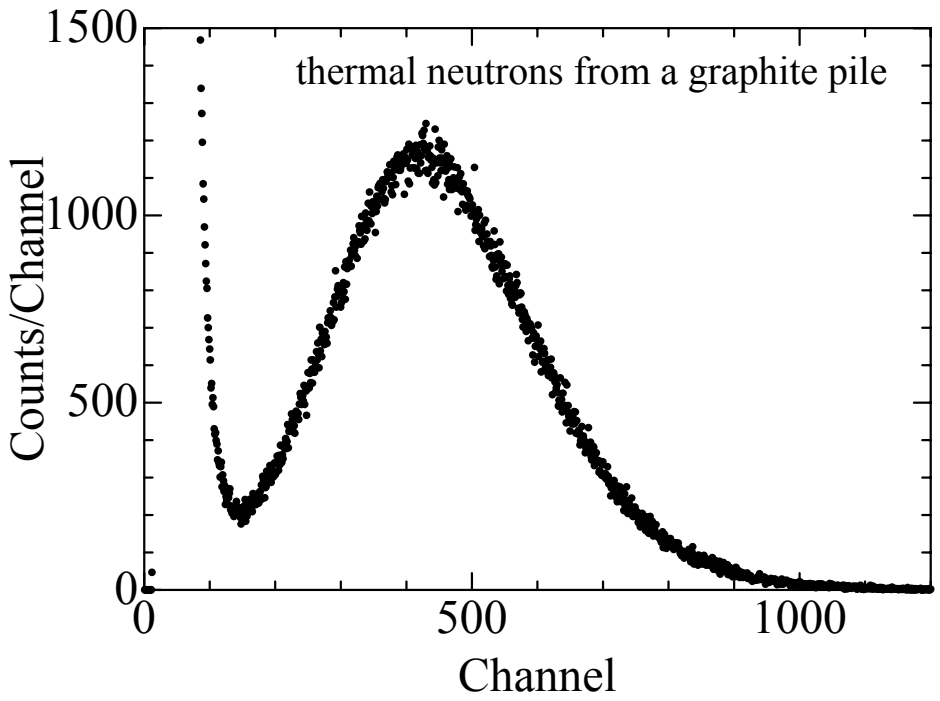

Figure 1. Pulse-height spectrum measured by the SLS in the thermal neutron standard field with the ^{241}Am-Be source.

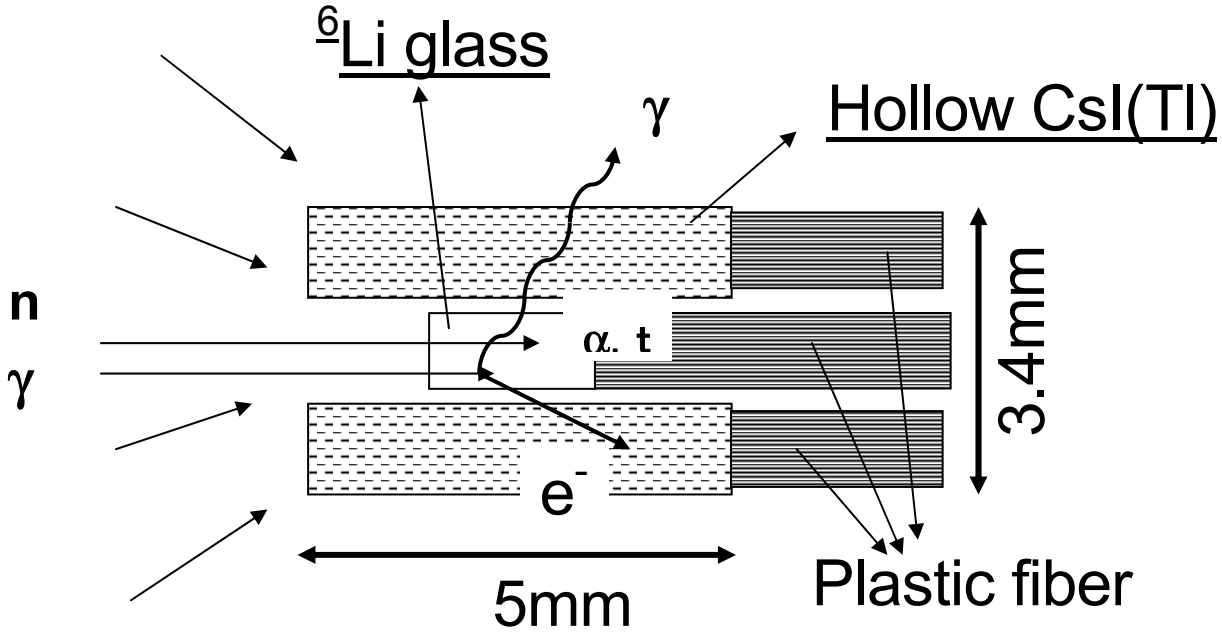

Figure 2. Schematic drawing of the GSS.

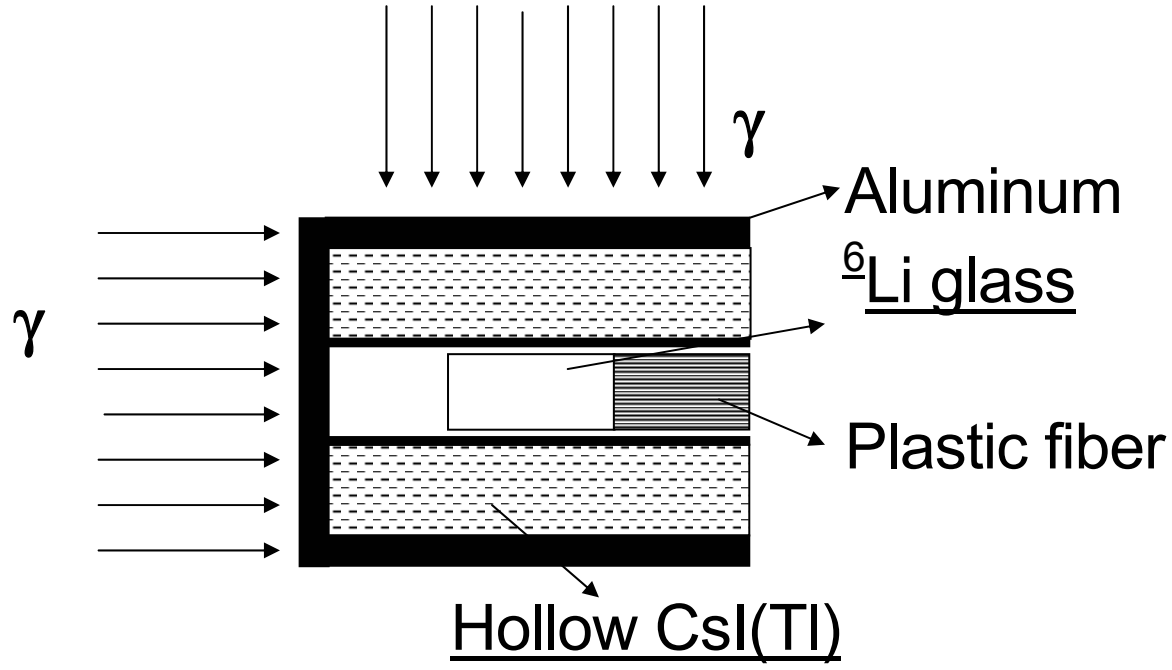

Figure 3. Geometry of the GSS.

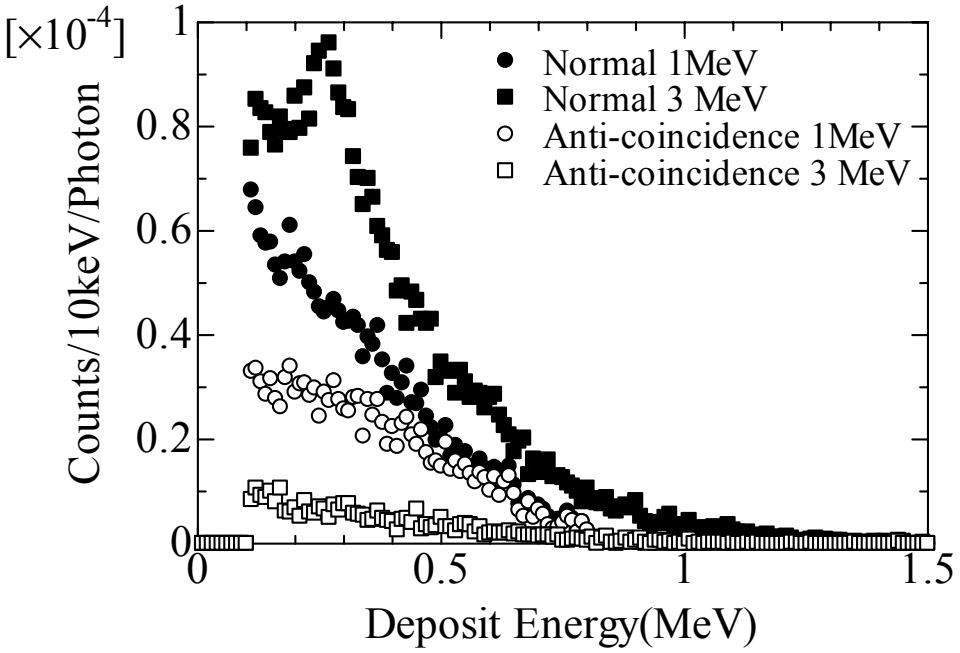

Figure 4. Calculated pulse-height spectra with and without the anti-coincidence method at the gamma-ray energy of 1 MeV and 3 MeV.

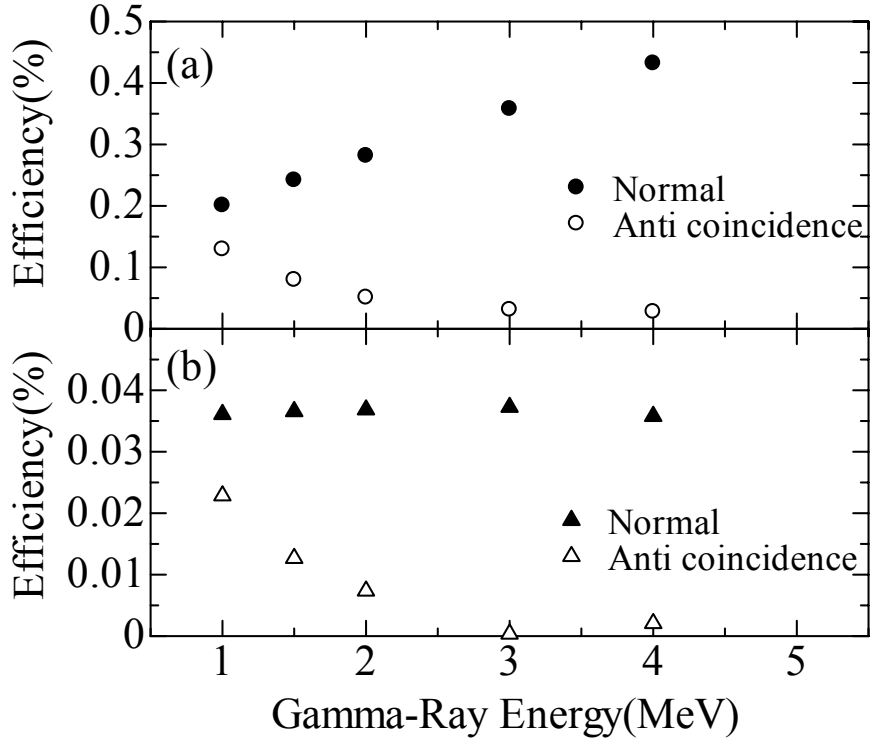

Figure 5. Comparison of efficiencies with and without the anti-coincidence method in the case of gamma-ray irradiation from (a) the vertical plane and (b) parallel plane for the axis of the GSS detector assembly.

DEVELOPMENT OF SINGLE GRIDDED LIQUID XENON IONIZATION DRIFT CHAMBER

T. Shimoyama[1], H. Harano[1], T. Matsumoto[1], M. Miyajima[2]

[1]National Metrology Institute of Japan,
National Institute of Advanced Industrial Science and Technology, Tsukuba 305-8568, Japan
[2] Advanced Research Institute for Science and Engineering, Waseda University, Tokyo 169-8555, Japan
e-mail: tetu-shimoyama@aist.go.jp

Abstract

We have simulated gamma-ray events in single gridded liquid xenon ionization drift chamber by EGS/PRESTA Monte Carlo code to construct data-sets for analyzing the basic performance as ionization chamber from ionization and scintillation signals. The size of effective volume is about 100 cc and a drift length is 42 mm. The collectors are segmented into 20 parallel strips of 2 mm wide with 0.5 mm space. We assumed that the energy resolution is 8.5 % at 1.064 MeV. The comparison of the ionization signals between the experimental result and calculated result were similar shape and the each photo-peak was at the same position. Also the number of scintillation photons observed at two photomultipliers was calculated from the data-sets.

1. Introduction

Double beta decay is one of the rarest phenomena. Especially, a double beta decay that doesn't emit neutrinos is an important decay mode to search for the existence of a massive neutrino [1-3], and to identify the neutrino types. A lot of experimental searches have been undertaken up to now [4-8]. In these experimental searches for the double beta decays, of which the transition energy is normally small and the decay rate is extremely low, only two emitted beta rays are observed at a decay. There exists, however, many background radiation (BG) such as alpha, beta, and gamma-rays from radioactive contamination in detector material, environmental radiation from the earth's crust, cosmic rays, all of which disturb measurements of rare decay events. Therefore, it is desirable to devise almost BG free apparatus at the next generation experiments.

As the first step for going to design the next generation large scale detector, we proposed [9] that a liquid xenon single gridded ionization drift chamber (LXSGIDC) equipped with a system in which the daughter is identified by laser induced fluorescence (LIF) to search for double beta decay events of ^{136}Xe. In the LXSGIDC, by observing the scintillation phenomenon and the ionization phenomenon, the energy of two beta-rays and the vertex position of the decay are determined at every double beta decay events. The total energy deposition is measured as the total charge of liberated electrons. The LXSGIDC enables to determine a two-dimensional vertex position for shooting a decay daughter by the laser light. One is the direction of electron drift under a uniform electric field. The drift time of the electron swarm is a measure to determine the distance from the collector electrode to the vertex position, since the drift velocity of electron swarms is constant under the uniform electric field over about 3 kV/cm in liquid xenon [10]. The other is the direction of a segmented collector electrode. This position is calculated to be a weighted average of collected charges measured by several segments to determine the center of gravity of an electron swarm.

Our purpose of this study is to simulate performance of a very thin and deep liquid xenon ionization chamber (2 x 50 x 50 mm^3) which is the same structure as the proposed one [9] for understanding especially background events due to gamma-rays in liquid xenon.

Here we describe the simulation of the ionization and scintillation signals in the LXSGIDC. In order to calculate signal sizes which we can observe in the LXSGIDC, we construct data-sets composed of the energy deposition due to the gamma-ray of ^{207}Bi simulated with EGS/PRESTA code [11]. We calculated the total of collected charge at the central segment, which width is 10 mm instead of the thin segment of 2 mm, since we have measured the scintillation and ionization signals from 10 mm wide segments. Those calculations are made using the data-sets to simulate the performance and characteristic of the LXSGIDC. We also calculated the number of scintillation photon observed in the photomultiplier tube (PMT) from the data-sets.

2. Structure and Material of Detector for simulation

The cross-sectional drawing of the detector is shown in Fig. 1 (a) and (b). The vessel of LXSGIDC was made OFC. To maximize the sensitive volume of LXSGIDC, the inside of the vessel is cubic shape. The three electrodes are fixed insulated with quartz plates inside the vessel. The upper part of this vessel is connected to a gas handling system. A prop (2.5mm in diameter) for cooling is set at the bottom of this vessel. The sensitive volume of LXSGIDC is 50 x 50 x 42 mm^2. The LXSGIDC consists of a cathode, a shielding grid, a segmented collector electrode (anode). The distance between the cathode and the grid is 40 mm and the distance between the grid and the collector is 2 mm. The grid is gold coated tungsten wire of 0.1 mm in diameter mounted on an invar flame. The effective area of the grid is 50 x 50 mm^2.The cathode plate is made stainless steel. The collectors are segmented into 20 parallel strips of 2 mm wide with 0.5 mm space. These segments were made by vacuum deposition of Cr-Ni-Au on quartz plate (3 mm). To readout the signals due to the collected charges of liberated electrons at segments, each segment is connected an amplifier system through multi-pin feedthroughs. The cathode and the grid are biased through two contact pins which are connected with a high voltage power supplies through each filter circuit, respectively. In this simulation, four segments at the center on the anode are connected together and are used to a collector electrode to collect electron swarms liberated by recoil electrons produced by the gamma-rays for comparison with preliminary experimental results.

Two side-windows for observing scintillation light of the LXSGIDC vessel are quartz plates (5 mm in thickness) and stainless steel flanges with a hole (60 mm in diameter). The indium seals are used in the gap between the vessel and quartz plates and Teflon sheets are placed between the quartz plate and stainless steel flange. Two VUV sensitive PMT are fixed from the quartz window at the position of 5 mm.

The LXSGIDC vessel, two PMT, and cooling system are placed inside an outer cylindrical vessel for thermal shield of the LXSGIDC vessel. The prop of 2.5 mm length was contacted to the cold finger cooled by liquid nitrogen. For example, the temperature of the detector vessel is controlled by adjusting heat flow from outside monitoring its temperature with two silicon diode sensors. The inner vessel was maintained at 165 ± 0.5 K at the preliminary experiments.

3. Geometry for simulation

In the LXSGIDC, there are independently and simultaneously obtained two kinds of signals, fast signals produced by scintillation light and slow signals due to electron-swarms liberated by ionizing particles. It is possible to determine the energy deposition and its two dimensional vertex position in liquid xenon due to the ionizing particle. However, it is not possible to separate events which are due to gamma-rays or two beta-rays emitted at a double beta decay of ^{136}Xe. In this study, we aimed the comparison between the simulation and experimental results in the thin and deep ionization chamber to find out how to reject the events due to background gamma-rays using the ionization signals observed by each segment. Presently, we have a preliminary experimental results obtained with a rather thick and deep

ionization chamber (10 x 50 x 50 mm^3). Those are spectra of ionization and scintillation yields due to gamma-rays from ^{207}Bi. Then, we simulated events due to gamma-rays with slightly simplified experimental arrangements as shown in Fig.1.

The geometry for the present simulation is shown in Fig. 2. In the simulation, the ionization chamber of 10 x 50 x 50 mm^3 is assumed to exist at the central parts in the vessel. However, the gamma-rays from the source interact with liquid xenon in the whole detector, the detector vessel (Cu), the piping (SUS304), electrodes (SUS304 and quartz) and quartz shield Plates. Material of segments is neglected in the simulation. The conversion electrons from the ^{207}Bi source are assumed to be completely absorbed at the cathode plate. The gamma-ray source is fixed at the distance of 14 cm from the cathode surface at the center of piping as shown in Fig. 2, where gaseous xenon of 0.15 MPa is filled in the piping. The density of LXe is 3.06 g/cm^3 and one of gaseous xenon is 5.86 x 10^{-3} g/cm^3. The effective volume of the whole detector is about 100 cm^3. The volume of the thin detector is 25 cm^3. The gamma-rays from the source are 0.570 MeV, 1.064 MeV and 1.770 MeV, and those ratios are 0.977, 0.745 and 0.069, respectively. In the simulation, the whole volume of the detector is divided into 60 x 60 x 55 cells. The energy deposition due to gamma-rays in each cell is simulated by EGS4/PRESTA code in order to make the data sets.

The gamma-rays from the source, which interact with LXe due to Photo-electric effects, Compton effects, and rarely pair creations, produce energetic recoil electrons. The recoil electron of the energy of E emits scintillation photons of n_{Ph} under the absence of an electric field, where $n_{Ph} = f{\cdot}\Omega{\cdot}E/W_s$. The W_s-value (23.7 eV [12]) is the average energy required to produce one scintillation photon in LXe. f is a factor assuming that one-third of the deposited energy is spent to emit scintillation photons under an electric field. The cause of this reduction is due to the luminescence formed by two processes. The first process is the recombination of the free electrons with positive ion. The other process is de-excitations of excited molecules. The contribution of the first process is negligible under high electric field, because the free electrons escape the recombination. Ω is the solid angle subtended by PMT to the center of cell. Assuming that any energy imparted to a cell by the gamma-ray is deposited at the center of the cell, the number of observed photons by two PMT is calculated for every event.

The ionization signals are calculated from the data-sets. Under a uniform electric field, which is sufficiently high to separate the pairs into electrons and ions, an electron swarm produced recoil electron by the gamma-ray is collected with the nearest several segments among the 20 segments. The ionizing electrons given by Q = E/W. W is the W-value (15.6 eV [13]). Assuming that the collection efficiency of electrons at the collector is slightly depend on the drift distance ($N = Q{\cdot}\exp(-x/99)$ [14], where x is the drift distance in cm, Q is initial number of the ionizing electrons), the total number of the collected electrons is calculated for every event.

4. Results and Discussion

Figure 3 shows spectra of the total energy deposition due to the gamma-rays from ^{207}Bi in the 10 x 50 x 50 mm^3 LXe at the center of the whole detector volume. The solid line shows a measured spectrum and the circles show a calculated one. The calculated spectrum is obtained by assuming that the energy resolution is 8.5 % at 1.064 MeV and is inversely proportional to square root of the energy. In each spectrum, two photo-peaks are observed at about 280 channel and about 110 channel. The peak at about 280 channel is due to the photo-peak of the gamma-ray of 1.064 MeV and the peak at about 110 channel is due to the gamma-ray at 0.570 MeV. Above the photo-peak at about 280 channel, there are observed small counts which may be due to the Compton scattering and photo-peak from the gamma-ray of 1.770 MeV. In the calculated spectrum, the position of a photo-peak at about 280 channel is plotted to the same channel of the measured photo-peak. The positions of the both photo-peaks are well coincident to each other and the shapes of the both spectrum seems roughly to be similar. However, the calculation does not clearly reproduce the Compton continuum due to the gamma-rays from ^{207}Bi. It is very hard to compare directly calculated number of counts under the photo-peak to measured number of counts. A ratio of counts under the photo-peak at 0.570 MeV to one at 1.064 MeV is 2.3 in the measurements, but the same ratio is 3.9 in the calculation. On the other hand, a ratio of the measured counts under the photo-peak of 0.570 MeV to the calculated counts under the photo-peak of the same energy is 7.5, but the same of 1.064

MeV is 4.4. The difference seems too large.

The calculated scintillation yields at PMT are shown in Fig. 4. The spectrum (a) and (b) show the number of photons at each PMT. The spectrum (c) shows summed spectrum of the calculated number of photons at two PMT. In the spectrum (a) and (b), the peak at the 800 photons was mainly due to the energy deposition of X-ray from the source. The peaks due to the gamma-rays do not appear in each spectrum. In the spectrum (c), the peak of 800 photon was also mainly due to the X-ray. The broad peak around 4000 photons is due to the gamma-ray at 0.570 MeV and also the board peak is due to the gamma-ray of 1.064 MeV. In consequence, the scintillation yields do not show clear peaks due to the total absorption of gamma-rays event in the calculation, because the emitted number of photons is not so large and also absorption and reflection of VUV photons at the window are completely neglected.

As the conclusion, we need further elaboration of simulation for reproducing the measured energy spectrum in order to understand how to reject background events due to gamma-rays with signals from the segmented electrodes in the LXSGIDC.

References

1) M. Doi, T. Kotani and E. Takasugi, Prog. Th. Phys. Suppl. 83 (1985).
2) M. Doi, T. Kotani, H. Nishiura, K. Okuda and E. Takasugi, Prog. Th. Phys. 66 (1981)1739.
3) M. Doi, T. Kotani, H. Nishiura, K. Okuda and E. Takasugi, Prog. Th. Phys. 66 (1981)1765.
4) H. V. Klapdor-Kleingrothaus, A. Dietz, H. L. Harney and I. V. Krivosheina, Mod. Phys. Lett. A 16 (2001) 2409.
5) K. Fushimi, et al., Phys. Lett. B 53 (2002) 190.
6) P. G. Bizzeti, et al., Nucl. Phys. B (Proc. Suppl.) 10 (2002) 389.
7) A. Alessandrello, et al., Phys. Lett. B 486 (2000) 13.
8) R. Luescher, et al., Phys. lett. B 434 (1998) 407.
9) T. Shimoyama, E. Shibamura, T. Nishikawa, and M. Miyajima, Jpn. J. Appl. Phys., 43(2004)8278.
10) E. Shibamura, et al., Nucl. Instr. and Meth. 131(1975)249.
11) R. Nelson, H. Hirayama, and D. W. O. Rogers, The EGS4 Code System, SLAC-265 (Stanford Linear Accelerator Center, Stanford, CA, 1985).
12) T. Doke and K. K. Masuda, Nucl. Instr. and Meth. A420 (1999) 66.
13) T. Takahashi, et al., Phys. Rev. A 12 (1975) 1771.
14) T. Doke, Portugal Phys. 12(1981)9.

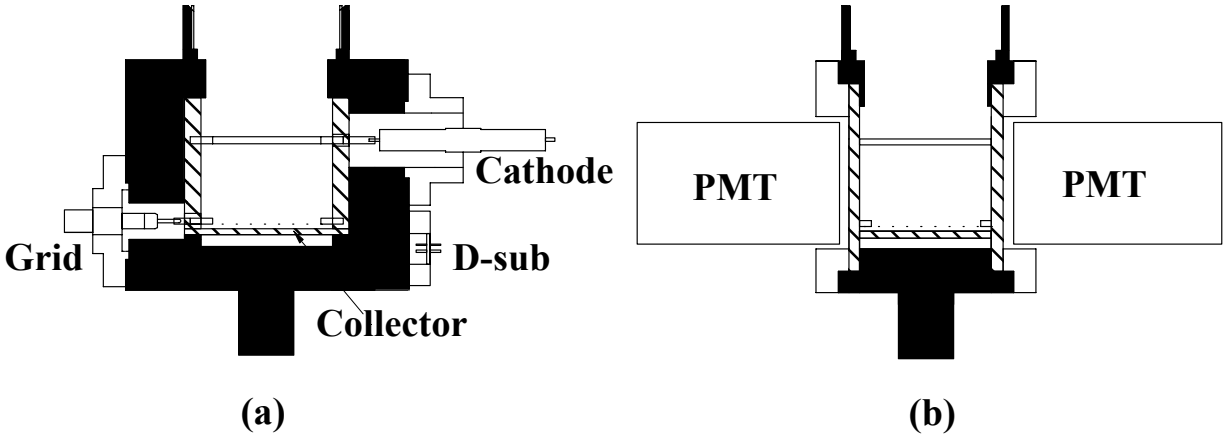

Fig. 1 Cross-sectional view of the LXSGIDC

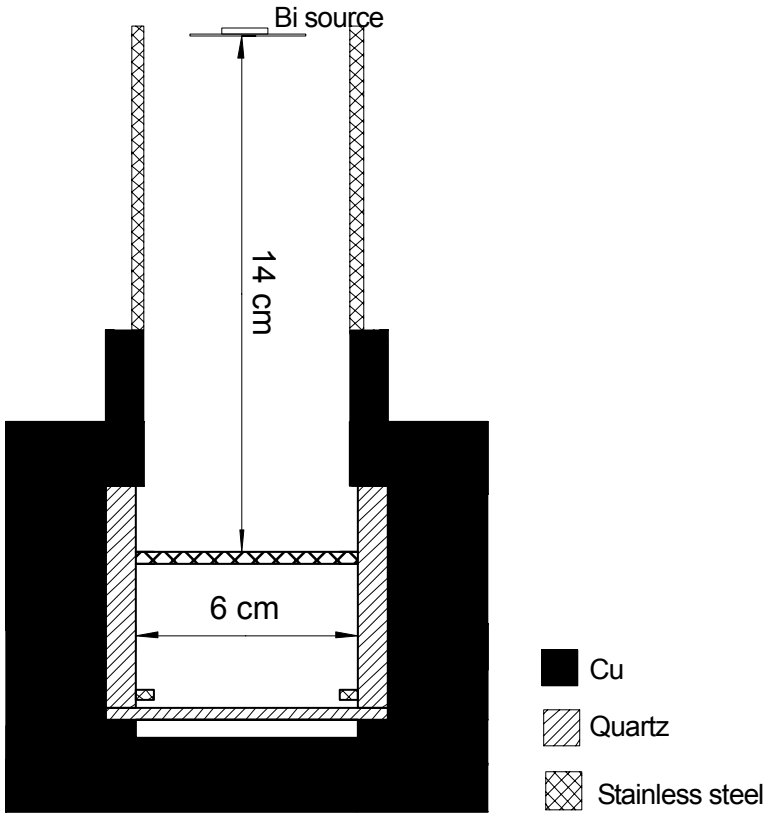

Fig. 2 Calculation model of the LXSGIDC

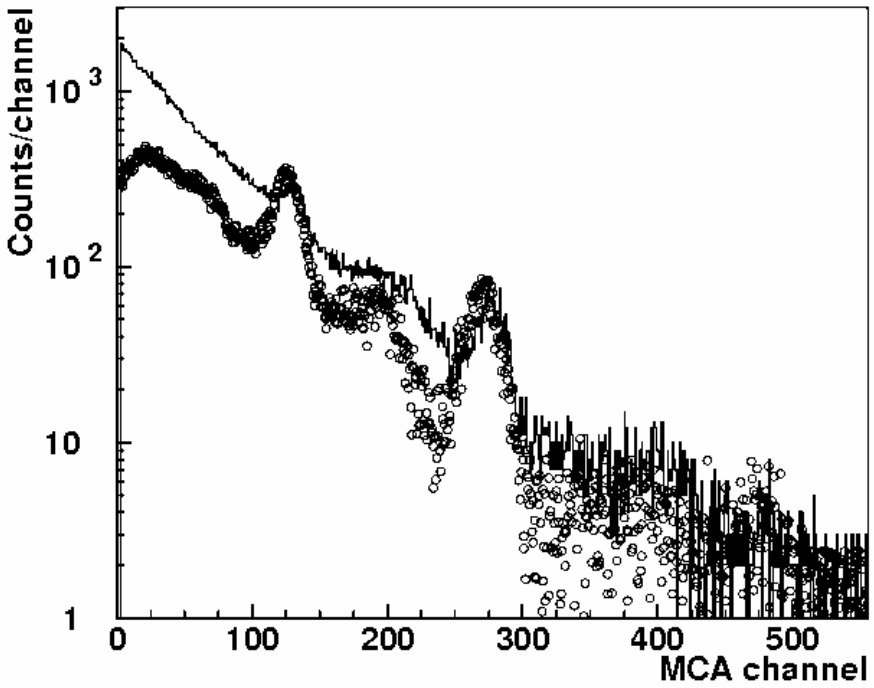

Fig. 3 Comparison of the energy spectrum. The circles correspond to the simulated and calculated total charge of liberated electron. The solid line corresponds to the results of experiment at the 3.5 kV/cm.

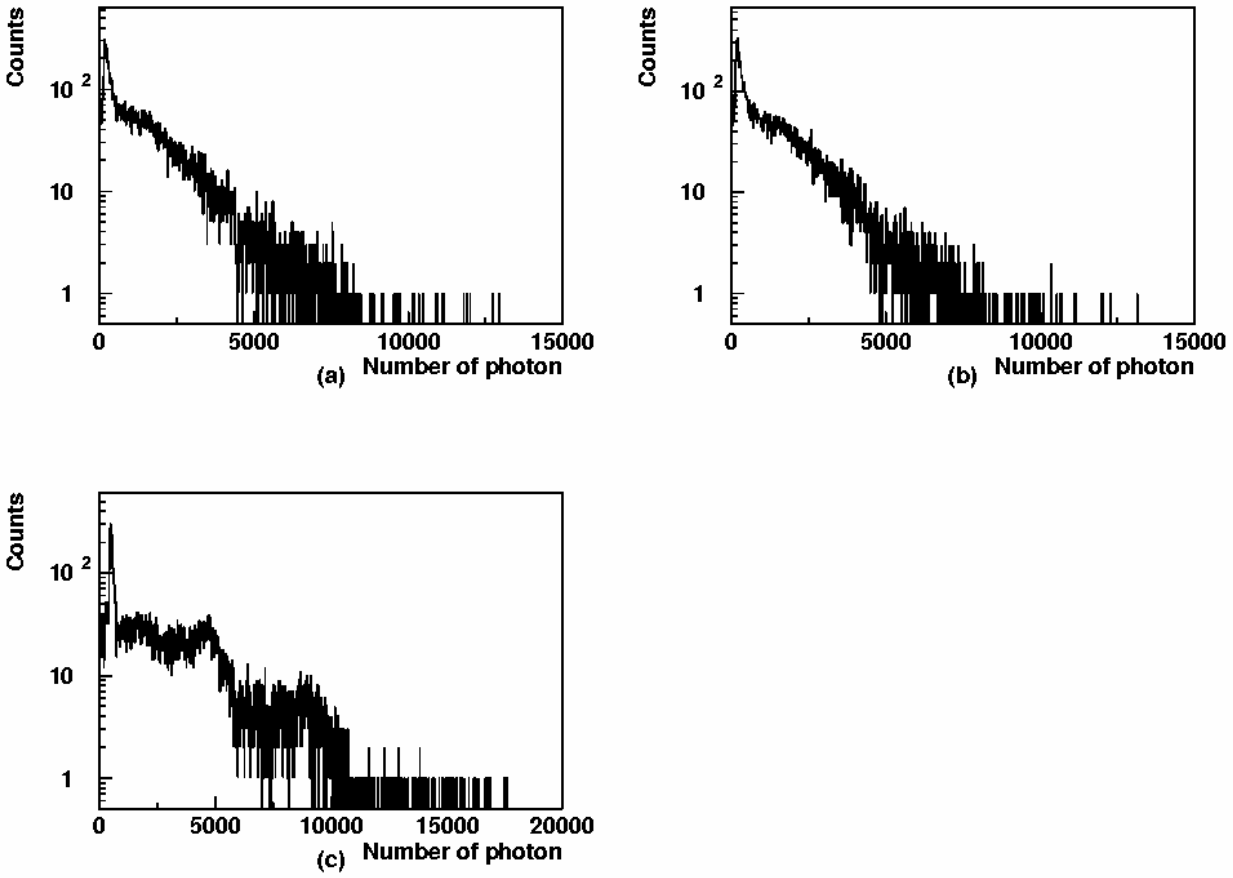

Fig. 4 Calculated results of observed the photon at each PMT. (a): one PMT observed photon. (b): the other PMT observed photon. (c): summed up observed at two PMT.